①

AD-A227 723

1990   Thesis/Dissertation

Properties of the Neutral Density in the Polar Lower
Thermosphere Determined By Incoherent Scatter Radar

Kenneth Winston Reese

AFIT Student at: University of Michigan

AFIT/CI/CIA - 90-086

AFIT/CI
Wright-Patterson AFB OH 45433

DTIC
ELECTE
OCT 24 1990
S E D

102

Abstract

The properties of the lower thermospheric neutral density are investigated using incoherent scatter radar technique. The data examined include 52 days of radar measurements from Chatanika, Alaska taken during the period 1976 - 1982, and one 6-day continuous period from Sondrestrom, Greenland taken during the Lower Thermospheric Coupling Study (LTCS-1) in September, 1987. The data are analyzed to determine average vertical profiles of the neutral density and to characterize the tidal oscillations of the neutral density in the lower thermosphere.

Techniques and software have been developed to process incoherent scatter radar data received on magnetic tapes in a standard output format. The ion-neutral collision frequency is the radar-derived parameter from which one can derive neutral density in the lower thermosphere. The complicated interaction of the radar with the plasma makes it possible for so many parameters of the plasma to be determined from the backscattered spectrum of radiation. In the E-region, the ion-neutral collision frequency is fit from the autocorrelation function (ACF) under the assumption that the ion and electron temperatures are equal. But in the polar lower thermosphere, there are processes that can cause thermal disequilibrium among the ions and electrons. These periods of E-region heating are removed from the data prior to further processing. The dominant interaction between ions and neutrals in the lower thermosphere is an induced dipole interaction. Total neutral number densities are derived from the ion-neutral collision frequencies using this theory. Then average vertical profiles of the neutral density are computed and the data are examined for the tidal oscillations present in the neutral density.

The data processing software developed in this study can efficiently process radar data from magnetic tape to plots of average neutral density profiles and tidal summaries in an almost-automated fashion. Only the identification of particle precipitation events and anomalous heating intervals require 'hands on' interface. Range smearing can introduce error into radar derived parameters, especially an exponentially changing parameter like the ion-neutral collision frequency. However, collision frequency profiles determined by different multipulse modes within 30 days of each other are virtually indistinguishable within the uncertainties of the measurements. The range smearing effect may be lessened in the E-region since the electron density is typically increasing with altitude (with proportional gain in signal strength) as the neutral density decreases.

Neutral scale heights fit to average ν_{in} profiles between 89-110 km at Chatanika show a very good correlation with the long term variation in F10.7 solar flux index, which indicates a strong dependence of lower thermospheric neutral scale height on solar cycle. Neutral scale

heights determined from the MSIS-86 model at 100 km showed virtually no variation with solar cycle, remaining nearly constant at a value near 6-km. The neutral scale height at Chatanika on the other hand varied on average between ~7-km in 1977 to more than 12-km in 1982.

Neutral scale heights fit to the average neutral density profiles from summer '80, autumn '80, winter '80-'81, and winter '81-'82 are 7.4 km, 9.5 km, 9.5 km, and 16.4 km respectively. The three profiles from 1980 and 1981 all displayed a roughly constant scale height with altitude. The winter '81-'82 profile deviates from a constant scale height profile at 90-km; if the 90-km average density is omitted from the fit, a neutral scale height of 9.1 km results. Using data from EISCAT, Kirkwood [1986] observed that vertical profiles from the entire year could be modelled by two cases: a case representing the summer and a case representing the rest of the year. Our results support this conclusion, although all our scale heights are higher than those of Kirkwood [1986], probably due to solar cycle effects as noted above.

The tidal analyses of the Chatanika and Sondrestrom neutral densities showed considerable complexity, however several observations can be made. The diurnal oscillations present in the neutral density were of the same order of magnitude as the semidiurnal components. This was somewhat unexpected because the semidiurnal tide is thought to be the dominant tidal oscillation at these altitudes.

The amplitudes of both the diurnal and semidiurnal oscillations were very large in the autumn. This was observed in both the autumn '80 case at Chatanika and the LTCS-1 (autumn '87) period at Sondrestrom. The phases observed during autumn at Sondrestrom and Chatanika were also similar. The phase of the diurnal oscillation at Chatanika stayed nearly constant with height up to 100 km, where it jumped by nearly 12 hours. This same feature was observed at Sondrestrom except the jump took place slightly lower, between 92-98 km. At Chatanika, the semidiurnal phase also remained constant up to 100 km, then decreased with altitude. The semidiurnal phase from LTCS-1 decreased with height indicative of an upwardly propagating wave with a vertical wavelength of approximately 15 km.

Accession For		
NTIS GRA&I	✗	
DTIC TAB	☐	
Unannounced	☐	
Justification		
By		
Distribution/		
Availability Codes		
Dist	Avail and/or Special	
A-1		

Abstract

The properties of the lower thermospheric neutral density are investigated using incoherent scatter radar technique. The data examined include 52 days of radar measurements from Chatanika, Alaska taken during the period 1976 - 1982, and one 6-day continuous period from Sondrestrom, Greenland taken during the Lower Thermospheric Coupling Study (LTCS-1) in September, 1987. The data are analyzed to determine average vertical profiles of the neutral density and to characterize the tidal oscillations of the neutral density in the lower thermosphere.

Techniques and software have been developed to process incoherent scatter radar data received on magnetic tapes in a standard output format. The ion-neutral collision frequency is the radar-derived parameter from which one can derive neutral density in the lower thermosphere. The complicated interaction of the radar with the plasma makes it possible for so many parameters of the plasma to be determined from the backscattered spectrum of radiation. In the E-region, the ion-neutral collision frequency is fit from the autocorrelation function (ACF) under the assumption that the ion and electron temperatures are equal. But in the polar lower thermosphere, there are processes that can cause thermal disequilibrium among the ions and electrons. These periods of E-region heating are removed from the data prior to further processing. The dominant interaction between ions and neutrals in the lower thermosphere is an induced dipole interaction. Total neutral number densities are derived from the ion-neutral collision frequencies using this theory. Then average vertical profiles of the neutral density are computed and the data are examined for the tidal oscillations present in the neutral density.

The data processing software developed in this study can efficiently process radar data from magnetic tape to plots of average neutral density profiles and tidal summaries in an almost-automated fashion. Only the identification of particle precipitation events and anomalous heating intervals require 'hands on' interface. Range smearing can introduce error into radar derived parameters, especially an exponentially changing parameter like the ion-neutral collision frequency. However, collision frequency profiles determined by different multipulse modes within 30 days of each other are virtually indistinguishable within the uncertainties of the measurements. The range smearing effect may be lessened in the E-region since the electron density is typically increasing with altitude (with proportional gain in signal strength) as the neutral density decreases.

Neutral scale heights fit to average v_{in} profiles between 89-110 km at Chatanika show a very good correlation with the long term variation in F10.7 solar flux index, which indicates a strong dependence of lower thermospheric neutral scale height on solar cycle. Neutral scale

heights determined from the MSIS-86 model at 100 km showed virtually no variation with solar cycle, remaining nearly constant at a value near 6-km. The neutral scale height at Chatanika on the other hand varied on average between ~7-km in 1977 to more than 12-km in 1982.

Neutral scale heights fit to the average neutral density profiles from summer '80, autumn '80, winter '80-'81, and winter '81-'82 are 7.4 km, 9.5 km, 9.5 km, and 16.4 km respectively. The three profiles from 1980 and 1981 all displayed a roughly constant scale height with altitude. The winter '81-'82 profile deviates from a constant scale height profile at 90-km; if the 90-km average density is omitted from the fit, a neutral scale height of 9.1 km results. Using data from EISCAT, Kirkwood [1986] observed that vertical profiles from the entire year could be modelled by two cases: a case representing the summer and a case representing the rest of the year. Our results support this conclusion, although all our scale heights are higher than those of Kirkwood [1986], probably due to solar cycle effects as noted above.

The tidal analyses of the Chatanika and Sondrestrom neutral densities showed considerable complexity, however several observations can be made. The diurnal oscillations present in the neutral density were of the same order of magnitude as the semidiurnal components. This was somewhat unexpected because the semidiurnal tide is thought to be the dominant tidal oscillation at these altitudes.

The amplitudes of both the diurnal and semidiurnal oscillations were very large in the autumn. This was observed in both the autumn '80 case at Chatanika and the LTCS-1 (autumn '87) period at Sondrestrom. The phases observed during autumn at Sondrestrom and Chatanika were also similar. The phase of the diurnal oscillation at Chatanika stayed nearly constant with height up to 100 km, where it jumped by nearly 12 hours. This same feature was observed at Sondrestrom except the jump took place slightly lower, between 92-98 km. At Chatanika, the semidiurnal phase also remained constant up to 100 km, then decreased with altitude. The semidiurnal phase from LTCS-1 decreased with height indicative of an upwardly propagating wave with a vertical wavelength of approximately 15 km.

PROPERTIES OF THE NEUTRAL DENSITY IN THE POLAR LOWER THERMOSPHERE DETERMINED BY INCOHERENT SCATTER RADAR

by

Kenneth Winston Reese

A thesis submitted in partial fulfillment
of the requirements for the degree of
Master of Science
(Atmospheric and Space Sciences)
in The University of Michigan
1990

Advisors:

Associate Professor, Timothy L. Killeen
Assistant Research Scientist, Roberta M. Johnson

Table of Contents

Chapter 1   Introduction

1.1 Statement of problem

The objective of this thesis is to investigate average vertical profiles of the neutral density and the dynamic behavior of the neutral density in the polar lower thermosphere using incoherent scatter radar technique.

To accomplish this objective, I have examined a large data base of radar measurements consisting of 52 days from Chatanika, Alaska and one 5-day continuous period from Sondrestrom, Greenland. The data has been analyzed to determine average vertical profiles of neutral density in the lower thermosphere and to characterize the tidal oscillations of the neutral density.

1.2 Thesis format

This thesis is organized around two papers (submitted for publication) which constitute Chapters 2 and 3. Chapter 2 presents an examination of lower thermospheric neutral densities at Sondrestrom during the Lower Thermospheric Coupling Study (LTCS-1). Chapter 3 is a study of the seasonal variations of lower thermospheric density at Chatanika. Because these papers have been written to stand alone as journal publications, there is necessarily a certain amount of repetition throughout the thesis. Chapter 4 contains a summary of the conclusions reached in both papers. I have also included an Appendix on the error analysis techniques used in these studies.

Chapter 1 is an expanded introduction in which I discuss background information pertaining to this effort in detail. This introduction is organized in a fashion which parallels the steps with which the radar data has been processed. First of all, the theory of incoherent scatter and the manner in which the radar beam interacts with the plasma environment is discussed. Locations and operating procedures of the incoherent scatter radar facilities are described, along with a description of the method by which ionospheric parameters are determined from the scattered signal.

1

The data analyzed in this study were acquired in the form of processed data on magnetic tape. The radar-derived parameter of interest in calculating neutral densities is the ion-neutral collision frequency (v_{in}). Certain assumptions are made to derive the collision frequencies, and during periods of E-region heating these assumptions can be violated. In the following section, heating processes in the lower thermosphere are described, as well as the techniques I have used for removing these periods from the data. I then discuss the theory relating the collision frequency to the neutral density.

The final stage in the analysis presented here is to examine the neutral densities to determine average vertical profiles and temporal variations, particularly at tidal frequencies. In the final section of the introduction, I describe the expected vertical profile of neutral density in the lower thermosphere. Finally, the mechanism by which tidal oscillations of the neutral density are produced, as well as the tidal modes which should be prevalent in the lower thermosphere are discussed.

1.3 Incoherent scatter radar theory

The theory of incoherent scatter is a complicated subject and requires a thorough knowledge of plasma physics. The theory has been presented by Dougherty and Farley [1963] and Hagfors and Brockelman [1971]. The subject has also been reviewed by Evans [1969, 1974] and been described in a more intuitive sense by Walker [1978] and Vickrey [1980]. In this thesis I shall describe the theory of incoherent scatter at this more intuitive level, with limited reference to plasma theory. Specifically, I will make it clear how so many physical parameters of the plasma and neutral gas can be determined from the scatter spectra.

1.3.1 Incoherent scatter

Incoherent scatter, also called Thomson scatter, is the scattering of electromagnetic waves by random fluctuations in the density of free electrons in the ionosphere. The scattering is extremely weak, thus very powerful radars must be employed to observe this phenomenon. The fluctuations in the electron density correspond to random thermal motion of the electrons as well as plasma waves of various types, including ion-acoustic waves, Langmuir waves, and cyclotron

2

waves. One can think of these fluctuations in the electron gas as a superposition of a whole spectrum of density waves of different wavelengths with randomly oriented wave vectors. Through an application of Bragg's law, we know that constructive interference with the radar wave only occurs for density waves propagating forward or backward along the direction of the radar beam, with a wavelength equal to half the wavelength of the incident radiation [Walker, 1978]. But of course, these constructively interfering waves in the electron gas propagate with a whole spectrum of different phase velocities, and thus the backscattered radiation consists of the original radar frequency Doppler shifted by an amount given by the distribution of wave velocities.

1.3.2 Debye length and the radar wavelength

The character of the plasma fluctuations detected by the radar is a function of the radar wavelength. To understand this, some discussion must be made of the concept of the Debye length. The Debye length can be thought of as a shielding distance in a plasma. Since the electrons and ions are free to move about, any individual charged particle is surrounded by a cloud of oppositely charged particles, thus limiting the distance over which the charge of any individual particle can be felt. For a wave propagating in a plasma, the Debye length also gives an indication of the relative magnitudes of the pressure and electrical forces on the electrons and ions in the wave. It can be shown that the Debye length is given by

$$\lambda_D^2 = \frac{\varepsilon_0 k_B T_e}{e^2 n_e}$$

where T_e is the electron temperature, n_e is the electron density, ε_0 is the permittivity of free space, k_B is Boltzmann's constant, and e the electron charge.

If the radar wavelength is much less than the Debye length, it will be scattered by fluctuations in the electron density at wavelengths half that of the probing radar. But the plasma can not sustain oscillations at these wavelengths because of the dominance of the pressure force relative to electrical force. In this case, that of "classical" Thomson scatter [Gordon, 1958], the scattered spectrum is Gaussian with a width characteristic of the electron thermal speed.

In actuality, most incoherent scatter radars have a wavelength much greater than the Debye length. In this limit, electrostatic forces on the electrons are much greater than the pressure forces, and due to their low inertia, the electrons will tend to move right along with any oscillations in the ions. Although the scattering is by the electrons, because the electrons move with the ion oscillations, the radar detection of these waves provides information on the distributions of both the ions and electrons. This gives rise to the portion of the incoherent spectra called the ion line, first identified by Bowles [1958, 1961].

In addition to the oscillations that contribute to the ion line, waves exist in the electron gas alone, with frequencies too high for the massive ions to respond to. These waves, called electron plasma waves, oscillate with a frequency proportional to the square root of the electron density. They give rise to a portion of the incoherent scatter spectrum called the plasma line. Traditionally, most information about the plasma is determined by fitting the ion line portion of the spectra. However, recent work has involved simultaneous fits of the ion and plasma lines to improve the number of parameters able to be independently fit from the spectra [Bjorna and Kirkwood, 1988; Bjorna, submitted for publication].

1.3.3 Determining the properties of the plasma

The physical properties of the plasma are determined by examination of the backscattered signal in either the frequency or time domains. The spread in backscattered power over a range of frequencies is caused by the Doppler shifting of the radar wave as it is scattered by waves in the plasma. This return is called a power spectral density function or power spectrum.

Alternatively, the scattered signal can be sampled as a function of time rather than frequency, and the average correlation as a function of time lag can be computed. This is called an autocorrelation function (ACF). These two approaches actually contain equivalent information since they form a Fourier transform pair. Most incoherent scatter radar facilities form and analyze the ACF, however the power spectrum is easier to understand with respect to the physical processes which give rise to its shape. I will therefore describe the affects of changes in plasma properties on the power spectra. Vickrey [1980] provides a useful summary relating power

spectrum and ACF shapes. The physical constants of the plasma which can be determined from the power spectra or ACF are the electron density, ion and electron temperature, line-of-sight ion drift velocity, ion composition and ion-neutral collision frequency. Below I briefly describe how changes in these parameters lead to changes in the scattered spectra, thus allowing us to determine them by fitting the spectra.

Electron density. Since it is the electrons which are doing the scattering, the total scattered power is proportional to the electron density. Integrating the power spectra over all frequency provides an estimate of the electron density. Alternatively, one can determine the electron density using the zeroth lag of the ACF.

Ion and electron temperature. Most incoherent scatter spectra in the literature are double-humped. This distinctive shape comes from the ion acoustic waves which are detected by the radar. As described above, for wave lengths much greater than the Debye length, oscillations in the ion density will impose themselves on the electrons. These oscillations are joint longitudinal oscillations resembling sound waves in the neutral gas [Walker, 1981]. The velocity of the ion acoustic waves is approximately

$$V = \left[\frac{k_B(T_e + T_i)}{m_i}\right]^{1/2}$$

where k_B is Boltzmann's constant, T_i and T_e are the ion and electron temperature, and m_i is the ion mass. If there were no damping processes occurring in the plasma, the scattered signal would consist of two lines Doppler shifted an amount corresponding to plus or minus the ion acoustic velocity [Vickrey, 1980].

These waves, however, are damped by a process called Landau damping. The easiest way to understand this process is by considering the interaction of the electric field of the wave with the individual charged particles [Walker, 1978]. Ions moving slightly faster than the wave will feed energy into it, while ions moving slightly slower than the wave will be accelerated by it, thus extracting energy from the wave. Because of the shape of the ion velocity distribution function, there will be more ions moving slightly slower than the wave than slightly faster. The amount of

5

Landau damping is proportional to the slope of the ion velocity distribution at the ion acoustic velocity. The net effect is to decrease the phase speed of the wave, thus smearing the spectrum of Doppler shifted radiation toward the transmitted frequency. This gives rise to the characteristic double humped shape of the spectra. The electrons also damp the wave, but at the ion acoustic velocity, the electron velocity distribution function is almost flat owing to the greater characteristic width of the electron velocity distribution (because $m_i/m_e >> 1$). As a result, the electrons contribute little to the damping of the wave.

Figure 1.1 shows the effect that changing T_e/T_i has on the scattered spectra. Increasing T_e without increasing T_i results in a faster ion acoustic wave with no corresponding changes in the ion velocity distribution. This moves the wave into a region less strongly damped by the ions, and the spectrum becomes more distinctly double humped at the Doppler shift corresponding to the ion acoustic velocity. Conversely, decreasing T_e results in greater and greater Landau damping, with the limit approaching a Gaussian-shaped scattered spectra corresponding to the ion thermal distribution.

Ion drift velocity. The ion drift velocity results in the entire spectrum being Doppler shifted a small amount. From the offset, the line of sight ion drift can be determined. This is shown in Figure 1.2. The Doppler shift resulting from these drifts is very small compared to the overall width of the spectra. By pointing the radar in three different directions in succession, a vector ion drift can be estimated above the radar.

Ion-neutral collision frequency. The effect of collisions on the scattered spectra is similar to the effect of increased Landau damping; the width of the spectrum is reduced and the double humps are smoothed out. Collisions begin to have an effect on the scattered spectra when the mean free path between collisions is comparable to the radar wavelength, or similarly when the time between collisions approaches the period of the ion acoustic wave [Walker, 1978; Vickrey, 1980]. In the limit of very high collision frequencies, waves cannot propagate at all and the scattered spectra approaches a narrow line at the frequency of the radar. This distinguishes the collisional process from Landau damping since intense damping leads to a Gaussian spectrum

while a large collision frequency leads to a Lorentzian profile. Figure 1.3 shows a power spectra for various values of the normalized collision frequency,

$$\psi = \left(\frac{v_{in}}{k}\right)\left[\frac{m}{2k_B T}\right]^{1/2}$$

where k is the radar wave number. For $\psi=0$, the spectrum shows the double humped shape, and for $\psi=10$, the spectrum tends toward a Lorentzian shape.

In conclusion, by fitting the shape of the scattered power spectra or autocorrelation function, many physical constants of the plasma can be determined. Table 1.1 is a summary of parameters directly fit from the spectra (described above), and some of the many other geophysical parameters of interest that can be derived from these. Of course, the most important parameter in this study is the ion-neutral collision frequency, however in the course of this study, I have also examined E-region electron densities, ion and electron temperatures, and electric field magnitudes. This ability to learn so much about the plasma is what makes incoherent scatter radar such a powerful tool for studying the thermosphere and ionosphere. In the next section, I describe the location and operating procedures of the radar facilities used in this study.

1.4 Description of incoherent scatter radar facilities

1.4.1 Locations

There are incoherent scatter radar facilities currently in operation at Sondrestrom, Greenland; Millstone Hill, Massachusetts; Arecibo, Puerto Rico; Jicamarca, Peru; and the European incoherent scatter radar (EISCAT) located in northern Scandinavia. The Sondrestrom radar was previously located at Chatanika, Alaska. Figure 1.4 displays the location of these radars; note the longitudinal chain of radars bracketed by Sondrestrom and Jicamarca. Table 1.2 contains some of the operating characteristics of the radars that are currently in operation.

In this thesis, I have analyzed measurements obtained by the Sondrestrom/Chatanika radar. The Chatanika radar operated from 1971 until 1982. The Chatanika location allowed the complex auroral region to be examined. During a typical daily cycle, the radar was located within the auroral oval for several hours hear dawn and dusk, moving to subauroral latitudes near midday and

7

within the polar cap near midnight. When the radar was moved to Sondrestrom, Greenland in 1983, it moved considerably closer to the north magnetic pole. It can now probe the region below the magnetospheric cusp near noon, the polar cap on the nightside, and the northward portion of the auroral oval in between [Wickwar et al., 1984]. At both locations, the radar could sample a variety of high latitude regions and the physical processes important there; the Sondrestrom location is more suited to polar cap observations.

1.4.2 Operating modes

The Chatanika/Sondrestrom radar antenna is fully steerable, and thus a variety of antenna operating modes are possible. Some of these are displayed in Figure 1.5 and include fixed position, multiposition, and continuous scan. All the data examined in this study was collected in a 3-position mode usually at a fixed elevation angle, but sometimes with varying elevation angles. This 3-position mode allows the determination of vector ion drifts from which neutral winds and electric fields can be derived.

The Chatanika/Sondrestrom radar also has a number of different pulse schemes. These include a short pulse (generally 60 μs), a long pulse (usually 320 μs), and two multipulse modes. The short pulse is used for power measurements only (from which n_e is determined), while the long- and multipulse modes are used for both power and spectrum measurements. The long pulse yields an effective range resolution (discussed below) of approximately 50 km, thus is best suited for F-region measurements. The multipulse yields much better range resolution and is best suited for measurements in the E-region. Since ion-neutral collision frequency can only be determined in the E-region, almost all parameters used in this study have been derived from multipulse measurements.

There are two standard multipulse operating modes used at Sondrestrom and Chatanika. The first consisted of two 160-μs pulses separated by about 7-ms. The resultant correlation function has 16 lags of 10-μs duration and a range resolution of approximately 24 km. Because of its larger range resolution, this multipulse mode provides a better signal to noise ratio (SNR) than the true multipulse.

The second multipulse mode, known as the "true multipulse" consists of a single 60-µs pulse followed 7-ms later by a burst of three 60-µs pulses. The correlation function formed has 32 lags at 10-µs intervals and a range resolution of 9 km. This mode is best for characterizing vertical profiles in the E-region as long as there is sufficient ionization (and resultant SNR).

In Chapter 3, I compare v_{in} profiles determined using both these multipulse modes to see if the multipulse mode affects the profiles through range smearing or other processes. Please continue to Chapter 3 for a more detailed discussion of range smearing effects, including other relevant studies which have been conducted by other investigators on this subject.

1.4.3 Radar fundamentals

In this section I illustrate how the radar makes a measurement and forms the ACF using a simple range-time diagram (Figure 1.6). In this diagram, altitude is plotted versus time showing the propagation of a radar pulse up through the atmosphere. Backscattered radiation is shown returning to the ground where it is sampled by the radar as a function of time. In this example, the radar is pointing straight up, the pulse duration, τ, is 160-µs followed by a long (7-ms) listening period. The listening period is long enough that by the time the next pulse is transmitted, the previous pulse is well outside the thermosphere, and no backscattered radiation returns from it. In this way, there is no ambiguity in determining from which pulse the scattered signal has returned.

The pulse length is $\tau \cdot c \approx 48$ km in the vertical, but this is not the altitude resolution. At any instant in time, the backscattered radiation sampled at the ground is from a volume of length $(\tau \cdot c)/2$. This then is the effective height resolution for each 10-µs sample shown in Figure 1.6. Now, how is the autocorrelation function formed? Once the radar has received all 16 of the 10-µs samples shown, it calculates the mean product of pairs among the 16 samples for 0 to 15 lags. The zeroth lag is the product of each 10-µs sample with itself; the first lag is the product of each sample with its neighbor, and so on. Each higher lag is computed using one less pair until the 15th lag has only one pair containing the first and last 10-µs sample within the 160-µs interval. The mean correlation as a function of lag is what comprises an autocorrelation function.

9

The above example is meant to be illustrative only. In reality, a more complicated lag sampling pattern and weighting scheme is used to form the ACFs used in most incoherent scatter measurements, especially in the case of a multipulse signal. Also, the alert reader may have realized that there are contributions to the ACF from a range interval given by $\tau \cdot c$. But the weighting factors that enter into the measurements lead to an effective range resolution on the order of half that, or $\sim \frac{\tau c}{2}$ [de la Beaujardiere, 1984].

Once the radar has received the backscattered radiation and formed the ACFs, the information enters the signal processing system of the radar. Here I will only highlight several aspects of the signal processing; an interested reader may refer to de la Beaujardiere et al. [1984] for additional information.

There are two main stages of signal processing, the first stage, processing and integration; and the second stage, derivation of ionospheric parameters. In the first stage, the ACFs are averaged over a set integration time. This stage also corrects the ACFs for instrumental effects. A first guess is made at the electron density, and the line-of-sight ion velocities are computed. The corrected ACFs and other information are then passed on to the second stage of processing.

Second stage processing consists of a whole family of different programs for deriving ionospheric parameters from the data. The second stage program which is of interest to me is the autocorrelation fitting program or ACFIT. The input to ACFIT is the ACFs from stage one. ACFIT performs an iterative nonlinear least squares fit of observed ACFs to calculated theoretical ACFs. The theoretical ACFs are generated from the theory of Dougherty and Farley [1963] which is briefly described above. By fitting the observed ACF to these theoretical ACFs, one or more sets of parameters can be determined from each observed ACF. Uncertainties are also computed for each of the physical parameters returned from each fit.

Table 1.3 shows the parameters which can theoretically be determined from the observed ACF. I have discussed how most of these influence the scattered spectrum in the sections above. In practice, only a limited number of parameters can be fit from a single ACF. Fortunately, not all the parameters listed affect the spectrum at all different altitudes. For instance, in the F-region, v_{in}

will have no effect on the scattered spectra. In the E-region, ion composition will have little effect on the spectrum since the primary ions, NO^+ and O_2^+ have nearly identical masses. Thus one may limit the number of parameters for which the spectrum must be fit in different altitude zones. Table 1.4 shows the four different zones which are considered in the ACFIT routine. In this study, zone 1 is the altitude range of primary interest.

Even within each zone, it still may not be possible to simultaneously fit for all the parameters listed in Table 1.3. For instance, T_e/T_i and v_{in} have very similar effects on the scattered spectra which cannot be separated in practice. The approach used in the ACFIT routine is to make several different fits to the data within each zone and to use geophysical arguments to decide which is most valid.

Table 1.5 shows the three different fits which are performed within the E-region. In Fit 2, v_{in} is taken from a model and T_i and T_e are fit separately. The ion-neutral collision frequency is obtained from Fit 3. The key assumption made in this fit is that $T_i=T_e$. If there are heating processes which cause $T_i \neq T_e$, then the v_{in} derived under these circumstances can be in error and should not be used. In the low- and mid-latitude regions, the ion and electron (and neutral) temperatures are rarely disturbed from thermal equilibrium in the E-region ($T_i=T_e=T_n$). But in the high latitude regions which were/are probed by the Chatanika and Sondrestrom radars, there are heating processes which may disturb the thermal equilibrium of the E-region. In the next section, these processes are described.

1.5 Data discrimination technique

1.5.1 Discussion of E-region heating mechanisms

Since the E-region above Chatanika and Sondrestrom is subject to heating processes which can violate the assumptions used to derive the ion-neutral collision frequency, periods when these heating processes are important must be removed from the data prior to analysis of v_{in}. Here I first describe the processes which can disturb the thermal equilibrium of the E-region at high latitude. Then I describe the technique I have used to identify and remove heating intervals.

The collision frequency in the E-region is sufficiently high that the temperatures of the electron, ion, and neutral species are usually equal. In the low and mid-latitudes, this is almost always true. During the daytime, the electron temperature in the F-region is elevated above the ion and neutral temperature by photoelectrons. But in the lowest part of the thermosphere, the high collision rate rapidly spreads that energy to the neutrals causing their temperatures to be approximately equal. Other mechanisms which can heat the lower thermosphere, such as dissipation of gravity waves or tides, heat the neutrals and charged particles at the same rate, and do not disturb the thermal equilibrium.

In the polar region, however, there are energy inputs which preferentially heat the electrons or ions. When these energy inputs turn off, collisions rapidly equilibrate the temperatures. But during these periods of heating, the ion and electron temperatures can be significantly elevated above the neutrals, and significantly different from each other. Three processes have been identified which can preferentially heat E-region electrons or ions. These are particle heating, Joule heating, and anomalous wave heating [Lathuillere, 1983].

Particle heating occurs when there is an injection of high energy magnetospheric particles down magnetic field lines into the polar thermosphere. Schlegel et al. [1980] has observed electron temperatures at 110 km elevated several hundreds of degrees above the ion temperatures during a precipitation event observed at Chatanika on May 15, 1977. These precipitation events are characterized by peaks in the electron density which are significantly higher than normal photoionization values.

Joule heating is the heating that results from dissipation of electric currents in the atmosphere. The dissipation is the result of collisions between the ions and neutrals, and electrons and neutrals. The neutral gas is heated by two processes: it is heated directly through collisions with the ions. This frictional heating is proportional to the square of the flow velocity difference between the ions and neutrals. The neutrals are also heated by thermal exchange with the ions. Due to their small heat capacity (as a result of their low density), the ions are quickly heated to a temperature much greater than that of the neutrals. Most of this heat is then returned to the neutrals

12

through heat exchange processes which are proportional to the temperature difference. But while the Joule heating is taking place, the E-region ion temperature can be elevated significantly above the neutral temperature. The electron gas is also heated by Joule heating, but the process serves to enhance most preferentially the ion temperature [Lathuillere et al., 1983].

Wickwar et al. [1981] and Schlegel and St. Maurice [1981] have both observed anomalously high electron temperatures in the E-region at Chatanika which can not be explained by particle precipitation or Joule heating. These periods were correlated with elevated electric fields, and St. Maurice et al. [1981] has suggested that the elevated temperatures may result from heating by plasma waves produced through a modified two stream instability. This heating process is the only known mechanism which is thought to be able to significantly disturb thermal equilibrium below 110 km [Lathuillere et al., 1983].

Figure 1.7 shows heating rates in the lower thermosphere from Chatanika determined during a period with a very high electric field. Note that Joule heating peaks at around 120 km while heating by particle precipitation and unstable waves peaks lower, around 100-105 km. This indicates that during periods with elevated electric fields, the electrons may be preferentially heated through unstable wave processes at lower altitudes than the ions, which are preferentially heated by Joule heating. I examined this by computing the correlation coefficient between T_i and electric field magnitude (|E|), and between T_e and |E| as a function of altitude using data from the LTCS-1 period at Sondrestrom. The results are summarized in Table 1.6. Clearly the electron temperature is best correlated with |E| at 115 km, while T_i is best correlated with |E| at the highest altitude available from the Zone 1 fit, 126 km. This is apparently in agreement with the observations of St. Maurice et al [1981], however the altitudes observed here are somewhat higher.

1.5.2 Technique for filtering out periods of heating

This previous section provides an interesting aside to the focus of this effort because it is not my purpose to study E-region heating mechanisms; indeed my intent is to eliminate episodes of heating from my data prior to analyzing the collision frequencies. For this purpose, it is essential to have an understanding of the nature and relative importance of the processes that are being

discriminated against. The process I have used to identify periods of E-region heating involves close examination of measurable quantities derived from the radar which cause or respond to the heating. These quantities are the electric field magnitude, the E-region electron densities, and the E-region ion and electron temperatures.

The electric field above the radar is determined by measuring the ion drift velocities in the F-region where collision frequencies are small and the ion equation of motion becomes $V = -ExB/B^2$, allowing the electric field to be estimated [Wickwar et al., 1981]. The electric field measured by the radar is the electric field perpendicular to the magnetic field ($E_\perp$, high electron mobility along B causes $E_{||} \approx 0$). I showed above how the E-region ion and electron temperatures are correlated to the magnitude of the electric field. This can further be seen in Figure 2.1, which is a scatter plot of T_i at 126 km vs IEI from LTCS-1. It is apparent that the measured electric field magnitude is an excellent tracer of periods of E-region heating. When the electric field is elevated, the ion and electron temperatures in the E-region also increase (albeit at different altitudes).

Therefore, I have used the magnitude of the electric field to identify periods of heating. Anytime IEI exceeds a certain threshold, the data from that period has not been used The value of this threshold is somewhat arbitrary. Flå et al. [1985] calculated that for $E_\perp < 20$ mV/m, the difference between T_i and T_n cannot exceed 4.3°K below 110 km. Similarly, Lathuillere et al. [1983] calculate that for $E_\perp \approx 40$ mV/m, the ion temperature will increase approximately 20°K at 110 km. The E-region electron temperature will be elevated by unstable wave heating in the presence of elevated electric fields; Wickwar et al. [1981] has observed clear cases of elevated electron temperatures for electric fields of 25-40 mV/m.

I initially used a threshold of 30 mV/m when analyzing the LTCS-1 data, but later modified the threshold to 25 mV/m when analyzing the Chatanika data. The reasons for selecting these thresholds were both the literature described above and analysis of the data. Figure 1.8 shows a histogram which shows the distribution of the number of occurrences of the electric field magnitude falling within the indicated ranges. Also indicated is the threshold of 30 mV/m which I

used. The thresholds of 25 and 30 mV/m were selected as a compromise between eliminating all possible heating periods and keeping as much data as possible.

Eliminating periods of elevated electric field magnitude should take care of almost all significant E-region heating events, but it does not indicate the presence of particle precipitation events which can preferentially elevate the electron temperature. At altitudes of 116 km and higher, the electron temperature can be increased due to loss of energy from auroral primary and secondary electrons [Wickwar et al., 1981]. Particle precipitation events are characterized by sharply elevated electron densities above their normal photoionization values. When no particle precipitation is present, the electron density has a diurnal variation proportional to the solar ionizing flux. Figure 1.9 shows electron density as a function of time at 126 km from the LTCS-1 period. The shaded regions indicate local nighttime. Clearly evident is the diurnal rise and fall of electron density corresponding to ionization by solar radiation. But within the night, there are electron density peaks indicated by the arrows which are not associated with the diurnal variation in electron density. This is especially true on the night of the 25th when the nighttime electron densities exceed the daytime amounts. These peaks are particle precipitation events, and these intervals have been removed from the data.

Usually after removing periods of elevated electric fields and anomalously high electron density, all periods of E-region heating have been removed. However, I have also examined the ion and electron temperatures from the upper E-region to make sure that no additional heating intervals have been missed.

In my data analysis software, periods of elevated electric fields are removed automatically. Periods of elevated electron density and other heating are removed using time delineations determined by hand after examining the N_e and T_i/T_e plots. The result of this semi-laborious process is a set of ion-neutral collision frequencies which have been fit from ACFs taken during periods consistent with the assumption that $T_i = T_e$. From this point, further analysis of the ion-neutral collision frequency can commence.

1.6 Theory relating the ion-neutral collision frequency to neutral density

15

The next step in my analysis scheme is to convert the ion-neutral collision frequencies into neutral number density. The ν_{in}s can be examined in their own right, but the neutral density is a more basic and physical quantity of the atmosphere for investigation. Several applications for neutral densities are conceivable, including comparison with satellite and rocket measurements, or with the predictions of atmospheric models. In the section to follow, I first discuss the types of interactions possible between the ions and neutrals. I then derive the expression relating ν_{in} to the neutral density.

1.6.1 Ion-neutral interactions

Converting ν_{in} to neutral density requires a knowledge of the types of interactions between the ions and the neutrals. At the temperatures found in the undisturbed E-region, the most important non-resonant ion-neutral interaction comes from the induced dipole attraction which has a potential distribution given by, $\varphi=-\alpha e^2/2r^4$, where α is the neutral atom polarizability, r is the radial separation, and e is the electric charge [Banks, 1966]. As the ion approaches the neutral atom or molecule, the electron cloud of the neutral shifts inducing an electric dipole within the particle and thus attracting the ion through electrostatic forces. It is found that the collisional cross section is proportional to $T^{-1/2}$ and the collision frequency is independent of temperature.

When the temperature exceeds 300°K, the induced dipole attraction is countered by a short range quantum mechanical repulsive force [Banks, 1966]. At very high temperatures, the contribution from polarization becomes small and the collision cross section becomes nearly constant yielding a collision frequency which varies as $T^{1/2}$. Since there have been very few measurements of high temperature collision cross sections or collision frequencies, the induced dipole interaction must be assumed to be correct when studying ion-neutral interactions. However, in the E-region, temperatures are usually low enough that the assumption of an induced dipole interaction is a good one. Also, since periods of heating are eliminated from our data, so too are periods when the induced dipole assumption could potentially be a bad one.

There is also the possibility for resonant interaction between the ions and neutrals. A resonant interaction occurs when an ion and its parent neutral exchange an electron and, in effect,

16

exchange places. The cross section of this type of process is often very large. However, the only resonant interaction of any potential importance in the E-region is between O_2 and O_2^+ since of the other primary neutral constituents, N_2 and O, neither O^+ or N_2^+ is present in the E-region in any significant concentration. Figure 1.10 shows the momentum transfer cross section for O_2^+-O_2. It can be seen that resonant charge exchange interaction only becomes important at very high temperatures compared with the polarization interaction. Thus for the same arguments as above, polarization should be the dominant ion-neutral interaction in the E-region for this data set.

1.6.2 Formula relating v_{in} to neutral density

With the ion-neutral interaction assumed to be of the induced dipole type, one can derive an expression relating the collision frequency to the neutral density. The following derivation follows that of Banks and Kockarts [1973]. We consider a gas consisting of two components, an ion species (i) and a neutral species (n) in thermal and dynamic equilibrium. As such, both particles are characterized by Maxwellian velocity distributions with the same bulk velocity and thermal speed. The velocity dependent momentum transfer collision frequency can be defined as

$$v_{in} = n_n g \sigma_D(g) \tag{1.1}$$

where the relative speed, $g=|v_i-v_n|$, and $\sigma_D(g)$ is the momentum transfer cross section. The average momentum transfer collision frequency (indicated by an overbar) is obtained by averaging over all relative speeds.

$$\overline{v}_{in} = \frac{4}{3} n_n \overline{v}_{in} \overline{Q}_D \tag{1.2}$$

where the average relative velocity is

$$\overline{v}_{in} = \left(\frac{8k}{\pi}\right)^{1/2} \left(\frac{T_i}{m_i} + \frac{T_n}{m_n}\right)^{1/2} \tag{1.3}$$

and the average momentum transfer cross section is given by

$$\overline{Q}_D = \left(1/c^6\right) \int_0^\infty g^5 \sigma_D(g) \exp\left[-g^2/c^2\right] dg \tag{1.4}$$

where the constant c

$$c^2 = \left(\frac{2kT_i}{m_i} + \frac{2kT_n}{m_n} \right)$$

For the induced dipole interaction between an ion and neutral particle, the ion-neutral velocity dependent momentum transfer cross section for singly charged ions is

$$\sigma_D = 2.21\pi \left(\alpha e^2 / \mu g^2 \right)^{1/2} \tag{1.5}$$

where α is the neutral gas atomic polarizability, μ is the ion-neutral reduced mass, and g is the ion-neutral relative velocity. Plugging into equation 1.4 above gives

$$\overline{Q}_D = 2.21\pi \left(\frac{\alpha e^2}{\mu} \right)^{1/2} \frac{1}{c^6} \int_0^\infty g^4 \exp\left(-g^2 / c^2\right) dg \tag{1.6}$$

and integrating gives

$$\overline{Q}_D = \frac{3\sqrt{2}}{16} \pi^{3/2} \left(\frac{2.21^2 \alpha e^2}{\mu} \right)^{1/2} \left(\frac{kT_i}{m_i} + \frac{kT_n}{m_n} \right)^{-1/2} \tag{1.7}$$

Now plugging this expression into equation 1 2 and also substituting in equation 1.3 gives

$$\overline{\nu}_{in} = \pi \left(\frac{2.21^2 \alpha e^2}{\mu} \right)^{1/2} n_n \tag{1.8}$$

If we let $\alpha = \alpha_o \times 10^{-24}$ [cm^3] and $\mu = \mu_A / N_A$ [g] (where μ_A is the reduced mass in atomic mass units and N_A is Avogadro's number); and knowing $e = 4.80 \times 10^{-10}$ [esu], then

$$\overline{\nu}_{in} = \left(\pi \cdot 2.21 \cdot e \cdot 10^{-12} \sqrt{N_A} \right) \left(\frac{\alpha_o}{\mu_A} \right)^{1/2} n_n$$

or,

$$\overline{\nu}_{in} = 2.59 \times 10^{-9} \left(\frac{\alpha_o}{\mu_A} \right)^{1/2} n_n \tag{1.9}$$

This result relates the average momentum transfer collision frequency of one ion/neutral species pair to the number density [cm^{-3}] of that neutral species. This equation is in the center of mass reference frame, but the incoherent scatter radar actually measures the collision frequency in the laboratory reference frame [Lathuillere et al., 1983]. These two collision frequencies are related by

18

$$V_{in} = \frac{m_n}{m_i + m_n} \overline{V}_{in}$$

(1.10)

where the lack of an overbar now indicates the laboratory reference frame. Equation 1.9 can now be expressed in the laboratory reference frame as

$$V_{in} = \frac{2.59 \times 10^{-9}}{m_i} \sqrt{\alpha_o \mu_{in}} \cdot n_n$$

(1.11)

This equation can then be summed over the three principle neutral species of the E-region, N_2, O_2, and O, to get an expression for the collision frequency between the total neutral density (N) and each ion species (i) [Lathuillere et al., 1983].

$$V_{iN} = \frac{2.59 \times 10^{-9}}{m_i} \left(n_{N_2} \alpha_{N_2}^{1/2} \mu_{iN_2}^{1/2} + n_{O_2} \alpha_{O_2}^{1/2} \mu_{iO_2}^{1/2} + n_O \alpha_O^{1/2} \mu_{iO}^{1/2} \right)$$

(1.12)

But $\alpha_O=0.79$, $\alpha_{O2}=1.59$, and $\alpha_{N2}=1.76$. I'll let $n_n=\%(n)N \cdot 0.01$, where $\%(n)=100 \cdot n_n/N$. Then equation 1.12 becomes

$$V_{iN} = \frac{2.59 \times 10^{-11}}{m_i} \left(\%(N_2)1.76^{1/2}\mu_{iN_2}^{1/2} + \%(O_2)1.59^{1/2}\mu_{iO_2}^{1/2} + \%(O)0.79^{1/2}\mu_{iO}^{1/2} \right) \cdot N$$

(1.13)

This expression still depends upon the ion species. However in the E-region, the two principle ions are NO^+ and O_2^+. They are so close in atomic mass (30 and 32) that minimal error will be introduced by assuming a single ion (I) of intermediate mass [Lathuillere et al., 1983]. If the intermediate mass is taken as 30.5 (corresponding to 75% NO^+, 25% O_2^+), then the final expression relating the total E-region ion-neutral collision frequency with the total neutral number density is

$$V_{IN} = K \cdot N$$

(1.14)

where $\quad K = \dfrac{2.59 \times 10^{-11}}{30.5} \left(\%(N_2) \cdot 5.07 + \%(O_2) \cdot 4.98 + \%(O) \cdot 2.88 \right)$

1.6.3 Determination of K

All that remains is to determine K by estimating the relative abundances of the three major E-region species. A reasonable first order approximation of K can be made by taking the ground percentages of N_2, O_2, and O. However, at these altitudes, the relative percentages of the three

19

components are changing with altitude according to their different scale heights. Our approach in determining K is to use the MSIS-86 model [Hedin, 1986] to estimate the relative percentages of the three constituents. This is certainly better than assuming that K is constant with altitude. However, it does not take into effect possible short scale fluctuations in the relative composition. Offerman et al. [1981] made several rocket shots into the lower thermosphere which indicated that in the E-region, the density of N_2 and O_2 may vary up to about 5%, while atomic oxygen may have varied by factors of 4 to 5. But O is still a minor constituent in the E-region (ranging on average from ~0.5% at 90 km to ~15 % at 125 km), and its weighting factor in K is smaller than that of N_2 and O_2 - both serving to lesson the sensitivity of K to large fluctuations in atomic oxygen density. In chapter 2, our average values of K are compared with other values cited previously in the literature. On the whole, the agreement is good.

1.7 Lower thermospheric neutral density

Up to this point, I've shown how the neutral density can be derived from incoherent scatter radar measurements in the lower thermosphere. The objective of this thesis is to determine the average vertical structure and the temporal behavior of the neutral density in the lower thermosphere using incoherent scatter radar. In this next section, I first discuss the average vertical profile expected in the lower thermosphere as well as the important dynamic influences which cause temporal variations in the neutral density.

1.7.1 Average vertical structure

The average neutral number density falls of exponentially with height in the lower thermosphere. For an isothermal atmosphere, the change in density with height is given by the expression

$$n(z) = n(z_o)\exp\left\{\frac{-(z - z_o)}{H}\right\}$$

where z_o is a reference altitude and H is the scale height given by

$$H = \frac{k_B T}{mg}$$

where k_B is Boltzmann's constant, T is the neutral temperature, m is the mean molecular weight, and g is the acceleration of gravity. For our purposes, we can assume g to be constant with height over the altitude range of interest. In this case

$$g_o = g_{sfc}\left(\frac{R_e}{R_e + 90}\right)^2 = 9.5 \text{ msec}^{-2}$$

This is a good approximation to the average vertical structure of the neutral density in the lower thermosphere, but there are two complications that need to be considered. The first concerns the mean composition, m, and the second concerns the assumption of an isothermal atmosphere. Each of these considerations are discussed below.

The lower thermosphere sits astride the region of the atmosphere where eddy processes give way to diffusion. This boundary is called the homopause and is located around 100 km. Below the homopause, mixing keeps the relative amounts of the major atmospheric constituents at approximately their surface values. But above the homopause, the relative amounts of the major constituents begin to change with height as each constituent falls off with a scale height given by its individual molecular weight. As a result, the mean molecular weight, m, decreases with altitude. Based on average percentage compositions from MSIS-86 for the LTCS-1 period, m changes from ~28.8 amu at 90 km to ~26.9 amu at 120 km, a change of ~7%. With all else held constant, this change serves to increase the neutral scale height with altitude.

The second complication is the fact that the atmosphere is not isothermal throughout the lower thermosphere. In fact, the mesopause is the coldest place in the atmosphere, and the temperature rises rapidly throughout the lower thermosphere. The simplest way to treat this is by assuming a constant scale height gradient with height. Banks and Kockarts [1973] show that

$$\frac{\rho g}{\rho_o g_o} = \left(\frac{H}{H_o}\right)^{-\frac{(1+\beta)}{\beta}}$$

where $\beta = \dfrac{\partial H}{\partial z}$ = constant. Expanding this in a series and keeping only the first term, one can show that

21

$$n \approx n_o \exp\left\{\frac{(1+\beta)(z-z_o)}{H_o + 0.5\beta(z-z_o)}\right\}$$

where n_o and H_o are the neutral number density and scale height at the reference altitude z_o. Kirkwood [1986] has used this formula to model neutral density profiles derived from incoherent scatter radar measurements. H_o and β are determined from the radar temperature data. The profiles obtained from Kirkwood's model are compared with the LTCS-1 neutral density profile in chapter 2.

1.7.2 Dynamic influences in the lower thermosphere

Two processes which can cause temporal variations in the neutral density are gravity waves and tides. I am specifically interested in characterizing the tidal variations in the neutral density. Below I present a brief discussion of gravity waves followed by a discussion of tidal theory. I show why we expect to see tidal variations in the neutral density. Finally, I discuss the tidal modes which should be important in the polar thermosphere.

Gravity waves result from the displacement of an air parcel in a stratified atmosphere where gravity provides the restoring force. Tides are low frequency gravity waves influenced by the rotation of the earth. Gravity waves have a maximum frequency given by the the Brunt-Vaisala frequency. Upwardly propagating tides and gravity waves increase in amplitude with increasing height to conserve energy density in an exponentially decreasing density field. They amplify until the waves become unstable and break into turbulence, or until viscosity and ion drag become important factors in damping the wave [Killeen, 1990]. This damping becomes important at thermospheric altitudes. In the thermosphere, gravity waves are excited by episodic heating events. They therefore tend to be rather sporadic and constitute some of the "noise" superimposed on the tidal oscillations observed in the neutral density.

Tides are global scale oscillations which are the response of the atmosphere to periodic forcing. Tides are characterized by frequencies which are integral multiples of the forcing. This forcing can be the gravitational attraction of the sun and moon, or the daily heating of the atmosphere by absorbed solar radiation. In the atmosphere, the tides excited by solar heating are

the most important. In the following section, I will outline the theory which explains the production of tidal oscillations in the neutral density. This classical development follows that of Lindzen and Chapman [1969].

1.7.3 Classical tidal theory

In order to obtain a set of equations which can be solved by classical methods for atmospheric tides, some assumptions must be made. The atmosphere is assumed to be comprised of a perfect gas, in local thermodynamic and hydrostatic equilibrium, and the atmosphere is regarded as a thin layer on a spherical earth. In addition, dissipative processes such as viscosity, ion drag and radiative transfer are ignored, and the tidal fields are considered as linearizable perturbations about some basic state. Given these assumptions (and neglecting the tidal potential due to gravitational attraction by the sun and the moon), linearized versions of the governing equations can be written as:

$$\frac{\partial u}{\partial t} - 2\omega v \cos\theta = -\frac{1}{a}\frac{\partial}{\partial \theta}\left(\frac{\delta p}{\rho_o}\right)$$
(1.15)

$$\frac{\partial v}{\partial t} + 2\omega u \cos\theta = -\frac{1}{a\sin\theta}\frac{\partial}{\partial \varphi}\left(\frac{\delta p}{\rho_o}\right)$$
(1.16)

$$\frac{\partial \delta p}{\partial z} = -g\delta\rho$$
(1.17)

$$\frac{D\rho}{Dt} \equiv \frac{\partial \delta\rho}{\partial t} + w\frac{d\rho_o}{dz} = -\rho_o\chi$$
(1.18)

where

$$\chi \equiv \nabla\cdot\vec{V} = \frac{1}{a\sin\theta}\frac{\partial}{\partial \theta}(u\sin\theta) + \frac{1}{a\sin\theta}\frac{\partial v}{\partial \varphi} + \frac{\partial w}{\partial z}$$

$$\frac{R}{\gamma-1}\frac{DT}{Dt} \equiv \frac{R}{\gamma-1}\left(\frac{\partial \delta T}{\partial t} + w\frac{dT_o}{dz}\right) = \frac{gH}{\rho_o}\frac{D\rho}{Dt} + J$$
(1.20)

and

$$\frac{\delta p}{p_o} = \frac{\delta T}{T_o} + \frac{\delta\rho}{\rho_o}$$
(1.21)

Here θ = colatitude; ϕ = east longitude; t = time; u = northerly velocity; v = westerly velocity; w = upward velocity; δp = pressure perturbation; $\delta\rho$ = density perturbation; δT = temperature perturbation; J = thermal tidal heating per unit mass per unit time; ω = earth's rotation rate; a = the radius of the earth; $\gamma = \dfrac{C_p}{C_v} = 1.4$; and $\kappa = \dfrac{(\gamma-1)}{\gamma} = \dfrac{2}{7}$.

Equations 1.15 and 1.16 are the linearized momentum equations, equation 1.17 is the hydrostatic pressure relation, (1.18) is the continuity equation, (1.19) is the thermodynamic energy equation, and (1.20) is the linearized perfect gas law.

Now defining the dependent variable G,

$$G = -\frac{1}{\gamma p_o}\frac{Dp}{Dt}$$

and assuming fields periodic in time and longitude of the form

$$f = f^{\sigma,s}(\theta,z)\exp\{i(\sigma t + s\phi)\}$$

our five equations can be reduced to a single equation for G alone:

$$H\frac{\partial^2 G^{\sigma,s}}{\partial z^2} + \left(\frac{dH}{dz} - 1\right)\frac{\partial G^{\sigma,s}}{\partial z} = \frac{g}{4a^2\omega^2}F\left(\left(\frac{dH}{dz} + \kappa\right)G^{\sigma,s} - \frac{\kappa J^{\sigma,s}}{\gamma gH}\right)$$ (1.22)

where F is an operator defined by

$$F \equiv \frac{1}{\sin\theta}\frac{\partial}{\partial\theta}\left(\frac{\sin\theta}{f^2 - \cos^2\theta}\frac{\partial}{\partial\theta}\right) - \frac{1}{f^2 - \cos^2\theta}\left(\frac{s}{f}\frac{f^2 + \cos^2\theta}{f^2 - \cos^2\theta} + \frac{s^2}{\sin^2\theta}\right)$$

This may be solved by the method of separation of variables. Assuming that $G^{\sigma,s}$ may be written

$$G^{\sigma,s} = \sum_n L_n^{\sigma,s}(z)\Theta_n^{\sigma,s}(\theta)$$ (1.23)

and also that the set $\{\Theta_n^{\sigma,s}(\theta)\}_{\text{all } n}$ is complete for $0\leq\theta\leq\pi$, then J may also be expanded as

$$J^{\sigma,s} = \sum_n J_n^{\sigma,s}(z)\Theta_n^{\sigma,s}(\theta)$$ (1.24)

Substitution of (1.23) and (1.24) into equation 1.22 gives the following equations for $\Theta_n^{\sigma,s}$ and $L_n^{\sigma,s}$

$$F\left(\Theta_n^{\sigma,s}\right) = -\frac{4a^2\omega^2}{gh_n^{\sigma,s}}\Theta_n^{\sigma,s}$$

$$(1.25)$$

and

$$H\frac{d^2L_n^{\sigma,s}}{dz^2} + \left(\frac{dH}{dz} - 1\right)\frac{dL_n^{\sigma,s}}{dz} + \frac{1}{h_n^{\sigma,s}}\left(\frac{dH}{dz} + \kappa\right)L_n^{\sigma,s} = -\frac{\kappa}{\gamma gHh_n^{\sigma,s}}J_n^{\sigma,s}$$

$$(1.26)$$

where $h_n^{\sigma,s}$ is the constant of separation. Equation 1.25 is called LaPlace's Tidal Equation for the free surface oscillations of a spherical ocean envelope. With the boundary conditions on $\{\Theta_n\}$ that they be bounded at the poles, equation 1.25 defines an eigenfunction-eigenvalue problem where the eigenvalues $\{h_n\}$ are referred to as the set of equivalent depths, and the eigenfunctions $\{\Theta_n\}$ are known as the Hough functions. The Hough functions describe the latitudinal variation of the tidal solutions in the classical approximation. Equation 1.26 is called the Vertical Structure Equation and, given two boundary conditions, has a unique solution for the vertical structure of a given Hough mode.

It can be further shown that

$$\delta\rho = \sum_n \delta\rho_n(\chi)\Theta_n$$

$$(1.27)$$

where

$$\chi = -\log\left(\frac{P_o}{P_o(0)}\right)$$

and

$$\delta\rho_n = \frac{P_o(0)}{(gH)^2}\left\{\frac{\gamma gh_n}{i\sigma}\exp\left(-\frac{\chi}{2}\right)\left[\left(1 + \frac{1}{H}\frac{dH}{d\chi}\right)\left(\frac{dy_n}{d\chi} - \frac{1}{2}\right) + \frac{H}{h_n}\left(\kappa + \frac{1}{H}\frac{dH}{d\chi}\right)y_n\right] - \frac{\kappa J_n}{i\sigma}\right\}$$

Equation 1.27 describes the response of the density to the tidal input. Similar expressions can be derived for the tidal response of δp, δT, and w in terms of the Hough functions, and for u and v in terms of related expansion functions derived from the Hough functions.

From this classical tidal derivation, one can see that tidal variations should be present in the neutral density. Some pretty severe assumptions were necessary to render the equations solvable by nonnumerical means. But even when dissipative processes, mean zonal winds, or temperature

25

gradients are allowed, the solutions can still be interpreted in terms of Hough modes, with the indirect forcing of tidal modes considered as a form of "mode coupling" [Johnson, 1987] A comprehensive numerical model of tidal oscillations in the earth's atmosphere has been developed by Forbes [1982a, 1982b, 1982c]. Unfortunately, this model currently only calculates the response of winds and temperature output fields, not the response of the neutral density.

The tidal response of the atmosphere is strongly a function of altitude and latitude. The latitudinal structure of the tidal modes is described by the Hough functions. A Hough mode is identified by two indices (m,n) where m represents the zonal wavenumber, and n is related to the number of nodal crossings of the Hough function with latitude. As mentioned above, the atmospheric response to solar heating is much greater than the response to the gravitational attraction of the sun or moon. Thus the primary period of forcing is 24 hours, and tidal modes with m=1 are referred to as diurnal, m=2 as semidiurnal, and so on.

Figure 1-11 shows the first five Hough functions for the diurnal (t1-12a) and semidiurnal (1-12b) tidal modes. Hough functions with n=odd number are antisymmetric with respect to the equator while n=even are symmetric. Modes with n<0 are referred to as evanescent modes, which means the tide does not propagate from its altitude of excitation. As consequence, evanescent tidal modes have a constant phase with height. Modes with n>0, on the other hand, propagate vertically from their altitude of excitation. All semidiurnal tides can propagate vertically at all latitudes; propagating diurnal tides are largest equatorward of ±30° latitude [Johnson, 1987].

1.7.4 Important thermospheric tidal modes

With this theory and terminology now in hand, let us finally describe the important tides in the thermosphere. The solar tides are primarily excited by absorption of solar UV radiation by ozone in the middle atmosphere (stratosphere and mesosphere), absorption of IR radiation by water vapor in the lower atmosphere, and by absorption of UV and EUV radiation by all gases in the thermosphere [Fesen et al., 1986]. Thus in the lower thermosphere, one can expect to find tides excited in situ, the evanescent tides, which are confined to the altitude of their excitation. In addition, one may expect to find tides propagating upward into the thermosphere from below.

These tides will be predominantly semidiurnal in nature, especially in the polar regions because the propagating diurnal modes are essentially confined to low latitudes (see Figure 1.11). In addition, most vertically propagating diurnal modes have short vertical wavelengths which lead to effective damping of these modes in the lower thermosphere. An exception is the (1,1) diurnal mode, which is quite large in the lower thermosphere, but is essentially dissipated below about 105 km [Fesen et al, 1986].

Semidiurnal tides have longer vertical wavelength and are quite important in the lower thermosphere. As the semidiurnal tides propagate upwards, their amplitude increases to conserve energy density. This amplification continues into the lower thermosphere where at some altitude, viscosity, thermal conduction, and ion drag (which become increasingly important with increasing altitude) serve to prevent further amplification with height.

Sharp et al. [1978] examined data from the AE-E satellite to determine the nature of tidal variations in the equatorial thermospheric neutral density. Figure 1.12 shows the amplitudes of the diurnal and semidiurnal components as a function of altitude. Above ~180 km, the diurnal tide is dominant, while below 180 km the amplitude of the semidiurnal tide exceeds that of the diurnal tide. Thus in the equatorial lower thermosphere, the semidiurnal tide is the most important tidal oscillation in the neutral density.

In the polar lower thermosphere, no equivalent tidal analysis of neutral density has been performed. However from the above discussion, we do expect to see tides in the neutral density. And in summary, the diurnal tide should be mainly nonpropagating, however there may be contribution from a propagating diurnal mode in the lowest part of the thermosphere. The semidiurnal tide will have contributions both excited in situ, and propagating upwards form the middle atmosphere.

1.8 Review of literature

Before my two papers are presented in the next two chapters, it is useful to briefly review the literature pertaining to this subject. Incoherent scatter radar facilities have been used very productively during the past two decades or so, and the literature is full of works on many varied

27

subjects. But here I specifically summarize the work which has been done on determining lower thermospheric ion-neutral collision frequencies or neutral densities from incoherent scatter radar. Works having to do with other pertinent subjects will be (or have been) summarized where appropriate throughout the paper. This review is essentially chronological.

Wand and Perkin [1968] showed ion temperature and v_{in} profiles between 97-120 km from Arecibo. Their v_{in} values were fit from the autocorrelation function assuming the ion and electron temperatures were equal ($T_i=T_e$). The theory of Dougherty and Farley [1963] was used to determine v_{in} from the radar measurements (as it has been in most papers described below). Salah [1974] determined thermospheric temperature, density, and winds for several days at Millstone Hill. The temperature oscillations were fit for a semidiurnal tide, however although a time history of v_{in} was displayed indicating considerable variability, no tidal analysis was made of the v_{in} oscillations. Good agreement was found between the average v_{in} profiles obtained and the Jacchia model [1971]. Wand [1976] primarily examined the semidiurnal tide in the lower thermospheric temperatures at Arecibo. Ion-neutral collision frequency profiles were presented from five separate days which showed considerable variability but overall reasonable agreement with the Jacchia model and a model based on hydrostatic equilibrium. Tepley and Mathews [1978] continued to examine temperatures and v_{in} profiles at Arecibo in the 80-100 km range. They observed profiles both warmer and denser (by almost $\frac{1}{2}$ scale height) than the CIRA (1972) model atmosphere.

At mid- and low- latitudes, the assumption that $T_i=T_e$ is almost always true in the E-region, and can generally be made without further consideration when determining ion-neutral collision frequencies. But in the polar regions, this assumption is not always true. Schlegel et al. [1980] were able to fit for v_{in}, T_i, and T_e during particle precipitation events at Chatanika. Their collision frequency profiles showed good agreement with the CIRA (1972) model. Tepley et al. [1981] examined v_{in} at Arecibo in the 70-100 km range. They also found very good agreement with CIRA (1972) down to approximately 70 km, with the deviation below this altitude attributed to the presence of negative ions. Lathuillere et al. [1983] continued the examination of the polar thermosphere at Chatanika using the first "large" set of data (over 30 hours). Neutral temperatures

28

and densities were determined with periods of E-region heating excluded from the data. Much of my work in this thesis parallels and extends this earlier work.

Flå et al. [1985] examined E-region collision frequencies from EISCAT with a range resolution of approximately 3 km. Despite different geophysical conditions, they observed little change in the v_{in} profile over a 2-week period. However they attribute an event which increased v_{in} by 1.5-2 times in $1\frac{1}{2}$ hours as the passage of a large amplitude gravity wave. Kofman and Lathuillere [1985] reviewed the EISCAT capabilities for measuring E- and F-region parameters, especially the multipulse technique for probing the E-region with high range resolution. Neutral density profiles were determined for two days in December 1983 and March 1984 with heating periods removed. They found scale heights of 6.5 km and 5.7 km respectively and attributed the difference to higher particle energy deposition on the day in December. Kirkwood [1986] examined seasonal and tidal variations of neutral temperatures and densities in a large data set between December 1984 to November 1985. Collision frequency profiles are presented by season and modeled with a density profile given a constant scale height gradient. Amplitudes and phases of the semidiurnal tide in the neutral density were presented for four separate periods. This study is the only other tidal study with which my results are comparable. Huuskonen et al. [1986] presented high resolution (1.2 km) observations of v_{in} from EISCAT, as did Kofman et al. [1986] also at EISCAT. Kofman et al. observed neutral scale heights at 100 km between 5-7 km for 7 days in 1983-1985. Nygrén et al. [1987] tested a new method of measuring the ion-neutral collision frequency at EISCAT. Instead of using the scattered spectrum shape, they combined the vertical ion velocity and electric field measurements through the ion momentum equation to deduce v_{in} between 95-130 km. Bjorna [in press] also tried something novel at EISCAT. The temperature/collision frequency ambiguity in the ion line autocorrelation function is resolved by including the plasma line in their fit. This new method resulted in v_{in} profiles which compared better with the MSIS-86 model than those derived from the ion line alone. Finally, Huuskonen [1989] presented continued high resolution observations of collision frequencies and temperatures at EISCAT based on 80 hours of data.
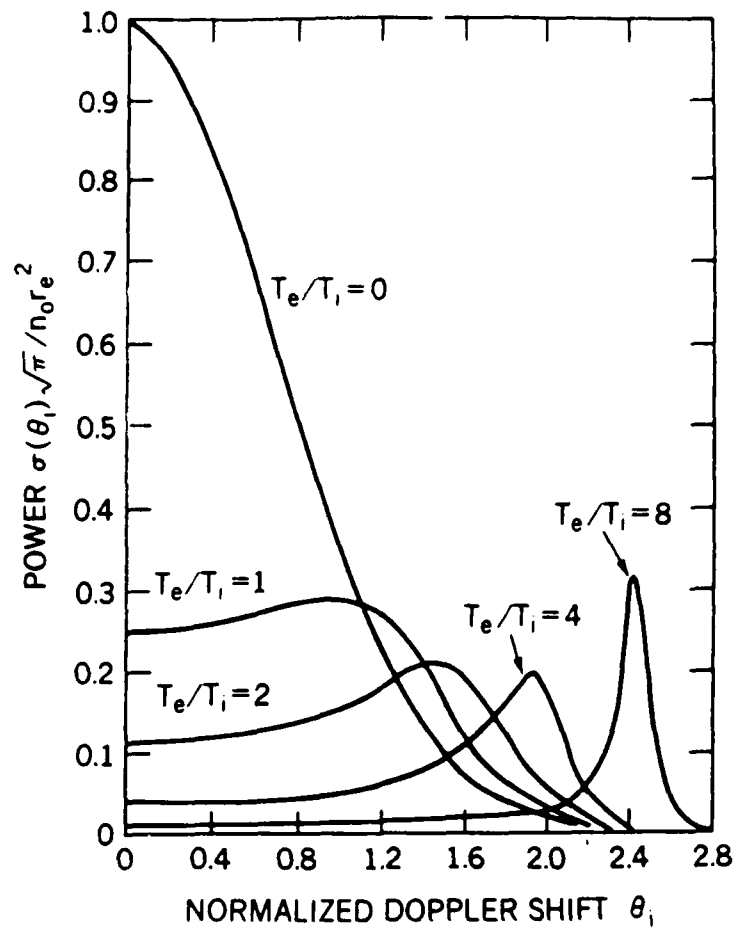
29

Figure 1.1 Normalized half spectra of the ionic component (radar $\lambda \gg \lambda_D$) for different values of T_e/T_i. Note the progression from a Gaussian shape ($T_e/T_i = 0$) to a narrow hump near the ion-acoustic frequency. [after Fejer, 1961]
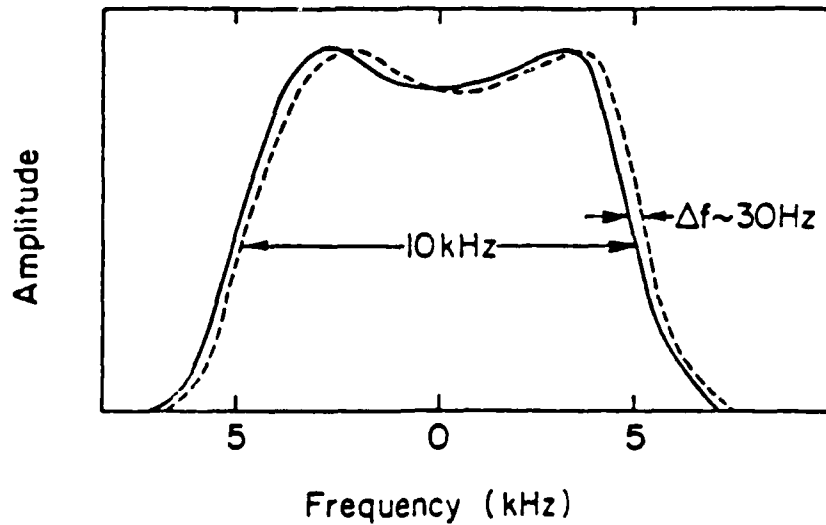

Figure 1.2 The spectral effect of a uniform ion drift velocity [after Vickrey, 1980]
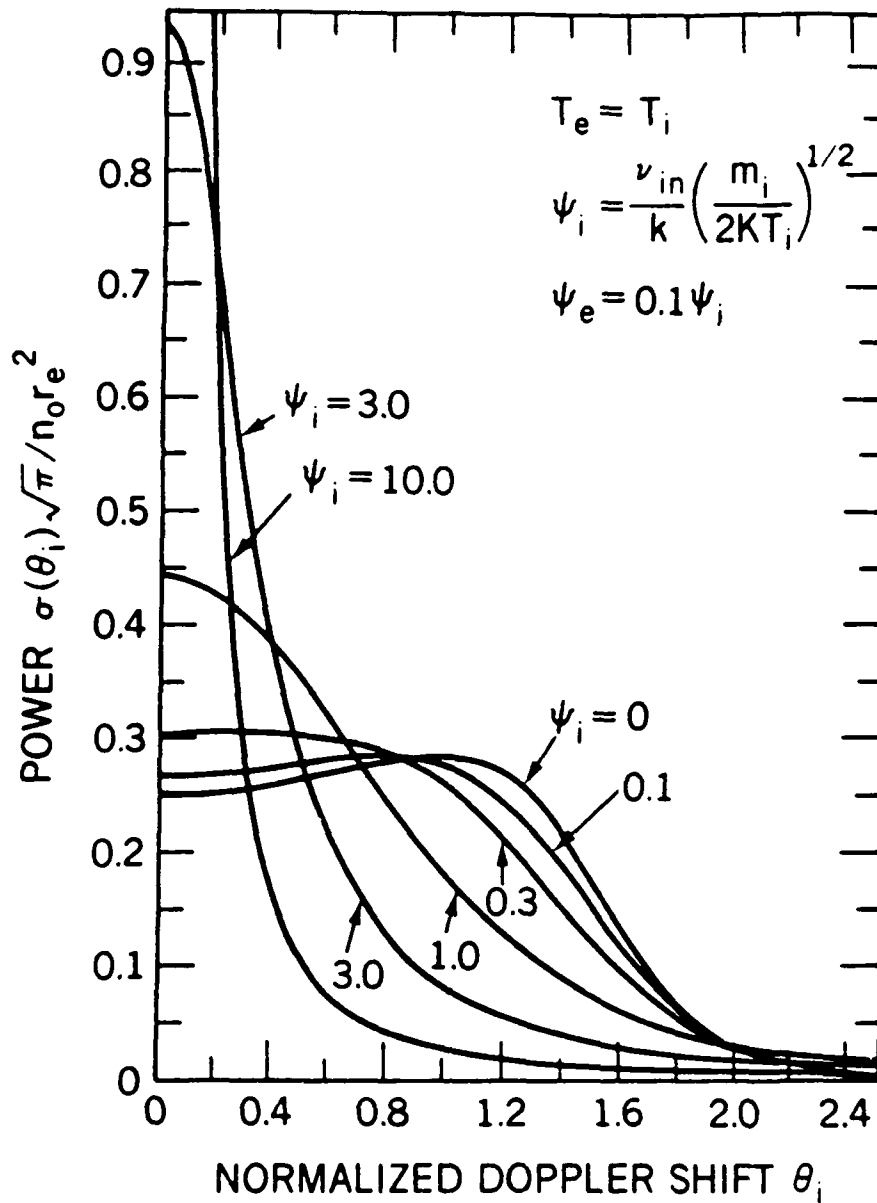
30

Figure 1.3 Normalized half spectra of the ionic component for $T_e = T_i$ and for different normalized ion-neutral collision frequencies. Notice the difference between the high collision frequency case (approaching Lorentzian) and the $T_i \gg T_e$ case (Gaussian) [after Dougherty and Farley, 1963]

```
┌─────────────────────────────────────┐
│           Basic Parameters            │
└─────────────────────────────────────┘
┌───────────────────────────────────────────────────────┐
│   Electron density            Electron temperature      │
│                                                         │
│   Line-of-sight ion velocity      Ion temperature       │
│                                                         │
│   Ion-neutral collision frequency      Ion composition  │
└───────────────────────────────────────────────────────┘


┌─────────────────────────────────────┐
│          Derived Parameters           │
└─────────────────────────────────────┘
┌───────────────────────────────────────────────────────┐
│   Vector ion velocity             Electric field        │
│                                                         │
│   Meridional neutral wind         Vector neutral wind    │
│                                                         │
│   Exospheric temperature          Neutral temperature    │
│                                                         │
│   Atomic oxygen density           Heat flux at high altitude │
│                                                         │
│   Energy loss from electrons to ions and neutrals    Energy input from thermal conduction │
│                                                         │
│   Hall conductivity               Pedersen conductivity  │
│                                                         │
│   Currents perpendicular to B     Birkeland current      │
│                                                         │
│   Joule heating                   Ion-electron production rate │
│                                                         │
│   Energy deposition by auroral electrons   Energy spectrum of auroral electrons │
│                                                         │
│   Several optical emissions       Total neutral density  │
└───────────────────────────────────────────────────────┘
```

Table 1.1   Geophysical parameters available from incoherent scatter radars

32

NAME	LOCATION			Frequency (MHz)	Power (MW)	ANTENNA TYPE
Sondrestrom	Sondrestrom, Greenland	67°N	51°W	1290	5	Monostatic, steerable
Chatanika	Chatanika, Alaska	65°N	148°W	"	"	"
EISCAT	Northern Scandinavia	69°N	19°E	933.5	2	Tristatic
Millstone Hill	Westford, Massachusetts	43°N	72°W	I. 440	3	Vertical
				II. 1295	4	Monostatic, steerable
Arecibo	Arecibo, Puerto Rico	18°N	67°W	I. 40	2.5	Vertical
				II. 430	2	"
Jicamarca	near Lima, Peru	12°S	77°W	50	4	Vertical

Table 1.2   Summary of incoherent scatter radar facility locations and operating characteristics.

33

1. Electron density [cm^{-3}]	N_e
2. Electron-ion temperature ratio	T_e/T_i
3. Electron temperature [°K]	T_e
4. Ion temperature [°K]	T_i
5. Ion velocity [m/s]	V_i
6. Ion composition	q
7. Electron-ion velocity difference [m/s]	V_e-V_i
8. Ion-neutral collision frequency [s^{-1}]	ν_{in}
9. Ion-temperature ratio	T_{i2}/T_i
10. Ion velocity difference [m/s]	$V_{i2}-V_i$
11. Ratio of reduced ion-neutral collision frequencies	ψ_i/ψ_{i2}

Table 1.3 Basic ionospheric parameters theoretically determinable from incoherent scatter radar. $q = [O^+]/N_e$, $\psi_i = \nu_{in}/[k(m_i/2k_BT_i)^{1/2}]$, $k = 4\pi/\lambda_{radar}$), V_{i2} = ion velocity of second ion species, and T_{i2} = ion temperature of second ion species. [after de la Beaujardiere, 1984]

Zone 1	E-region (85 to 120 km)
	N_e, T_i, T_e, V_i, ν_{in}
Zone 2	E- to F-region (115 to 250 km)
	N_e, T_i, T_e, V_i, ion composition (O^+, NO^+, O_2^+)
Zone 3	F-region (200 to 700 km)
	N_e, T_i, T_e, V_i
Zone 4	Upper F-region (500 to 1200 km)
	N_e, T_i, T_e, V_i, ion composition (O^+, He^+, H^+)

Table 1.4   Four different thermospheric zones considered in the ACFIT routine and the parameters that are determined. In this study, only Zone 1 is used. [after de la Beaujardiere, 1984]

FIT	ASSUMPTIONS	Variables Determined From Fit
1	$T_i = T_e$ ν_{in} = model	N_e, T_i, V_i
2	ν_{in} = model V_i = value from fit 1	N_e, T_i, T_e
3	$T_i = T_e$ V_i = value from fit 1	N_e, T_i, ν_{in}

Table 1.5   Three different fits performed within the E-region (Zone 1). The ion-neutral collision frequency is derived in Fit 3. [after de la Beaujardiere, 1984]
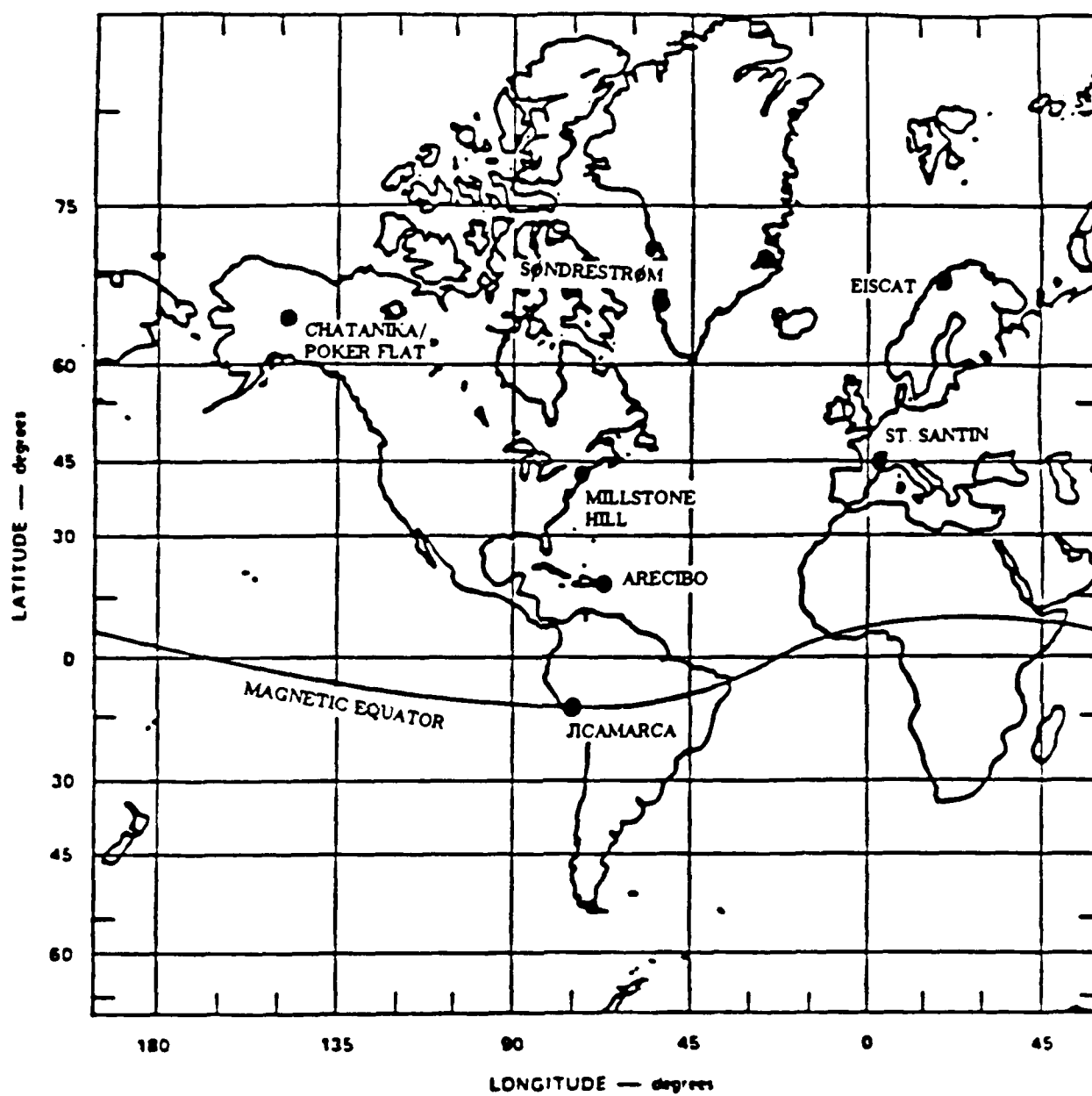
Figure 1.4   Map showing the location of incoherent scatter radar installations, past and present. Note the longitudinal chain of radars anchored by Sondrestrom in the north and Jicamarca in the south.
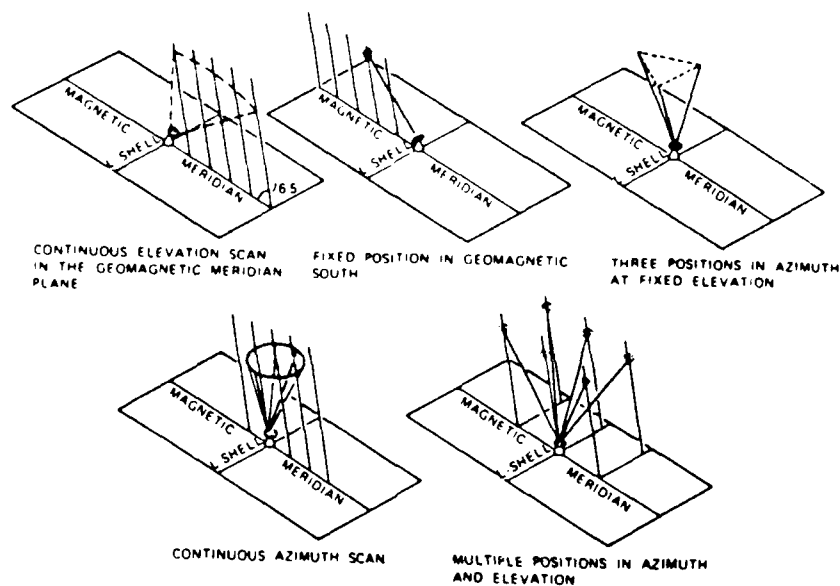
36

CONTINUOUS ELEVATION SCAN
IN THE GEOMAGNETIC MERIDIAN
PLANE

FIXED POSITION IN GEOMAGNETIC
SOUTH

THREE POSITIONS IN AZIMUTH
AT FIXED ELEVATION

CONTINUOUS AZIMUTH SCAN

MULTIPLE POSITIONS IN AZIMUTH
AND ELEVATION

Figure 1.5 Typical antenna modes at Chatanika and Sondrestrom.
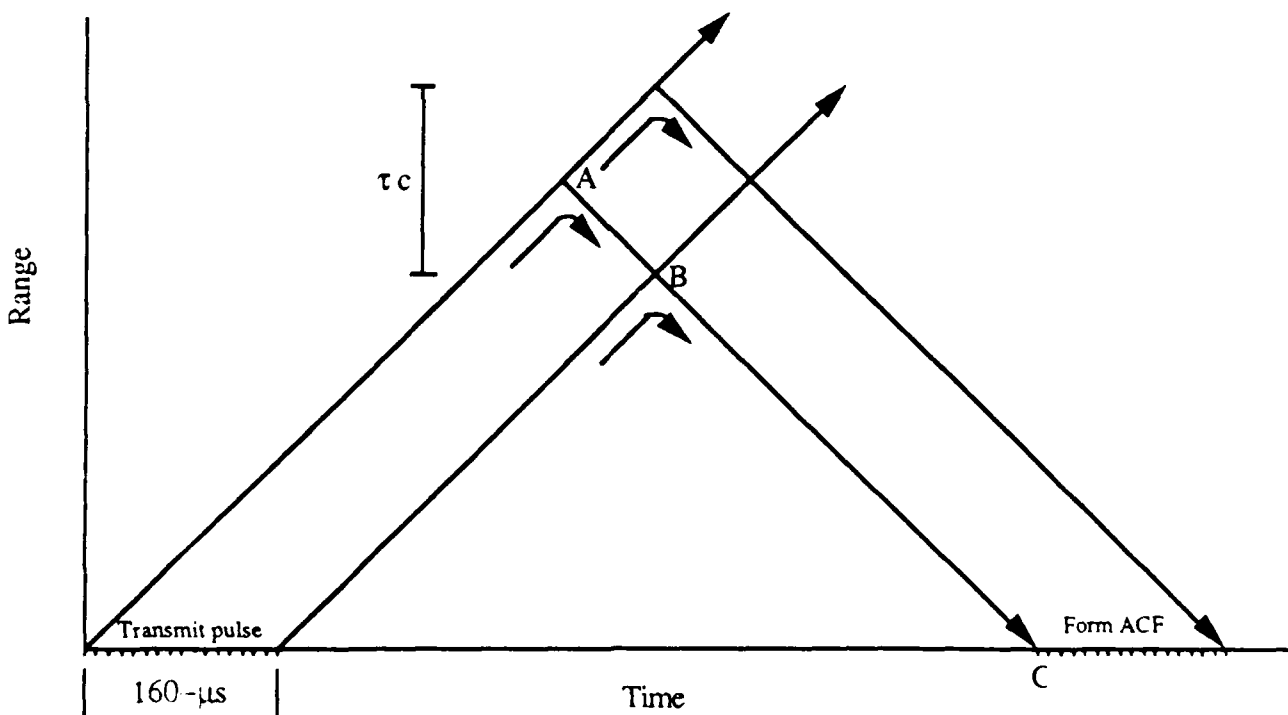
Figure 6 Range-time diagram. The radar transmits a pulse of 160-μs duration then 'listens' for backscattered returns. The time at which the radar detects backscattered radiation corresponds to the range from which the radiation was scattered. But for any particular instant in time, there is a range ambiguity of $\frac{\tau c}{2}$. For instance, at time C, there is backscattered radiation coming from anywhere along AB. An ACF formed using the 160-μs interval will have contributions from a range of length τc.
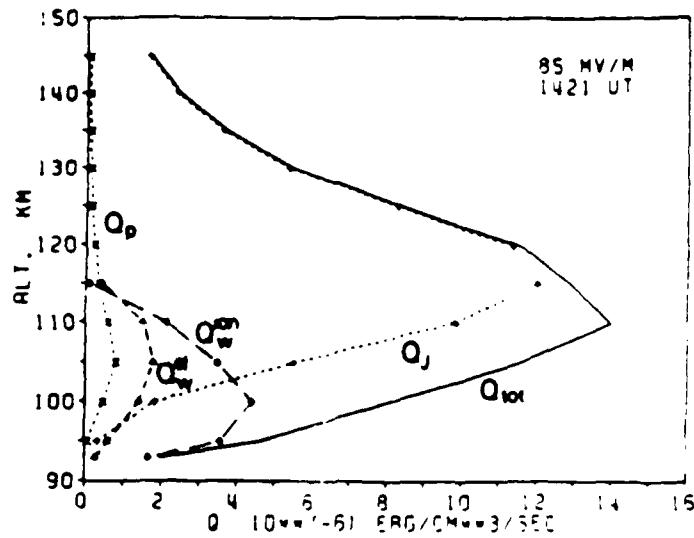
37

Figure 1.7   Comparison of different lower thermospheric heating rate profiles. Q_p is the heating caused by precipitating particles, Q_w^{el} is the electron heating caused by the unstable waves, Q_w^{ion} is the ion heating caused by the unstable waves, and Q_J is the Joule heating. Q_{tot} is the sum of all four. [St.-Maurice et al., 1981].
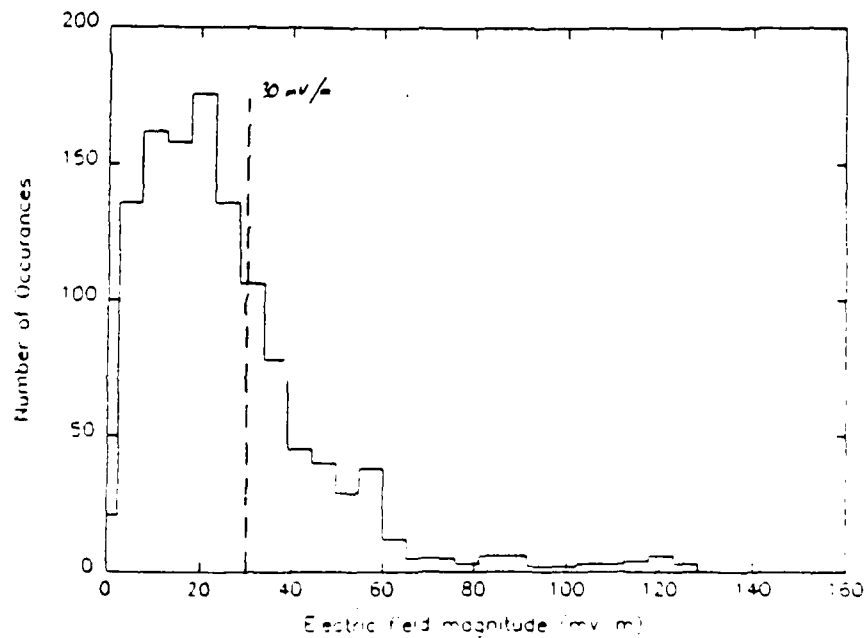

Figure 1.8   Histogram showing a probability distribution of electric field magnitude during LTCS-1. The threshold of 30 mV/m is indicated; periods with electric fields above this threshold were removed from the data before processing the collision frequencies. The distribution somewhat resembles a Chi-square distribution, as would be expected if both electric field vectors are assumed to be normally distributed.

Altitude (km)	Correlation Coefficient T_e vs $\mid E \mid$	Correlation Coefficient T_i vs $\mid E \mid$
104	0.568	0.427
109	0.709	0.556
115	0.797	0.838
121	0.653	0.842
126	0.574	0.851

Table 1.6   Correlation coefficient as a function of altitude for electron and ion temperature vs. electric field magnitude. The electron temperature has a highest correlation with $\mid E \mid$ at 115 km while T_i has the highest correlation at 126 km, the highest altitude in the Zone 1 fit. Anomalous heating of the electrons during elevated electric fields is expected to peak lower than the heating of ions by Joule heating. These results support this suggestion.
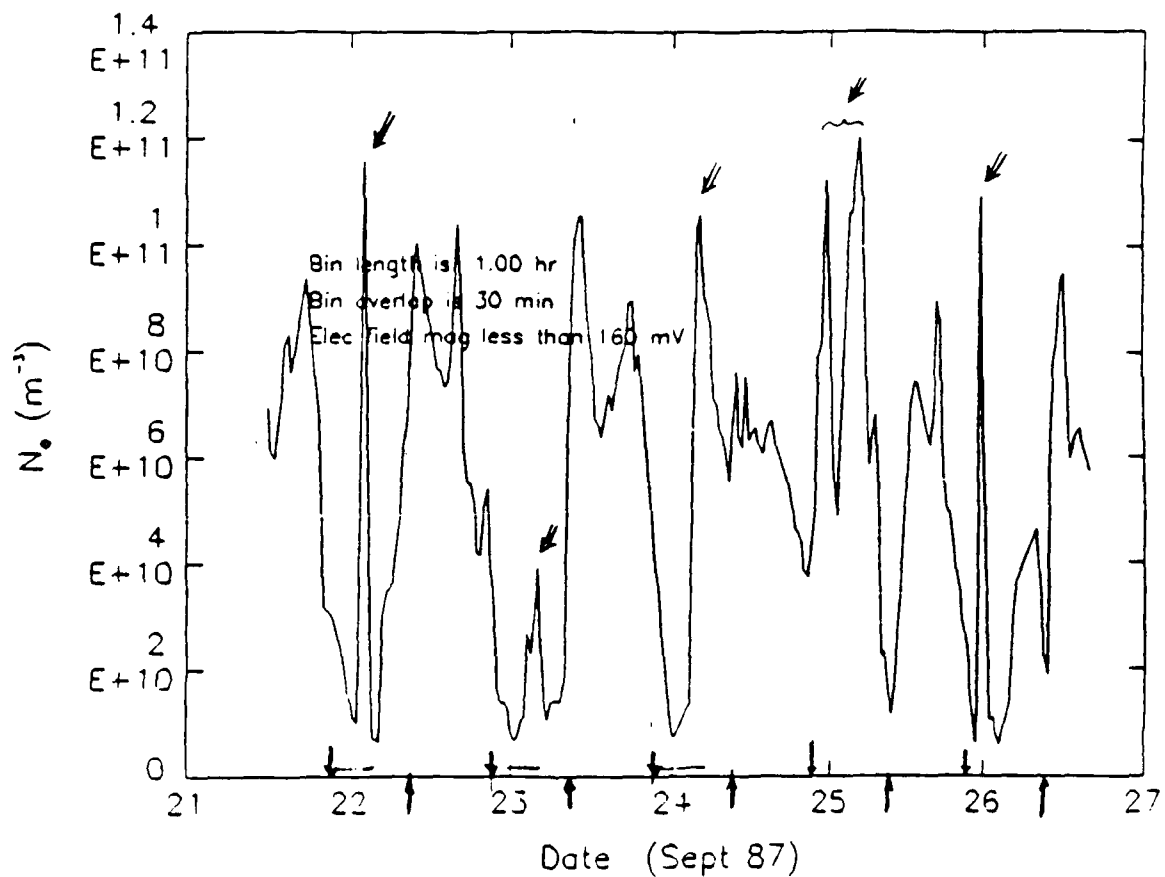
Figure 1.9   Electron density at 126 km as a function of time during LTCS-1. The arrows along the lower axis indicate local sunrise and sunset. Nighttime peaks in the electron density are also indicated by arrows. These periods of elevated electron density can correspond to particle precipitation events and have been removed from the data.
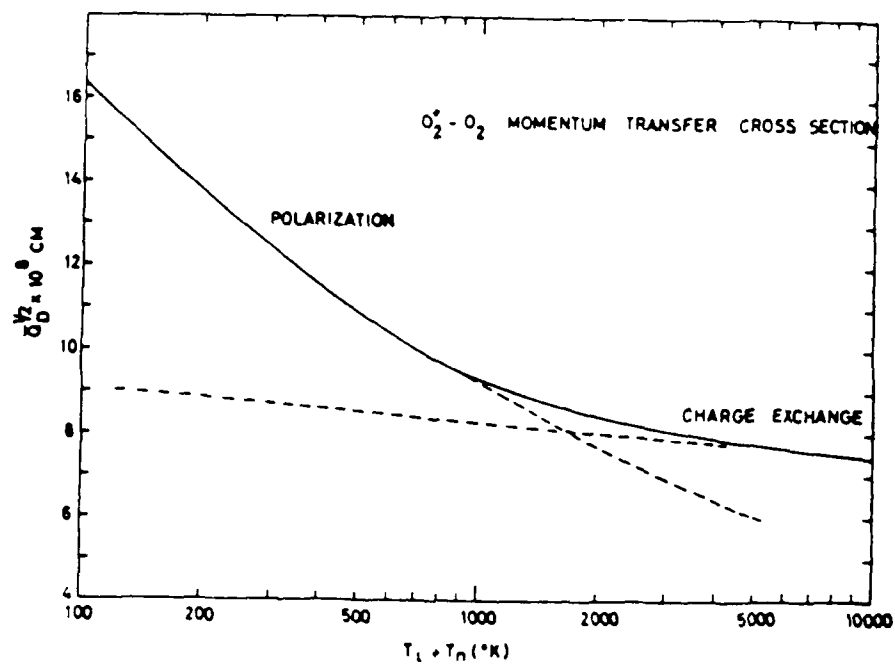
Figure 1.10 Momentum transfer collision cross section for O_2^+ - O_2 as a function of temperature. [Banks, 1966]
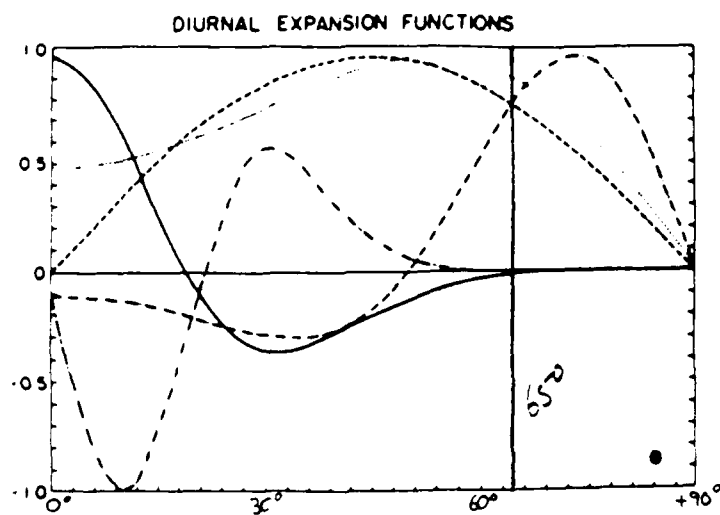
DIURNAL EXPANSION FUNCTIONS

Figure 1.11a Diurnal Hough modes. The approximate latitude of Chatanika and Sondrestrom is indicated. The key for the tidal modes is as follows: solid line (1,1), dashed line (1,-1), dotted line (1,-2), dashed-dotted line (1,-4), dashed-double dotted line (1,2). [Forbes, 1982a]

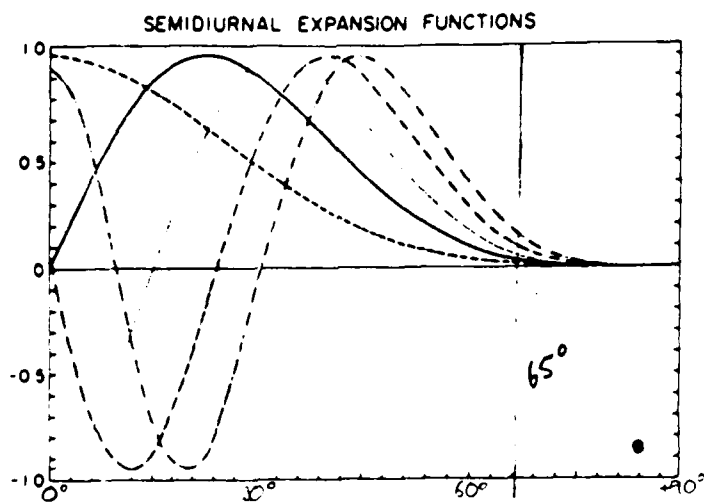**SEMIDIURNAL EXPANSION FUNCTIONS**

Figure 1.11b Semidiurnal Hough modes. The key is as follows: dashed line (2,2), solid line (2,3), dotted line (2,4), dot-dashed line (2,5), dashed-double dotted line (2,6).
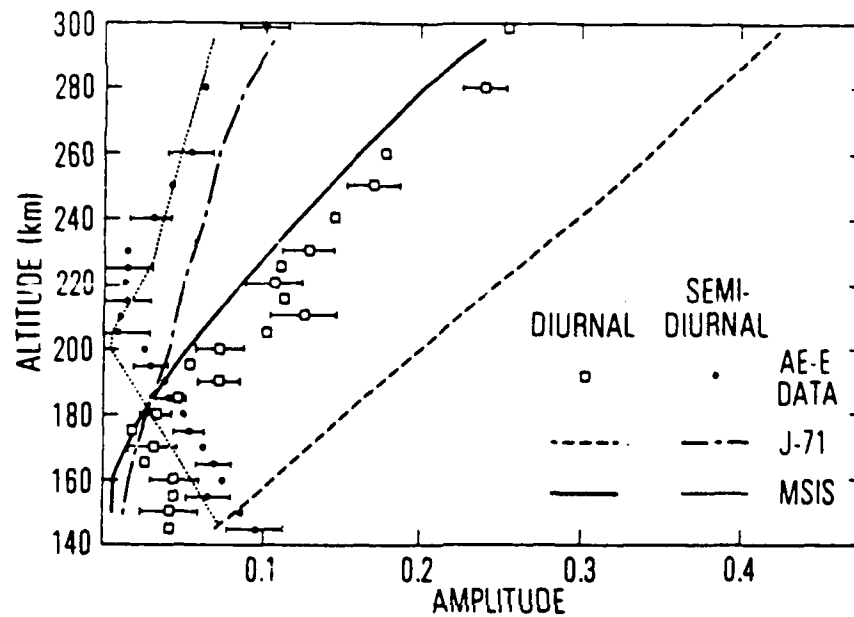
42

Figure 1.12   Amplitudes of the diurnal and semidiurnal components of the tides in the neutral density near the equator. The data is taken from the AE-E satellite. The semidiurnal tide is more important below 180 km while the diurnal tide predominates above 180 km. [Sharp et al, 1978]

Chapter 2   Lower Thermospheric Neutral Densities Determined From Sondrestrom Incoherent Scatter Radar During LTCS-1

2.1 Introduction

The lower thermosphere is a region of complex dynamics. Most thermospheric energy sources peak in this region, including solar EUV and UV absorption and variable high latitude heating sources [Killeen, 1987]. This solar absorption locally excites tides, which cause oscillations in the density, winds, and temperature. In addition, the lower thermosphere is subject to gravity waves and propagating tides which are excited in the stratosphere and mesosphere and travel upward into the lower thermosphere. Thus the neutral density, winds, and temperature of the lower thermosphere are far from constant; they reflect a very complex set of dynamic forcing. Most thermospheric models maintain a lower boundary near the mesopause, thus improved understanding of the dynamics of the lower thermosphere can lead to better boundary conditions for the models.

The Lower Thermospheric Coupling Study (LTCS) has the goal of studying the complex interactions within this region as well as with adjoining regions. Unfortunately, the lower thermosphere lies below the orbit of most satellites and has been relatively infrequently probed by rockets. However, the incoherent scatter technique is well suited to study the dynamics of this region [Evans, 1978; Johnson, 1990]. By analyzing the returned power spectra or autocorrelation function (ACF), one can, under certain circumstances, directly determine the electron density (n_e), ion and electron temperature (T_i and T_e), ion drift velocity (V_i), and ion composition [eg. Dougherty and Farley, 1963; de la Beaujardière et al., 1984]. One can additionally derive other ionospheric and thermospheric parameters including electric fields, neutral temperature, wind velocity and density. In the lower thermosphere, the incoherent incoherent scatter technique also allows the ion-neutral collision frequency (v_{in}) to be determined over a limited altitude range.

Below 90 km or so (depending on the radar wavelength and the electron density), the radar signal-to-noise ratio increasingly deteriorates with decreasing electron density, while above approximately 110 km, the effect of collisions on the scattered spectra becomes negligible. Within this altitude range, however, much can be learned about the dynamic behavior of v_{in} and the neutral density.

While a number of investigators have determined average profiles of v_{in}, very few have attempted to characterize the temporal variations observed in the collision frequency. There have been v_{in} observations from Arecibo [Wand and Perkins, 1968; Tepley and Mathews, 1978; Wand, 1976], Millstone Hill [Salah et al., 1975], Chatanika [Schlegel et al., 1980; Lathuillere et al., 1983], and EISCAT [Flå et al., 1985; Kofman and Lathuillere, 1985; Huuskonen et al., 1986; Kirkwood, 1986; Kofman et al., 1986; Nygrén et al., 1987, Huuskonen, 1989]. Daily oscillations of nin have been examined by Salah [1974] at Millstone Hill and by Kirkwood [1986] at EISCAT. In addition, neutral densities measured by the AE-E satellite have been examined for tidal fluctuations [Sharp et al., 1978; Forbes and Marcos, 1979]. This analysis was limited to equatorial regions above 140 km. We report here the first ion-neutral collision frequency measurements from the incoherent radar facility at Sondrestrom.

In the following section our data analysis technique is discussed, including the assumptions used in obtaining v_{in} from fits to the scattered spectra, the procedures used to discriminate against periods during which these assumptions are violated, and the formula relating v_{in} to neutral density. This discussion is followed by a presentation of the neutral density results. These include both average vertical profiles of neutral density and a tidal analysis of the neutral density over the LTCS-1 period. These results are compared with other experimental measurements and the predictions of tidal theory.

2.2 Data Analysis

2.2.1 Radar mode of operation

The Sondrestrom, Greenland incoherent scatter radar (67°N, 51°W, 74.5°Λ) took part in the first LTCS campaign [Johnson, this issue], collecting data from 1000 UT on 21 September until 1700 UT on 26 September 1987. It operated in a three-position azimuth mode allowing

45

determination of vector winds and electric fields. The radar transmission sequence consisted of a 60-μs pulse followed by 320-μs and two 160-μs pulses. The dual 160-μs pulse mode was used to probe the E-region with a range resolution of 24 km. The ACF's in the E-region were sampled from 92-126 km in 6 km range increments. The Sondrestrom radar does have another multipulse mode for sampling the E-region with a better range resolution. But the dual 160-μs pulse mode was selected because it gave a better signal-to-noise ratio and thus better data continuity. This continuity makes the data particularly valuable for examining the daily oscillations in the lower thermosphere. But the large range resolution is also a detriment because it introduces some degree of range smearing over the parameters to be determined.

The range smearing has the potential to be more important when determining collision frequencies (compared to temperatures or winds) because of their exponential decrease with altitude. Lathuillere et al. [1983] examined this problem for a Chatanika multipulse correlator having a range resolution of 9 km. They found that when determining v_{in} below 105 km, the error introduced through range smearing was always less than 15%. They also found that this error was most sensitive to the temperature and v_{in} profile, and less sensitive to electron density profile or windshear across the integration range.

2.2.2 Discriminating against periods of heating

Although it is theoretically possible to fit simultaneously for n_e, T_i, T_e, v_{in}, and V_i from the ion-line portion of the spectrum in the E-region, in practice, a four parameter fit generally provides the most satisfactory results. The effects of v_{in} and T_e/T_i on the spectrum are too similar for them to be separable given typical noise levels. The approach of the Sondrestrom software system is to make three separate fits for ionospheric parameters in the E-region (85 to 120 km) (see Table 1.5). The ion-neutral collision frequency is determined based on the assumption that the ion and electron temperatures are equal.

At low and mid-latitudes, the assumption that $T_i=T_e$ is usually valid, but at high latitudes there are a number of processes which will disturb the thermal equilibrium of the E-region. High particle precipitation can lead to elevated electron temperatures. During periods of high electric

46

fields both the ions or electrons can be preferentially heated - the ions through classical Joule heating processes, and the electrons through wave-particle interactions [St.-Maurice et al., 1981; Lathuillere et al., 1983]. During these periods of thermal disequilibrium, the assumptions made to derive v_{in} are invalid and the collision frequencies determined from the measurements should not be used.

Therefore, we have systematically identified and removed suspected periods of E-region heating from our data. This was done by examining the derived electric field magnitude, electron density, and upper E-region ion and electron temperatures. Figure 2.1 shows a scatter plot of the electric field magnitude vs ion temperature at 126 km for the LTCS-1 period. A close correlation is apparent between elevated electric field magnitude and elevated ion temperature, making the electric field magnitude a useful tracer of periods of heating. In the results that follow, we have set a threshold of 30 mV/m on the use of v_{in} values; periods with electric field magnitude above this threshold are removed from the data. The electron density has also been examined. By removing periods when the electron density is significantly elevated above 'normal' levels, particle precipitation events which may also disturb E-region thermal equilibrium have been eliminated. Finally T_i and T_e at 121 and 126 km were also visually examined for periods when $T_i \neq T_e$, that had not been accounted for above. Through this systematic elimination of periods of E-region heating, the geophysical conditions for the remaining ion-neutral collision frequencies are consistent with the assumptions required to derive them from the measurements.

Figure 2.2a shows the Kp index for 21-26 September. Two periods of enhanced activity occurred, one of relatively short duration between 22 and 23 September, and another of longer duration on 25 and 26 September. The electric field magnitude over Sondrestrom is shown in Figure 2.2b. The short period of higher Kp on 22-23 September is not reflected in the electric field. However, on 25-26 September, the electric field is highly elevated, reaching values over 100 mV/m. Because of the high activity on the 25th, we limited our examination of collision frequencies to the period of 21 24 September.

2.2.3 Determination of neutral densities from radar-derived ion-neutral collision frequencies

For the temperature range characteristic of the E-region, the most important ion-neutral collision mechanism is the induced-dipole interaction [Banks and Kockarts, 1973]. The data discrimination process described above removes periods of heating, and thus should prevent significant departures from these conditions in our altitude range of interest. Assuming an induced-dipole interaction for the momentum transfer cross section, one can show that the ion-neutral collision frequency for momentum transfer (relative to the laboratory frame of reference) is related to the neutral density by

$$v_{in} = \frac{2.59 \times 10^{-9}}{m_i} (\alpha_n \mu_{in})^{1/2} N_n$$

where α_n is the atomic polarizability of the neutral, μ_{in} is the reduced mass of the ion-neutral pair, and N_n is the number density of the nth neutral constituent [see Banks and Kockarts, 1973]. Summing over the primary neutral constituents of the lower thermosphere, N_2, O_2, and O, we obtain

$$v_{in} = \frac{2.59 \times 10^{-11}}{m_i} \left[\%(N_2)(1.76\mu_{iN_2})^{1/2} + \%(O_2)(1.59\mu_{iO_2})^{1/2} + \%(O)(0.79\mu_{iO})^{1/2} \right] \cdot N$$

where N is now the total neutral density, $\%(\ ) = \frac{N_n}{N}$ (x 100), and m_i is the mass of the ion species in amu. The primary ions in the E-region are NO^+ and O_2^+ with atomic masses 30 and 32, respectively, and assuming a single ion with intermediate mass will introduce minimal error. Taking this intermediate ion mass to be 30.5 amu (corresponding to 75% NO^+, 25% O_2^+), the total ion-neutral collision frequency is related to the total neutral density by

$$v_{in} = K \cdot N,$$

where $K = \frac{2.59 \times 10^{-11}}{30.5} \left[\%(N_2) \cdot 5.07 + \%(O_2) \cdot 4.98 + \%(O) \cdot 2.88 \right]$

[Lathuillere et al., 1983]. We have used the MSIS-86 model [Hedin, 1987] to estimate the relative populations of the three neutral species and thus the constant K. Due to the variation in the relative populations, especially the increase in $\%(O)$ with altitude, the constant K is observed to decrease

48

with altitude. Average values of K used in this study range from 4.28×10^{-10} cm^{3}sec^{-1} at 92 km to 4.10×10^{-10} cm^{3}sec^{-1} at 115 km. This variation of K with altitude has the effect of slightly lowering the neutral density scale height relative to the collision frequency scale height from which it is derived.

The values of K that we have used in this study are in reasonable agreement with other values that have been previously reported. For example, experimental values for N_2/O_2^+ collisions (in the laboratory frame of reference) range from 3.5×10^{-10} at 300 K to 2.7×10^{-10} at 1500 K [see Banks and Kockarts, 1973]. The constant used in the "EPEC" routine, which computes Joule heating and electric fields from Sondrestrom (and Chatanika) data is 3.75×10^{-10} [de la Beaujardière et al., 1984]. The Forbes tidal model estimates ion drag and Hall coefficients using $v_{in}/N = 4.9 \times 10^{-10}$ for a mean molecular weight of 28.5 [Forbes, 1982a.]. K has also been variously estimated as 4.5×10^{-10} and 3.8×10^{-10} [Wand, 1976; Flå et al., 1985].

2.3 Results and Discussion

2.3.1 Average vertical profile of neutral density

Figure 2.3 shows average vertical neutral density profiles for the period 21 - 24 September 1987. Average daily profiles are shown in the inset, while the main figure contains the four-day average profile with error bars superimposed. The error bars indicate the uncertainty of the mean computed by $\sigma_\mu = (1/\Sigma(1/\sigma_i^2))^{1/2}$, where σ_i are derived from the individual error estimates from the fit for the ion-neutral collision frequencies. Also shown on the plot is the MSIS-86 profile and two other models of the data. The solid line is a weighted least squares fit to the data assuming a constant scale height. The form $n(z) = n(z_0) \exp\{-(z-z_0)/H_s\}$ was used in this fit, where the reference altitude, z_0, is 100 km and $n(z_0)$ and H_s are determined by the least squares fit. The density at each altitude is weighted by the uncertainty of the mean at that altitude.

The dashed line is the Kirkwood 'winter' model [Kirkwood, 1986]. It is of the form $n(z) = n(z_0) - (1+\beta)(z-z_0)/H(z_0) + 0.5\beta(z-z_0))$, where the reference altitude is again 100 km, $\beta = \partial H/\partial z$, and $H(z_0)$ is the scale height at the reference altitude. This model allows a constant scale height gradient (and thus temperature change) through the altitude range of interest. The Kirkwood

49

'winter' model has $\beta=0.13$ and $H(z_0)=6.05$ km. The neutral density at the reference altitude is interpolated from the data.

The four day average profile is observed to show good agreement with all three models, at least up to 104 km. The constant scale height determined from the fit to our data is 5.5 km. The experimental data is also observed to curve upward, indicating an increasing scale height with altitude. This is not unexpected since the temperature in this altitude range increases with altitude, but it increases much more rapidly than predicted by the Kirkwood 'winter' model.

Some comments on possible sources of error in these profiles are in order. First of all, sometimes an average can be biased by the fact that data are not evenly represented over the period(s) of oscillation in the data. For instance, if a strong diurnal oscillation is present in the data with a minimum at midday, and if less data are present at night, then the mean over a 24-hour period will be lower than it should be. Because this is the case on 23 September at 98 and 104 km, this may explain why the averages are so low at these heights on this day.

A second source of possible error comes from the fact that above 110 km collisions have an increasingly small effect on the incoherent scatter spectra, and the collision frequency can no longer effectively be determined. It appears that as the effect of collisions on the spectra diminishes, the collision frequencies are increasingly overestimated. Thus while one would expect to see the scale height increasing with altitude as observed, this trend may be overestimated, especially above 105 km. A possible explanation for the tendency to overestimate the collision frequency with increasing altitude is the range smearing effect discussed above. The simulation of range smearing by Lathuillere et al. [1983] does indicate an increasing overestimation of collision frequency with height, but the effect is fairly small. In our case the effect may be more pronounced due to our larger range resolution. However, it is very encouraging to note that despite the large range resolution of our measurements, we do seem to obtain very reasonable estimates of the neutral density between 90-105 km.

2.3.2 Tides in the neutral density

Having examined the average neutral density profile for LTCS-1, we now turn to an examination of the time varying behavior of the neutral density. As mentioned briefly above, the lower thermosphere is strongly affected by a number of dynamic influences. Solar insolation can locally excite diurnal and semidiurnal tides. Solar absorption by ozone in the mesosphere also excites tides below thermospheric altitudes which can propagate upwards. Gravity waves can also propagate into the thermosphere from below.

Most propagating diurnal waves tend to interfere destructively due to their smaller vertical wavelength, thus the diurnal tides are essentially limited to their region of excitation [Fesen, et al., 1986]. An exception is the propagating (1,1) mode which is quite large at the lowest levels of the thermosphere but is dissipated by about 105 km. Semidiurnal modes excited in the mesosphere amplify as they propagate upwards into the thermosphere, and continue to amplify until molecular viscosity, thermal conduction, and ion drag begin to damp their growth above about 150 km. Analysis of AE-E neutral densities revealed that in the equatorial regions, the oscillations of the neutral density change from predominantly diurnal above 180 km to predominantly semidiurnal below this altitude [Sharp et al., 1978; Forbes and Marcos, 1979].

Our density data has been examined at the altitudes of 92, 98, 104, and 109 km. Figure 2.4 shows a time sequence of neutral density for the period 21-24 September. The data has been averaged in bins of 3-hour duration, with a bin spacing of 1 hour and a weighted mean calculated for each bin. The error bars represent the uncertainty of the mean as described above. Most notable is the large amplitude of the observed oscillations. Also evident is the sinusoidal nature of the variation; the diurnal variation at 98 km is very obvious. In order to characterize the tidal oscillations that appear to be present in the data, we have performed a linear regression fit to a sinusoidally varying function at each altitude. Specifically, the data is fit to $f(t)=a_0+a_1\cos \omega_1 t +b_1\sin \omega_1 t+a_2\cos \omega_2 t+b_2\sin \omega_2 t$, where $\omega_1=\frac{2\pi}{1 \text{ day}}$ and $\omega_2=\frac{2\cdot 2\pi}{1 \text{ day}}$. The linear regression is performed by the routine REGRESS [Bevington, 1969] using instrumental uncertainties to weight the fits. From the coefficients, we derive amplitudes and phases (local times of maximum) for the diurnal and semidiurnal oscillations.

The result of the fit at each altitude is displayed in Figure 2.5. Here the data have been binned by universal time with a bin size of 2 hours and bin spacing of 1 hour. The universal-time binned plots reinforce the visual evidence of the oscillatory nature of the density fluctuations. The curves are seen to represent the density fluctuations very well. Figure 2.6 is a summary of the parameters obtained from the fit to the data. On the left is the amplitude of the diurnal and semidiurnal oscillations at each altitude. Also displayed as X's are the ratio of each amplitude to the constant term determined from the least squares fit ($100 \cdot a_i/a_0$). On the right is the local time of maximum for each oscillation and altitude. Uncertainties in the amplitudes and phases have been determined using error propagation techniques from the uncertainties in the coefficients obtained from the weighted fit.

Some interesting observations can be made from these results. The amplitude of the diurnal tide appears roughly equivalent to the amplitude of the semidiurnal tide. This is surprising since the semidiurnal tide is expected to be dominant in this altitude interval [Forbes, 1982a,b]. The amplitudes of the tides are roughly constant with height, but as a percent of the mean, the amplitudes steadily increase with altitude up to 105 km and then show a decline (although our confidence in our values at 109 km and above is low).

The phase of the diurnal tide shows an interesting shift of approximately 12 hours between 92 km and 98 km, and then remains roughly constant with height, as is expected for a nonpropagating tide. The phase of the diurnal tide near 90 km could be influenced by a propagating diurnal mode. The phase of the semidiurnal tide shows a regression with altitude indicative of an upwardly propagating mode.

Kirkwood [1986] has also examined tides in the high latitude lower thermosphere from EISCAT. Oscillations in the temperature, southward wind and neutral density were analyzed for their semidiurnal tidal component during periods in January, May, August, and November 1985. The neutral density amplitudes (as a percent of the mean) and local time of maximum were presented for all four periods between the altitudes of 90-105 km. Comparison with our tidal results reveals some encouraging similarities. The local time of maximum of the semidiurnal tide

agrees with our results within the uncertainties of our measurements, showing a very similar regression with altitude. Their amplitudes, on the other hand, remain roughly constant with height and do not exceed 15%. Our amplitudes (as a percent of the mean) increase from 5% at 92 km to close to 30% at 104 km. They did not present the amplitudes and phases of the diurnal component of the tides in the neutral density.

Salah [1974] presents a sequence of eight hours worth of neutral densities derived from radar measurements at Millstone Hill on 14 April 1971. The data presented was obtained from altitudes between 107-119 km. While no tidal analysis was performed on the density data, it was observed that the fractional amplitude of the density oscillations was roughly twice that observed in the temperature oscillations, or 20-30%. This is in very good agreement with our observations.

Fesen et al. [1986] described modifications to the National Center of Atmospheric Research thermospheric-ionospheric general circulation model (TGCM), by which the upward propagating semidiurnal tide is modeled as a perturbation to the lower boundary conditions. Recently, the TGCM was updated to incorporate a self-consistent ionosphere [Roble et al., 1988], and is now referred to as the Thermosphere/Ionosphere General Circulation Model (TIGCM). We have compared our tidal analysis of the neutral densities from LTCS-1 with a similar analysis performed on TIGCM neutral densities calculated over Sondrestrom for the same period [Fesen and Roble, this issue]. Excluding data from the model's lower boundary at approximately 97 km, which is constrained to an imposed semidiurnal geopotential oscillation, we have compared the radar and model results between 100 and 110 km.

Figure 2.7 contains the results of our tidal analysis of the TIGCM neutral densities superimposed on our experimental results. The amplitudes of both the diurnal and semidiurnal tides in the model densities are between 1 and 2 orders of magnitude smaller than the observed amplitudes, but this may be due to the proximity of the model's lower boundary [Fesen and Roble, this issue]. The phases of the model and radar data show very similar behavior with height. The local time of maximum of the model diurnal tide is roughly constant with height between 100-110 km at 0600 LT. The diurnal phase of the data is also roughly constant with height but

approximately 8 hours earlier than that predicted by the model. The semidiurnal phases of the model and data show remarkable agreement. They are virtually parallel between 100-110 km, with our data running approximately 2 hours earlier than the model, well within the uncertainties of our measurements.

2.4   Conclusions

Our study is the first examination of collision frequencies from Sondrestrom, and only the second to analyze the tidal behavior of the neutral density. We have described a technique for deriving neutral densities from radar derived ion-neutral collision frequencies in the lower thermosphere. The polar E-region is subject to processes which can disturb the thermal equilibrium among the neutrals, ions, and electrons. Since the collision frequencies are derived based on the assumption that $T_i = T_e$, we have carefully filtered out periods when this assumption was violated. The neutral density was derived from the collision frequency assuming an induced dipole interaction between the ions and the neutrals, a single ion of intermediate mass, and allowing for the variation of relative neutral composition with altitude.

We have found that our average neutral densities agree very well with MSIS-86 below 105 km. This is encouraging given the large range resolution of the radar measurements. There appears to be a tendency to overestimate increasingly the neutral density with altitude above 105 km, which may result from range smearing effects.

The tidal analysis of the neutral density indicates that the amplitude of the diurnal mode is about the same magnitude as the amplitude of the semidiurnal mode. The amplitude of both (as a percentage of the mean) is observed to increase with altitude up to 105 km. The phase of the semidiurnal tide is observed to shift to earlier local times with increasing altitude indicative of a vertically propagating mode. The phase of the diurnal tide remains roughly constant with height above 98 km. The phase of the semidiurnal tide shows excellent agreement with previous observations from EISCAT and with the predictions of the NCAR TIGCM. However, the amplitudes of the semidiurnal tide determined from this contiguous interval are greater than those observed in the EISCAT data set.

We intend to extend this technique to a large incoherent scatter radar data base, obtained when the radar currently located in Sondrestrom was in Chatanika, Alaska, in order to further clarify the tidal behavior of the lower thermospheric neutral density. This data will be examined for any seasonal effects, and will be further compared with the predictions of tidal theory.
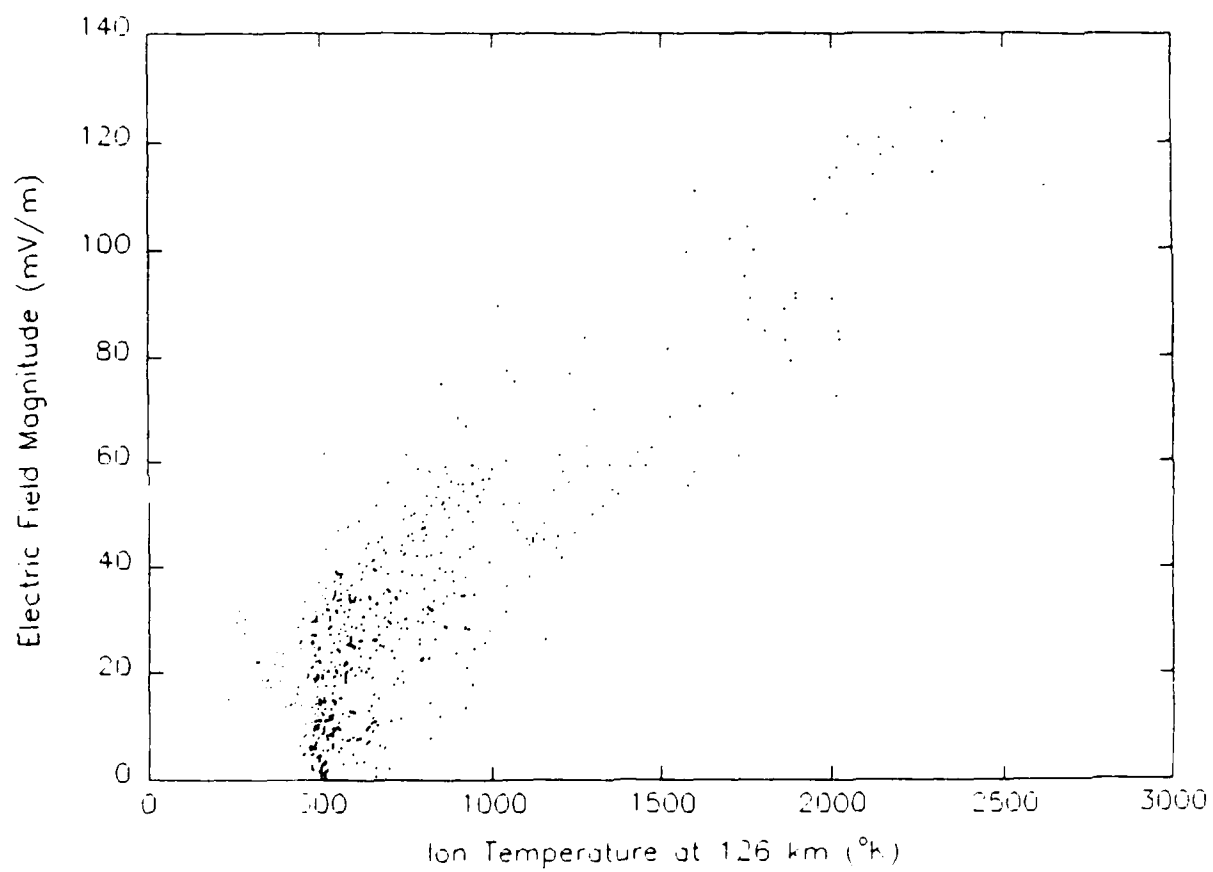
Figure 2.1 Scatter plot of ion temperature at 126 km vs. electric field magnitude at Sondrestrom for the LTCS-1 period. The linear correlation coefficient is 0.85.

56
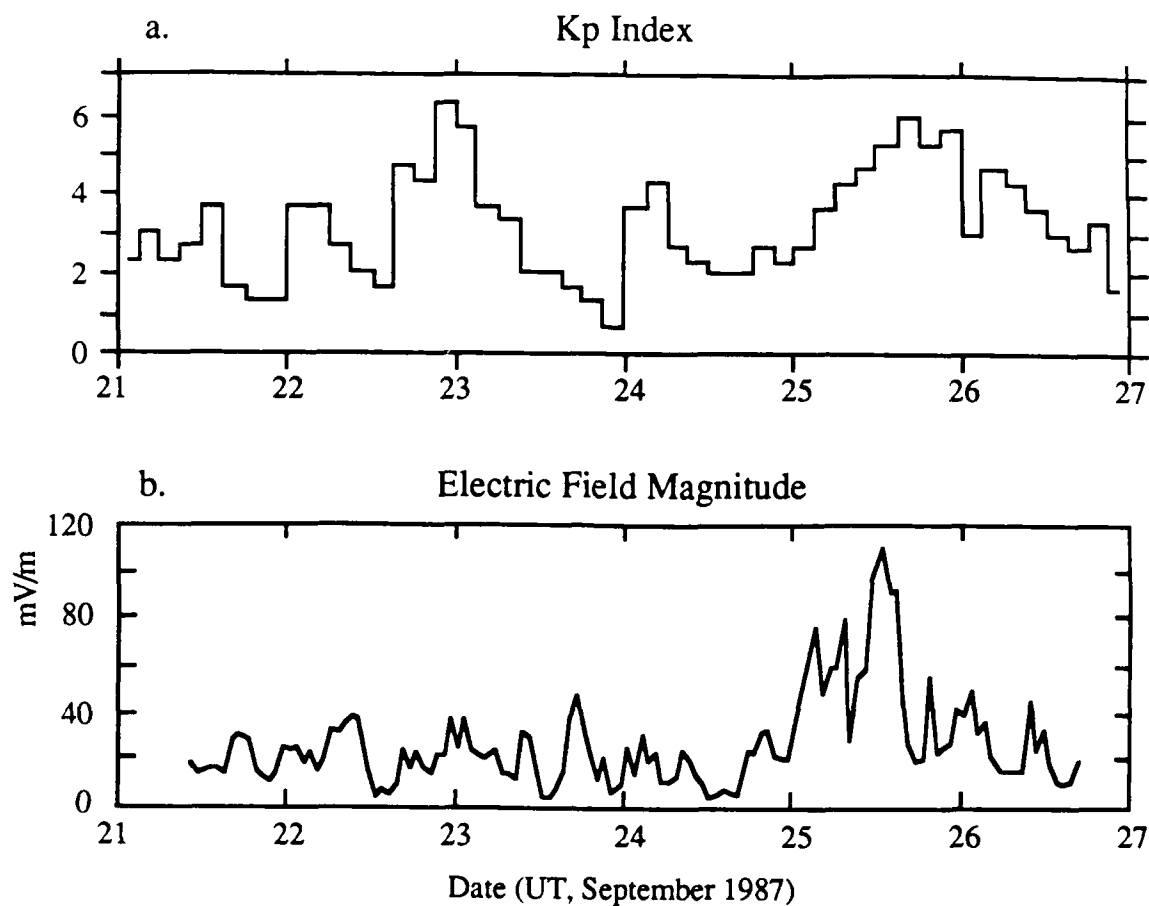
Figure 2.2 Geomagnetic activity during LTCS-1. (a) The Kp index shows two periods of activity; one of shorter duration on 22-23 September, followed by a longer period beginning on 25 September. (b) Only the activity beginning on 25 September was reflected in the electric field magnitude over Sondrestrom, during which values exceeded 100 mV/m.
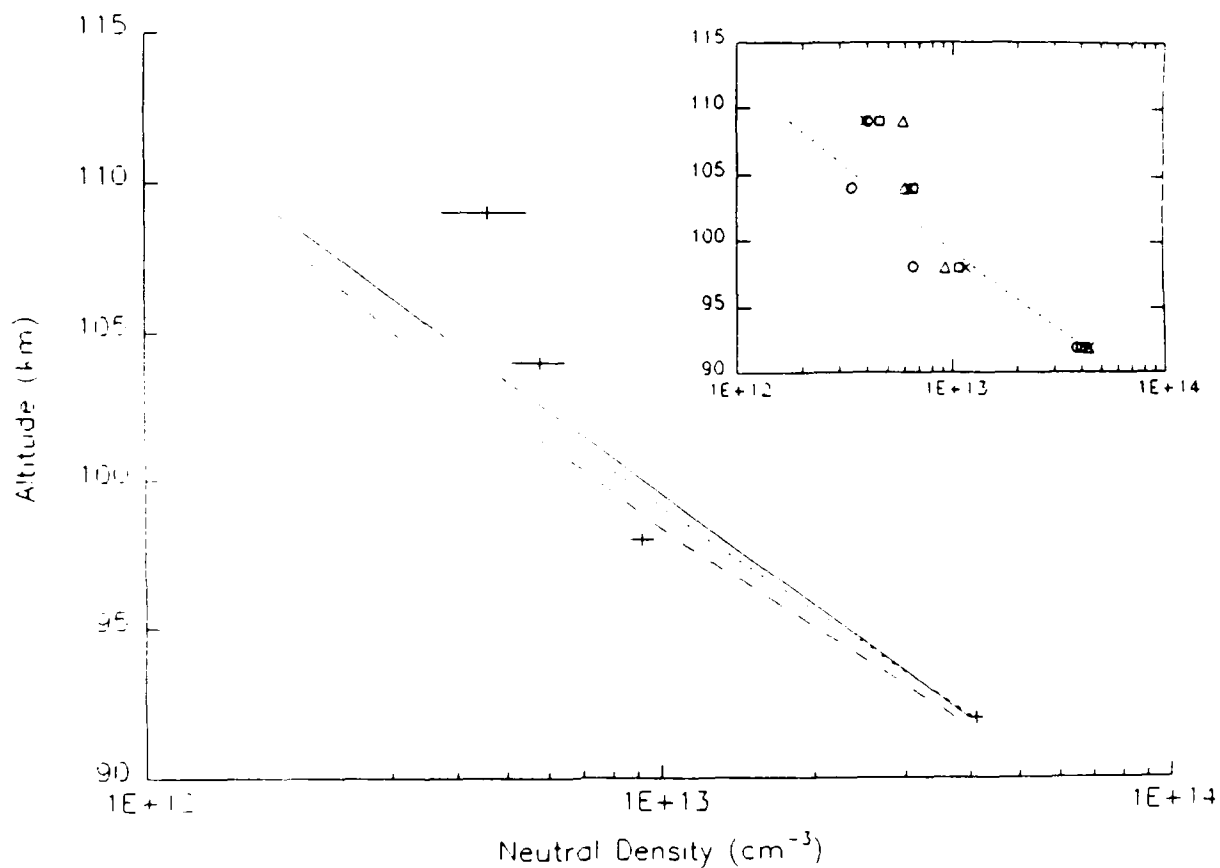
Figure 2.3 Four day average vertical profile of neutral density for 21-24 September. The dotted line is the density predicted by MSIS-86, the dashed line is from the *Kirkwood* [1986] 'winter' model, while the solid line is a weighted least squares fit to our data assuming a constant scale height. The scale height resulting from the fit to our data is 5.5 km. (Insert) Averages for each day of the LTCS-1 period. 'Δ' = 21 September, 'Δ' = 22 September, 'O' = 23 September, and 'X' = 24 September. The dotted line is again from MSIS-86.
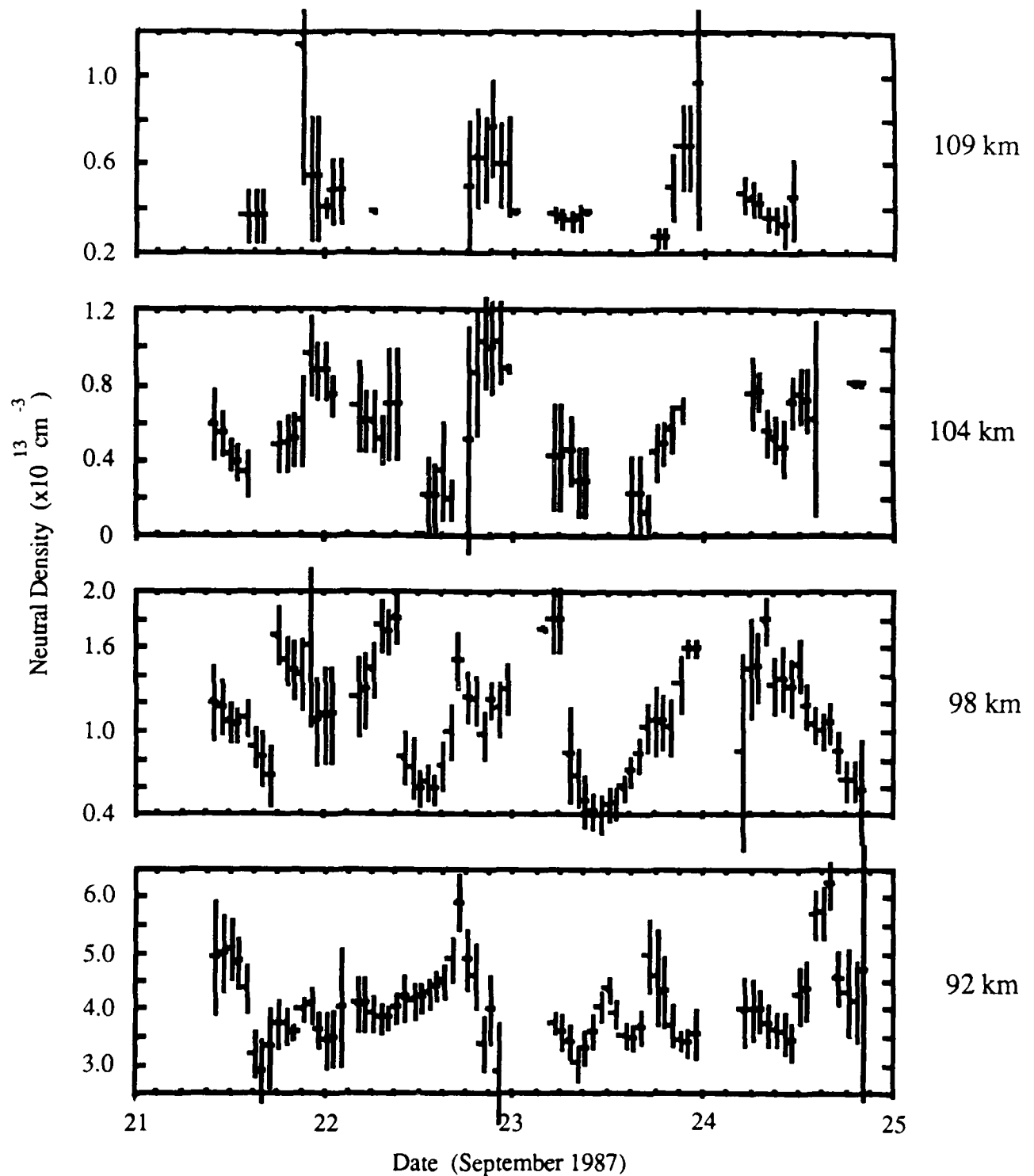
58

Figure 2.4 Neutral density as a function of time for 21-24 September 1987. Panels each contain data for a different altitude from 92 to 109 km. Notice the large amplitude of the oscillations as well as their sinusoidal character. More 'holes' in the data are apparent in the higher altitudes, especially at 109 km. This leads to greater uncertainty in the tidal fit to the data.
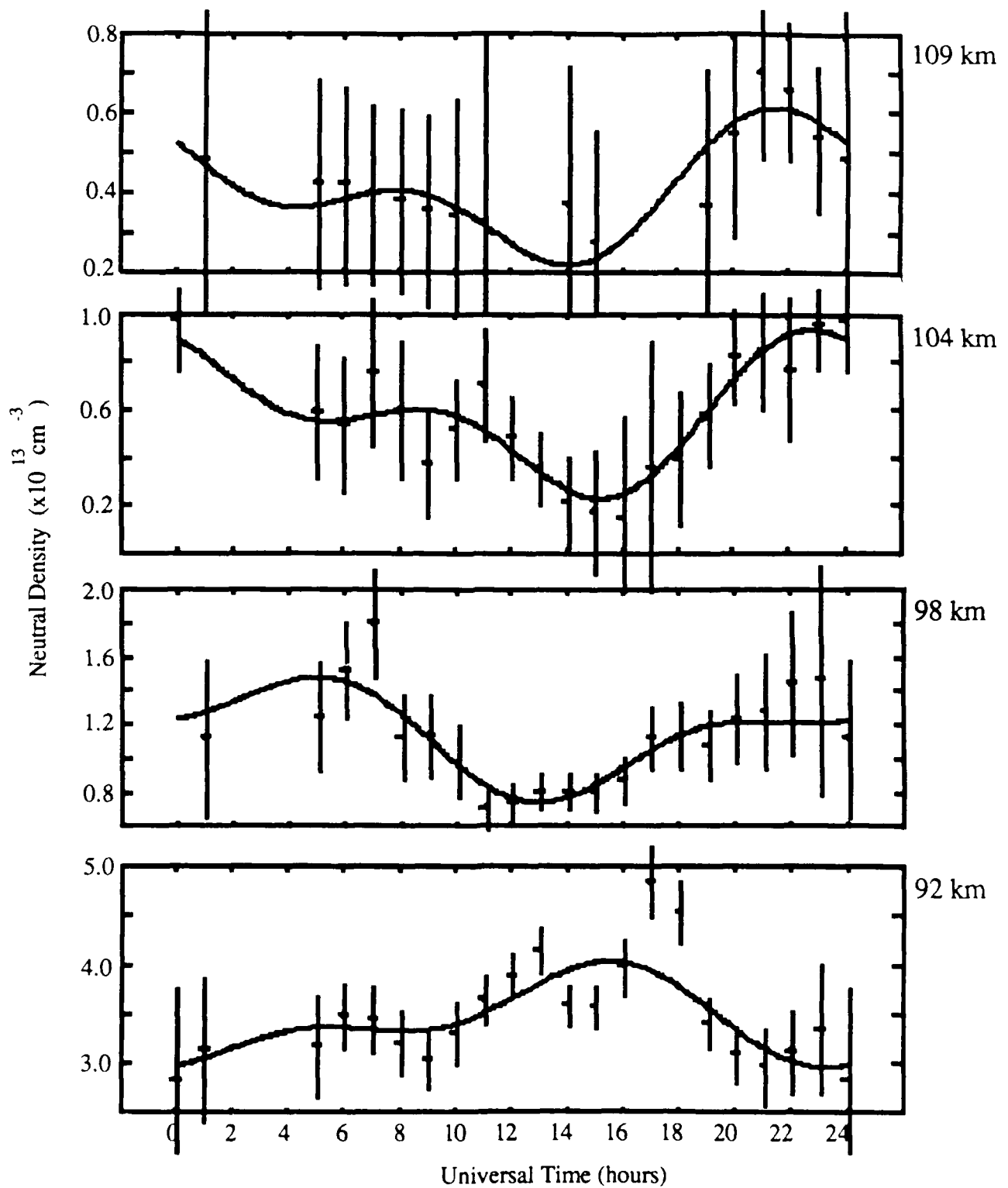
59

Figure 2.5 Same as Figure 2.4 except now the density has been binned by universal time of day. Superimposed on the data is the diurnal and semidiurnal fit to the data.
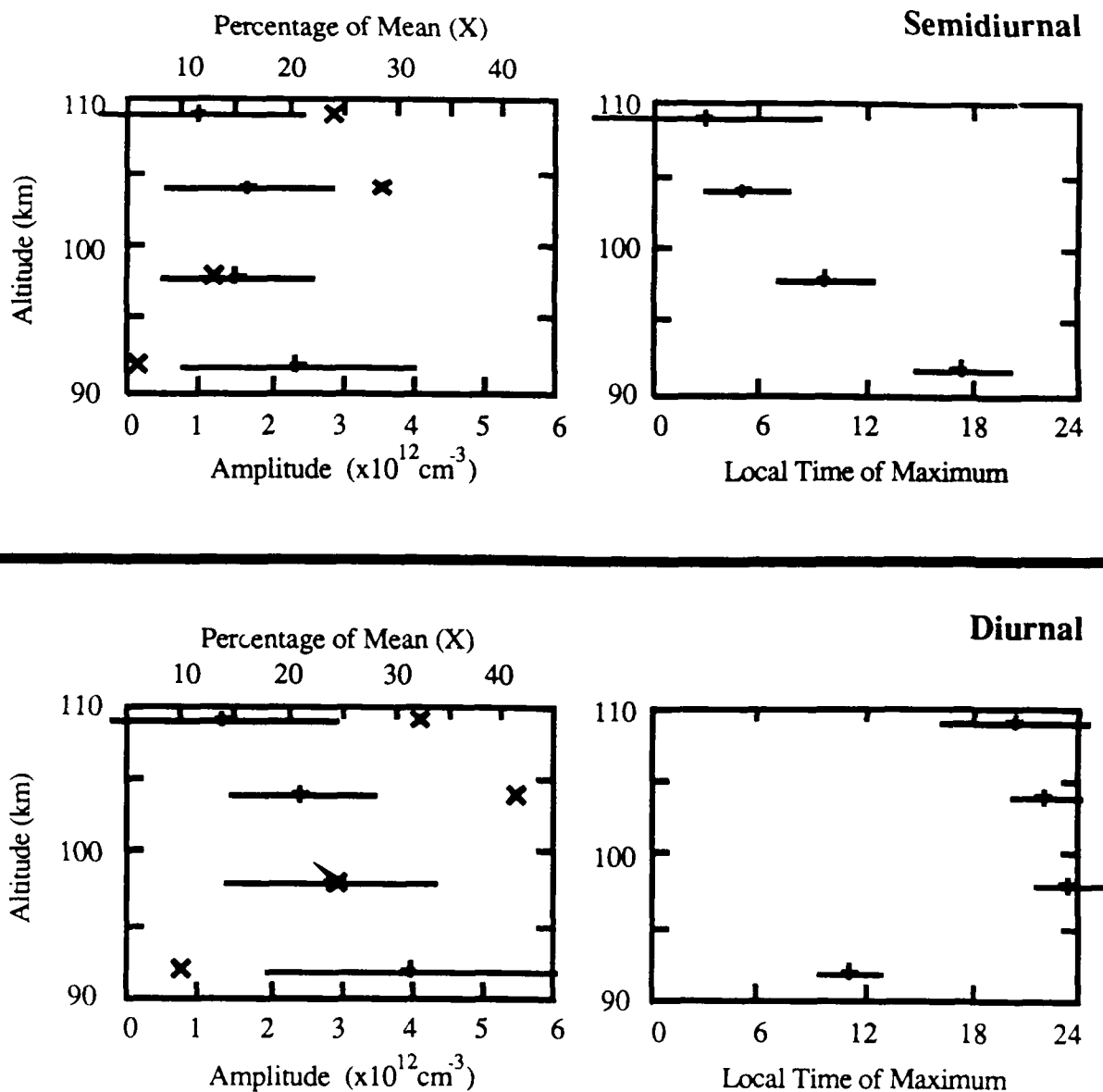
Figure 2.6 Summary of the tidal fit to the data. The amplitude and phase of the semidiurnal oscillation is shown in the top two panels, while the same for the diurnal oscillation is in the bottom two panels. On the left in each case is the amplitude of the oscillations. The amplitudes (shown with error bars) correspond to the scale on the bottom of each figure on the left. Also displayed on the left are the amplitudes as a percentage of their mean. These are plotted as X's and correspond to the scale at the top of each figure on the left. On the right are the phases of the oscillations, presented as the local time of maximum.
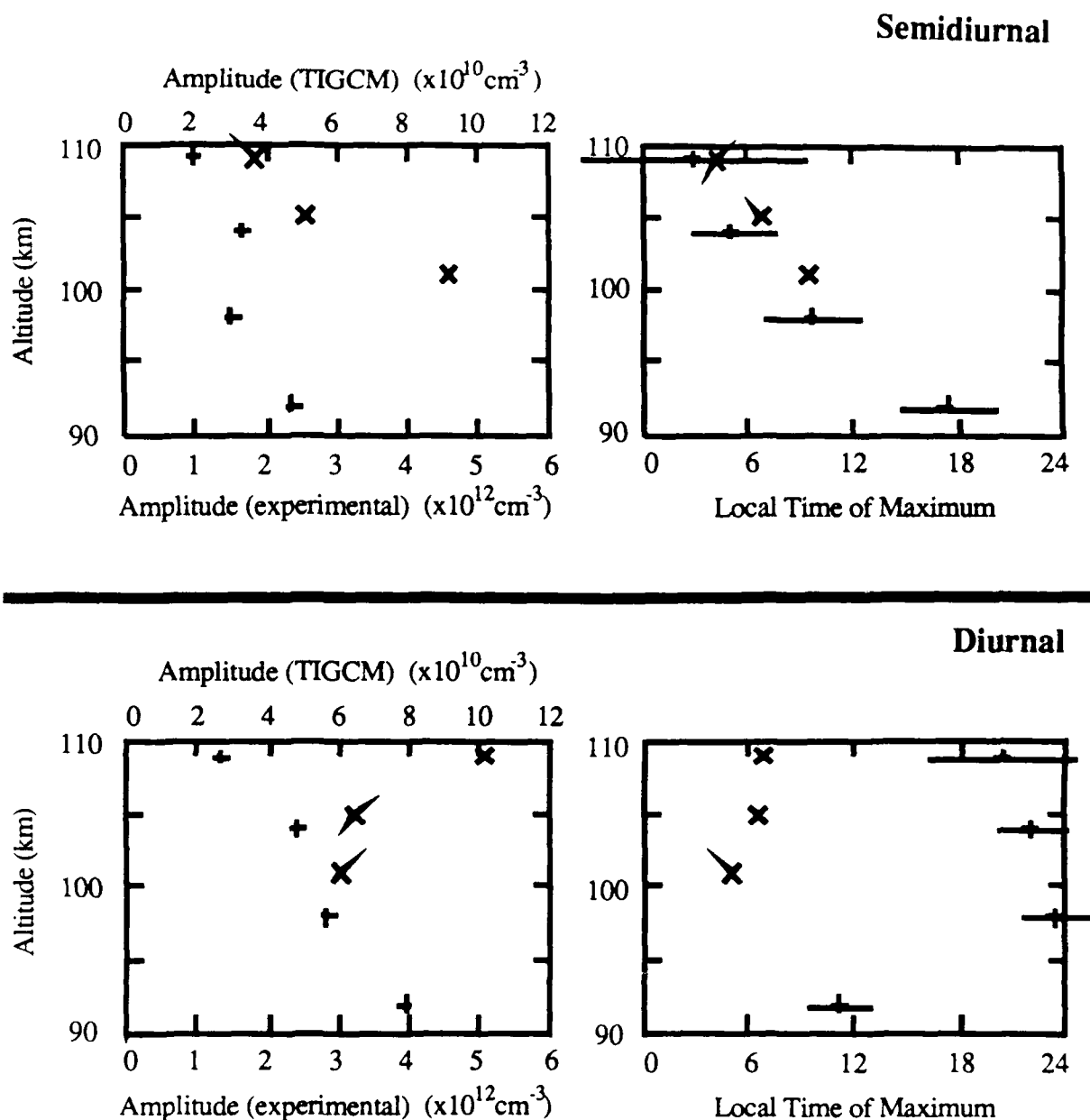
61

Figure 2.7   Comparison of oscillations in TIGCM neutral density with the experimental results. Format is the same as Figure 2.6, except now X's correspond to the amplitudes and phases of TIGCM neutral density tidal components. Two different scales have again been used in the left-hand panels. The bottom scale corresponds to the experimental amplitudes (+'s), while the top scale corresponds to the model amplitudes (X's). Note the difference of two orders of magnitude between the multiplicative factor on the top versus the bottom. ·ue to this difference in scaling, the error bars have been omitted from the experimental amplitudes. However, they have been included with the experimental phases because the scales of the model and experimental phases is the same.

Chapter 3   Long Term and Seasonal Variations of Lower Thermospheric Neutral Densities Determined from Chatanika Incoherent Scatter Radar

3.1 Introduction

There have been relatively few measurements of lower thermospheric neutral densities. This region lies below the orbits of most satellites, and has been relatively infrequently probed by rockets [e.g. Offerman et al., 1981]. However, the region is ideally suited for measurement by incoherent scatter radar. In the lower thermosphere, the ion-neutral collision frequency (v_{in}) can be determined over a limited altitude range (~90-110 km) from the backscattered power spectra or autocorrelation function (ACF) of the radar. The collision frequencies can be used to derive the total neutral number density.

There have been previous v_{in} observations from various radar facilities, including Arecibo [Wand and Perkins, 1968; Tepley and Mathews, 1978; Wand, 1976], Millstone Hill [Salah et al., 1975], Chatanika [Schlegel et al., 1980, Lathuillere et al, 1983], EISCAT [Flå et al., 1985; Kofman and Lathuillere, 1985; Huuskonen et al., 1986; Kirkwood, 1986; Kofman et al., 1986; Nygrén et al., 1987, Huuskonen, 1989], and Sondrestrom [Reese et al., 1990].

Tidal oscillations in the lower thermospheric neutral density have been examined by only two investigators. Kirkwood [1986] derived the amplitudes and phases of the semidiurnal tides observed in the v_{in} oscillations at EISCAT for 2-day periods in January, May, August, and November 1985. Reese et al. [1990] derived the amplitudes and phases of both the diurnal and semidiurnal tidal components in the neutral density at Sondrestrom during the LTCS-1 period (21-26 Sep 1986). This study uses the same techniques described in that earlier work but on a much more extensive data base.

In this study, data from the Chatanika, Alaska incoherent scatter radar facility is examined. The Chatanika radar was in operation from 1971 until 1982, at which time it was relocated to its

63

present location at Sondrestrom, Greenland. The radar periodically operated in a 'synoptic' mode, during which it collected data in both the E- and F-region for 24-hour periods. Between 1976 and 1982, there were at least 50 days of data collected in this manner.

It is the purpose of this paper to analyze the ion-neutral collision frequencies (v_{in}) from this large set of data. After eliminating periods of E-region heating from the data, neutral densities are calculated from the collision frequencies. Average vertical profiles of neutral density are examined for seasonal as well as solar cycle effects. In addition, the diurnal and semidiurnal components of the tidal oscillations in the neutral density are calculated for the different seasons.

Table 3.1 summarizes the data examined in this study. The days of radar operation are tabulated, as well as the 'season', the radar multipulse type, and the geophysical Ap index. The seasonal boundaries have been set to reflect the rapidity of the equinox transition, with spring and autumn being of shorter duration than summer and winter. spring and autumn are approximately 66 days long centered on the equinoxes, while summer and winter are approximately 116 days in duration centered on the solstices.

3.2 Radar Mode of Operation

The Chatanika incoherent scatter radar was located near Fairbanks, Alaska at 65.1°N, 147.5°W, and has been discussed in detail by de la Beaujardiere et al. [1984]. The radar operated at a frequency of 1290 MHz, which effectively limited determination of ion-neutral collision frequency to altitudes below approximately 110 km [Johnson, 1990]. For all the 'synoptic' days analyzed in this study, the antenna operated in a three position mode allowing determination of vector ion drifts from which neutral winds and electric fields could be calculated.

There were two multipulse modes used to obtain autocorrelation functions (ACFs) from the E-region. The first, used predominantly before 1980, was a dual 160-μs mode having a range resolution of approximately 24 km. The second consisted of a single 60-μs pulse followed by a burst of three 60-μs pulses. This 60-μs mode had an effective range resolution of approximately 9-km.

Using an iterative nonlinear least squares fitting routine, geophysical parameters are determined from the experimental ACFs. In the E-region, three separate fits are made from each ACF. In one fit, the ν_{in} is taken from a model and the ion and electron temperatures (T_i and T_e) are determined separately. In another fit, the ion-neutral collision frequency is determined based on the assumption that $T_i = T_e$. The results of this fit are those analyzed in this study. Because at latitudes there are heating processes which can disturb thermal equilibrium at E-region heights, we have removed intervals of such heating from the data set prior to analysis.

3.3 Data Analysis

3.3.1 Discriminating against periods of heating

There are a number of processes that can disturb the thermal equilibrium of the E-region in high latitudes. For instance, high particle precipitation can lead to elevated electron temperatures. In addition, during periods of high electric fields both the ions or electrons can be preferentially heated - the ions through classical Joule heating processes, and the electrons through wave-particle interactions [St.-Maurice et al., 1981; Lathuillere et al., 1983]. During these periods of thermal disequilibrium, the collision frequencies cannot be reliably determined from the radar measurements.

Therefore, we have systematically identified and removed periods of suspected E-region heating from our data. This was done by examining the derived electric field magnitude, electron density, and upper E-region ion and electron temperatures. In the results that follow, we have set a threshold of 25 mV/m on the use of ν_{in} values; periods with electric field magnitude above this threshold are removed from the data. The electron density has also been examined. By removing periods when the electron density is significantly elevated above its normal photoionization levels, particle precipitation events which may also disturb E-region thermal equilibrium have been eliminated. Finally the ion and electron temperatures from the upper E-region were also visually examined for periods when $T_i \neq T_e$, that had not been accounted for above. Through this systematic elimination of periods of E-region heating, the geophysical conditions for the remaining ion-neutral

collision frequencies are consistent with the assumptions required to derive them from the measurements.

3.3.2 Determination of neutral densities from radar-derived ion-neutral collision frequencies

For the temperature range characteristic of the E-region, the most important ion-neutral collision mechanism is the induced-dipole interaction [Banks and Kockarts, 1973]. The data discrimination process described above removes periods of heating, and thus should prevent significant departures from these conditions in our altitude range of interest. Assuming an induced-dipole interaction for the momentum transfer cross section, one can show that the ion-neutral collision frequency for momentum transfer (relative to the laboratory frame of reference) is related to the neutral density by

$$\nu_{in} = \frac{2.59 \times 10^{-9}}{m_i} (\alpha_n \mu_{in})^{1/2} N_n$$

where α_n is the atomic polarizability of the neutral, μ_{in} is the reduced mass of the ion-neutral pair, and N_n is the number density of the nth neutral constituent [see *Banks and Kockarts*, 1973]. Summing over the primary neutral constituents of the lower thermosphere, N_2, O_2, and O, we obtain

$$\nu_{in} = \frac{2.59 \times 10^{-11}}{m_i} \left[\%(N_2)(1.76\mu_{iN_2})^{1/2} + \%(O_2)(1.59\mu_{iO_2})^{1/2} + \%(O)(0.79\mu_{iO})^{1/2} \right] \cdot N$$

where N is now the total neutral density, $\%( ) = \frac{N_n}{N}$ (x 100), and m_i is the mass of the ion species in amu. The primary ions in the E-region are NO^+ and O_2^+ with atomic masses 30 and 32, respectively and assuming a single ion with intermediate mass will introduce minimal error. Taking this intermediate ion mass to be 30.5 amu (corresponding to 75% NO^+, 25% O_2^+), the total ion-neutral collision frequency is related to the total neutral density by

$$\nu_{in} = K \cdot N,$$

where $K = \frac{2.59 \times 10^{-11}}{30.5} \left[\%(N_2) \cdot 5.07 + \%(O_2) \cdot 4.98 + \%(O) \cdot 2.88 \right]$

[*Lathuillere et al.*, 1983]. We have used the MSIS-86 model [*Hedin*, 1987] to estimate the relative populations of the three neutral species and thus the constant K.

3.4 Range smearing

For a logarithmically varying quantity such as v_{in}, the range resolutions of the Chatanika multipulse modes can potentially introduce large errors due to range smearing. The magnitude of the errors are difficult to quantify and may be a function of altitude.

Range smearing arises because the ACF is formed using contributions from a volume of atmosphere of finite height. For a single-pulse of length τ, there are contributions to the ACF from an altitude range of τ·c, where c is the speed of light. Actually however, the ACFs are formed from multiple pulses, and a weighting scheme is applied to the lagged products forming the ACF, yielding an effective range resolution better than τ·c. As mentioned above, the 160-μs and 60-μs multipulse modes have range resolutions of 24- and 9-km respectively.

The greater the variation of the parameter to be determined over the range, the worse the range smearing can be. Temperature and winds typically change linearly over the altitude ranges in question, but the ion-neutral collision frequency is proportional to the neutral density and falls off exponentially. In the E-region, the scale height for variation of v_{in} is approximately 8-km. Thus the 60-μs multipulse mode at Chatanika has a range resolution of the order of a neutral scale height while the 160-μs mode is approximately 3-times the neutral scale height.

A simple way to attempt to quantify this problem is to assume that the radar is physically integrating the density over an altitude increment R. A triangular weighting scheme is applied to the integration, and the density is assumed to vary with a constant scale height, H. This is shown schematically in figure 3.1. Symbolically, the problem is

$$n'(z_0) = \int_{z_0 - R/2}^{z_0 + R/2} n(z)w(z)dz$$

where $n'(z_0)$ is the estimated density at z_0. It can be shown that the estimated density is given by

$$n'(z_0) = n(z_0)\left\{\left(\frac{H}{R/2}\right)^2\left[\exp\left(\frac{R/2}{H}\right) + \exp\left(-\frac{R/2}{H}\right) - 2\right]\right\}$$

67

where $n(z_0)$ is the actual density at z_0. Interestingly, it is the ratio of the scale height to half the range resolution that is the critical parameter. This simple model predicts that for a neutral scale height of 8-km, the 60-μs and 160-μs pulse modes will overestimate the density by 3% and 20% respectively, independent of altitude.

Of course, this model neglects the fact that the ACF is the quantity that is being integrated over the height range by the radar, not the density. Also the electron density is varying with height in the E-region, and the scattered signal strength is proportional to the electron density. To some extent this dependence on electron density should mitigate the range smearing effect of the exponentially decreasing neutral density, since in general the electron density increases through the altitude range of interest (90-110 km). Thus in general, the return signal from the portion of the range with greatest v_{in} (and lower n_e) will be smaller than the return from the portion of the range with lower v_{in} (and higher n_e).

Lathuillere et al. [1983] performed a more realistic simulation to test the error introduced by range smearing while using the 60-μs multipulse mode (9-km resolution). ACFs were computed with a 1.5-km altitude resolution using different density and temperature profiles. Then theoretical mean ACFs were computed in the same way as in the radar autocorrelator and analyzed to obtain "mean" collision frequencies and temperatures. The temperatures obtained from the simulation showed very little range smearing. The error in the collision frequencies was less than 15% between 90- to 105-km. Above 105-km, the fits to the simulated ACF appeared to be increasingly overestimated relative to the model values. The magnitude of the range smearing changed with altitude, increasing above 105-km. Interestingly, changing the electron density profile from one constant with height to one typical for the E-region appeared to not affect the "mean" temperatures and collision frequencies in this simulation.

Obviously, the better the range resolution, the less of a problem range smearing will be. An EISCAT multipulse mode has an effective resolution of less than 1-km [Huuskonen et al., 1986] and has been used to make high resolution measurements of E-region collision frequencies.

Yet Reese et al. [1990] obtained an average neutral density profile using the 160-µs multipulse at Sondrestrom that showed good agreement with MSIS-86 [Hedin, 1986]. between 90- to 105-km.

One way to experimentally test the magnitude of range smearing introduced by the different multipulse modes is to make measurements with both modes within a relatively short time and compare the results. Within the data being examined here, there are two cases where 60-µs and 160-µs multipulse measurements were made within 30 days of each other. In one of these cases, a 160-µs measurement is actually bracketed by 60-µs measurements on each side. Average vertical profiles of v_{in} have been computed for these cases and displayed in Figures 3.2a and 3.2b. In both cases, the triangles indicated the 160-µs multipulse measurements and the squares indicate the 60-µs measurements. The measurements made with the two multipulse modes are indistinguishable within their respective uncertainties; one multipulse mode cannot be said to range smear more than the other based on this comparison.

It is clear that further study will be needed to quantify the magnitude of the range smearing problem when the range resolution is of the order of, or greater than the neutral scale height. In the results that follow, both multipulse modes are used to examine long term trends in the neutral scale heights. However, only data derived from the 60-µs multipulse is used in the study of average profiles and tides as a function of season.

3.5 Results and Discussion

3.5.1 Solar cycle effects in the E-region neutral scale height

Figure 3.3a displays average neutral scale height as a function of date between 1977 and 1982. The scale heights represent average v_{in} profiles between the altitudes of 89- to 110-km for each day. The scale heights are determined from a weighted least squares fit to the profiles, weighted by the uncertainty of the mean at each altitude. The two symbol types indicate the radar mode in use on that day. It is interesting to note that there is no obvious discontinuity between the scale heights derived using the two multipulse modes which may have arisen as a result of range smearing as discussed in the previous section.

Figure 3.3b is a trace of the 81-day averaged F10.7 solar index for the same period. It appears that there is a trend in the lower thermospheric neutral scale height which is connected to the solar cycle variation. The scale height is observed to increase from an average of approximately 7-km in 1977-78 to approximately 12 km in 1981-82. A neutral scale height change from 7-km to 12-km corresponds to a change in temperature from ~225°K to ~386°K at 100-km assuming no change in composition. The neutral scale height at 100-km calculated using the neutral temperature and mean molecular weight from MSIS-86 showed virtually no solar cycle variation, staying almost constant at a value of approximately 6-km.

3.5.2 Average vertical profiles of neutral density: Seasonal effects

All data discussed from here on includes only 60-μs multipulse data from 1979 until 1982. The experiments are divided by season, and average vertical profiles and tidal analyses are generated for each season. It was originally our intent to average a large number of days for each seasonal case and compare the vertical profiles and tidal modes as a function of season. But the presence of a solar cycle variation over the duration of the data set may mask any seasonal variation. In addition, the experiments to be averaged together must have the same range gate spacing. For example, averaging together a day with data sampled at 90, 100 and 110-km with a day sampled at 95, 105, and 115 km will be statistically meaningless.

With these constraints in mind, four sets of data were formed for the purpose of examining average seasonal effects. There is a summer case consisting of four experiments from the summer of 1980, an autumn case consisting of approximately 5-days from the fall of 1980, and two winter cases consisting of four experiments from the winters of 1980-81 and 1981-82 respectively. The individual days included in each of the seasonal cases are shown in Table 3.2.

Figures 3.4 - 3.7 display average vertical profiles of neutral density corresponding to the summer '80, autumn '80, winter '80-'81, and winter '81-'82 cases respectively. The error bars indicate the uncertainty of the mean computed by

$$\sigma_\mu^2 = \frac{1}{\sum \left(1 / \sigma_i^2 \right)}$$

where σ_i are derived from the individual error estimates from the fit for the ion-neutral collision frequencies. Also on the figure are densities from the MSIS-86 model (dotted line. The solid line is a weighted least squares fit to the data assuming a constant scale height. The form

$$n(z) = n(z_0)exp\left\{-\frac{(z-z_0)}{H_s}\right\}$$

was used in this fit, where the reference altitude, z_0, is 100 km and $n(z_0)$ and H_s are determined by the least squares fit. The average density at each altitude is weighted by the uncertainty of the mean at that altitude.

The average vertical profiles for all four cases have a greater scale height than the corresponding profiles from MSIS-86. As mentioned above, the neutral temperatures at 100-km from MSIS-86 are fairly constant for differing F10.7 inputs, and the neutral scale height at 100 km from MSIS-86 changes very little over the solar cycle. However as observed above, it appears that there is a solar cycle variation observed in the scale height fit to the lower thermospheric neutral densities at Chatanika. Since 1980-81 is close to solar maximum, it is not surprising that the four observed profiles all have a greater scale height than predicted MSIS-86.

There is also variation among the three seasonal cases from 1980. The scale height determined from the fit to the summer '80 data is 7.4 km, while for the autumn '80 and winter '80-'81 cases the scale height is 9.5 km. There is a large increase between the winter '80-'81 case and the winter '81-'82 case, 9.5 km to 16.4 km. The overall trend in these four scale heights is consistent with the trend observed in the scale heights as a function of solar cycle. The three profiles from 1980 and 1981 all display a roughly constant scale height with altitude. The winter '81-'82 profile deviates from a constant scale height profile at 90-km; altitudes above 90-km have a nearly constant scale height, but the average density at 90-km appears too low. It is possible that the winter conditions and the low altitude may have combined to create a situation with insufficient ionization to accurately derive the ion-neutral collision frequency. Alternatively, the profile in this case may be poorly represented by a constant scale height. In either case, if the 90-km average

density is omitted from the fit, a neutral scale height of 9.1 km results, which is consistent with the observations of the previous winter.

Other investigators have reported neutral scale heights from fits to radar-derived neutral density and v_{in} profiles. Reese et al. [1990] fit average neutral densities between 92- to 109-km with a constant scale height of 5.5-km at Sondrestrom during autumn 1987, slightly past solar minimum conditions. Kirkwood also reported neutral density profiles during solar minimum conditions (1984 - 1985) at EISCAT. Very little seasonal variation was observed in the average v_{in} profiles. In winter the collision frequency scale height was about 6-km between 92- to 105-km altitude. In the summer, the scale height was observed to increase steadily from about 5-km at 92-km altitude to about 8-km at 105-km altitude. Lathuillere et al. [1983] reported neutral scale heights between 6- and 8-km from March 1978 at Chatanika using the 60-μs multipulse (also solar minimum). These results are consistent with the scale heights displayed in Figure 3.3a which were obtained using the 160-μs multipulse. Kofman et al. [1986] observed neutral scale heights that varied between 5- to 7-km during the period from 1983 to 1985. This period is post-solar maximum, and also seems to fit in with the longterm solar cycle oscillation of the lower thermospheric neutral scale height.

3.5.3 Tides in the neutral density: seasonal dependence

The lower thermosphere is strongly affected by a number of dynamic influences. Solar absorption by ozone in the mesosphere excites tides below thermospheric altitudes which can propagate upwards. These tides, which are relatively unimportant at high latitude, are predominantly semidiurnal in nature. Gravity waves can also propagate into the thermosphere from below. Waves propagating upwards amplify with altitude until molecular viscosity, thermal conduction, and ion drag begin to damp their growth above about 150 km. Most propagating diurnal waves tend to destructively interfere due to their smaller vertical wavelength, thus diurnal tides are essentially limited to their region of excitation [Fesen et al., 1986]. An exception is the propagating (1,1) mode which is quite large at the lowest levels of the thermosphere but is dissipated by about 105 km.

The four seasonal case studies described above have been analyzed to characterize the tidal oscillations in the neutral density between 89- to 110-km We have performed a linear regression fit to a sinusoidally varying function at each altitude. Specifically, the data is fit to

$$f(t) = a_0 + a_1 \cos(\omega_1 t) + b_1 \sin(\omega_1 t) + a_2 \cos(\omega_2 t) + b_2 \sin(\omega_2 t)$$

where $\omega_1 = \frac{2\pi}{1\ \text{day}}$ and $\omega_2 = \frac{2 \cdot 2\pi}{1\ \text{day}}$. The linear regression is performed by the routine REGRESS [Bevington, 1969] using instrumental uncertainties to weight the fits. From the coefficients, we derive amplitudes and phases (local times of maximum) for the diurnal and semidiurnal oscillations.

Figures 3.8 - 3.11 are summaries of the amplitudes and phases for the diurnal and semidiurnal oscillations observed for each of the seasonal cases. On the left is the amplitude of the diurnal and semidiurnal oscillations at each altitude. Also displayed as X's are the ratio of each amplitude to the constant term determined from the least squares fit ($100 \cdot a_i/a_0$). On the right is the local time of maximum for each oscillation and altitude. Uncertainties in the coefficients have been determined using error propagation techniques from the uncertainties in the coefficients obtained from the weighted fit. Some interesting observations can be made from these plots.

Amplitudes   The diurnal oscillations present in the neutral density are of the same order of magnitude as the semidiurnal components for all the seasons. The amplitudes of the diurnal and semidiurnal tides at Sondrestrom during LTCS-1 were also approximately equivalent [Reese et al., 1990]. This is somehat unexpected because the semidiurnal tide is thought to be the dominant tidal oscillation at these altitudes. In equatorial regions below 180 km, the amplitude of the semidiurnal tide exceeds that of the diurnal tide in the neutral density [Sharp et al., 1978].

The amplitudes of both the diurnal and semidiurnal components decrease with height as a general rule. However in the two winter cases, the amplitudes stay roughly constant with height. The amplitudes as a percentage of the mean display a somewhat more complicated behavior. In both winter cases, the percentage amplitude of the diurnal component increases with altitude, while the semidiurnal component appears to increase to a maximum of approximately 10% near 100 km. The percentage amplitudes of both oscillations in the summer case are relatively small, generally

73

less than 10%, with the semidiurnal case decreasing with altitude. The autumn case has the largest amplitudes of all the cases for both the diurnal and semidiurnal oscillations. Reese et al. [1990] also observed large amplitude oscillations in the autumn at Sondrestrom during LTCS-1. The winter '81-'82 case also has relatively large amplitudes. That case includes a period from late October and one from mid-November, both winter by our definition, but may still reflect autumn characteristics. Kirkwood [1986] calculated semidiurnal amplitudes (as percentages of the mean) and phases for four periods in 1985. The November and January cases (both 'winter' in our scheme) have amplitudes less than 10%, which agrees with our observations. Their August case has semidiurnal amplitudes less than 10% which decrease with altitude, which also agrees with our summer '80 case.

Phases   The phases in these seasonal cases display quite a bit of variability. The semidiurnal phases in both winter cases display roughly the same behavior: the phase changes little with height up to ~105 km then shifts towards earlier local times by 6 hours or more above 105 km. The semidiurnal phases in both winter cases of Kirkwood [1986] basically decrease with height between 90-110 km. The diurnal phases of the two winter cases are dissimilar. The winter '81-'82 diurnal phases remain nearly constant with height, while the winter '80-'81 diurnal phases tilt to earlier local times as altitude increases.

For the summer '80 case, the phase of the semidiurnal oscillation decreases with altitude indicative of a vertically propagating oscillation with a vertical wavelength of ~20 km. The semidiurnal phase of Kirkwood's [1986] August case also decreases with altitude, rapidly between 90- to 98-km then much more slowly above 98-km. Due to the large uncertainty of the diurnal phases as a function of height, no clear altitude dependence of the diurnal phase is evident.

For the autumn '80 case, the diurnal phase stays nearly constant with height up to 100 km, where it jumps by nearly 12 hours. This same feature was observed by Reese et al. [1990] in the LTCS-1 neutral densities except the jump took place slightly lower, between 92-98 km. The semidiurnal phase also remains constant up to 100 km, then decreases with altitude. The

semidiurnal phase from LTCS-1 decreased with height indicative of an upwardly propagating wave [Reese et al., 1990] with a vertical wavelength of ~20 km.

3.6 Conclusions

We have analyzed the ion-neutral collision frequencies from a large data set from the Chatanika, Alaska incoherent scatter radar facility consisting of more than 50 days of data. Our procedures for removing periods of E-region heating from the data was discussed as well as the technique for deriving neutral densities from the radar derived collision frequencies.

Range smearing can introduce errors into radar measurements especially when determining an exponentially changing parameter such as v_{in}. However, examination of v_{in} profiles derived using the two different Chatanika multipulse modes (9- and 24-km resolution) revealed no obvious range smearing effects between the two modes. It would be interesting to design a similar experiment comparing v_{in} profiles derived from the 9-km resolution multipulse and a much higher resolution multipulse mode.

The 50 radar experiments examined in this study encompass a period from 1977 - 1982. When average v_{in} profiles between 89 - 110 km are fit for a constant scale height, these scale heights appear to correlate very well with the large scale solar cycle variation displayed in the F10.7 solar flux. The scale heights vary on average from ~6-km in 1977 to over 12-km in 1982. The MSIS-86 model does not include this dependence, and instead generates neutral scale heights of approximately 6-km at 100-km which are very nearly constant throughout the solar cycle.

Four seasonal cases were examined for average vertical profiles and tidal oscillations of the neutral density. All four cases had scale heights greater than the scale heights from MSIS-86. The three vertical profiles from 1980-81 all had scale heights which were almost constant with altitude between 89 - 110 km. The constant scale height fit to the summer '80 case was 7.4 km, while the autumn '80 and winter '80-'81 scale heights were both 9.5 km. The constant scale height fit to the winter '81-'82 average profile was 16.4 km, but the average density at the lowest altitude appeared suspect, possibly due to insufficient ionization. With this altitude removed, the scale height fit to the data was 9.1 km. Kirkwood [1986] observed that vertical profiles from the entire year could

75

be modelled by two cases: a case representing the summer and a case representing the rest of the year. Our results support this conclusion, although all our scale heights are higher than those of Kirkwood [1986], probably due to solar cycle effects as noted above.

The tidal oscillations present in the neutral density display considerable complexity. The amplitudes of the diurnal and semidiurnal oscillations present in the neutral density are of the same order of magnitude for all the seasons. The largest amplitude oscillations were observed in the autumn '80 case. Reese et al. [1990] also observed large oscillations in the autumn during LTCS-1 at Sondrestrom. However in that study of four contiguous days of measurements, the tidal amplitudes exceeded those found here, where noncontiguous measurements were averaged together. Since tidal amplitudes tend to be somewhat consistent over time intervals of several days, the smaller amplitudes determined here are not unexpected. The percentage amplitudes of the semidiurnal modes for the two winter and summer cases agreed with the observations of Kirkwood [1986] at EISCAT. It is difficult to make further conclusions concerning tidal oscillations present in the neutral density due to the lack of other observations and model results suitable for comparison. However, this study should provide a starting point for further examinations of tidal oscillations in the polar lower thermospheric neutral density.

Date	Season	Multipulse type	Ap	Date	Season	Multipulse type	Ap
11 Aug 76	Sum	160-μs	5	19 Dec 79	Win	60-μs	6
22 Dec 76	Win	160-μs	8	16 Jan 80	Win	60-μs	9
15-16 Feb 77	Win	160-μs	8,6	13 Feb 80	Win	60-μs	2
15-16 Mar 77	Spr	160-μs	5,6	19-20 Mar 80	Spr	160-μs	10,4
19-20 Apr 77	Spr	160-μs	48,28	16 Apr 80	Spr	60-μs	12
18-19 May 77	Sum	160-μs	11,5	14 May 80	Sum	60-μs	17
16 Jun 77	Sum	160-μs	10	11 Jun 80	Sum	60-μs	59
23 Nov 77	Win	160-μs	2	9 Jul 80	Sum	60-μs	8
18 Jan 78	Win	160-μs	12	13-14 Aug 80	Sum	60-μs	6,6
8 Feb 78	Win	160-μs	10	10 Sep 80	Aut	60-μs	4
8 Mar 78	Spr	160-μs	20	8 Oct 80	Aut	60-μs	12
12 Apr 78	Spr	160-μs	29	10-12 Oct 80	Aut	60-μs	22,40,11
10 May 78	Sum	160-μs	10	12 Nov 80	Win	60-μs	12
7 Jun 78	Sum	160-μs	11	10-11 Dec 80	Win	60-μs	10,16
12-13 Jul 78	Sum	160-μs	4,20	14 Jan 81	Win	60-μs	6
1-2 Aug 78	Sum	160-μs	4,4	4 Feb 81	Win	60-μs	9
6 Sep 78	Aut	160-μs	14	4 Mar 81	Spr	160-μs	12
18 Oct 78	Aut	160-μs	32	1 Apr 81	Spr	60-μs	23
13-14 Dec 78	Win	160-μs	7,28	13 May 81	Sum	60-μs	10
14 Feb 79	Win	160-μs	2	14-16 Jul 81	Sum	60-μs	7,4,8
21 Mar 79	Spr	160-μs	4	28-29 Oct 81	Win	60-μs	19,12
18 Apr 79	Spr	160-μs	6	18 Nov 81	Win	60-μs	26
20 Jun 79	Sum	160-μs	8	15-17 Dec 81	Win	60-μs	6,4,7
17-18 Oct 79	Aut	60-μs	4,3	19-20 Jan 82	Win	60-μs	3,6
21 Nov 79	Win	160-μs	6	16-17 Feb 82	Win	60-μs	6,30

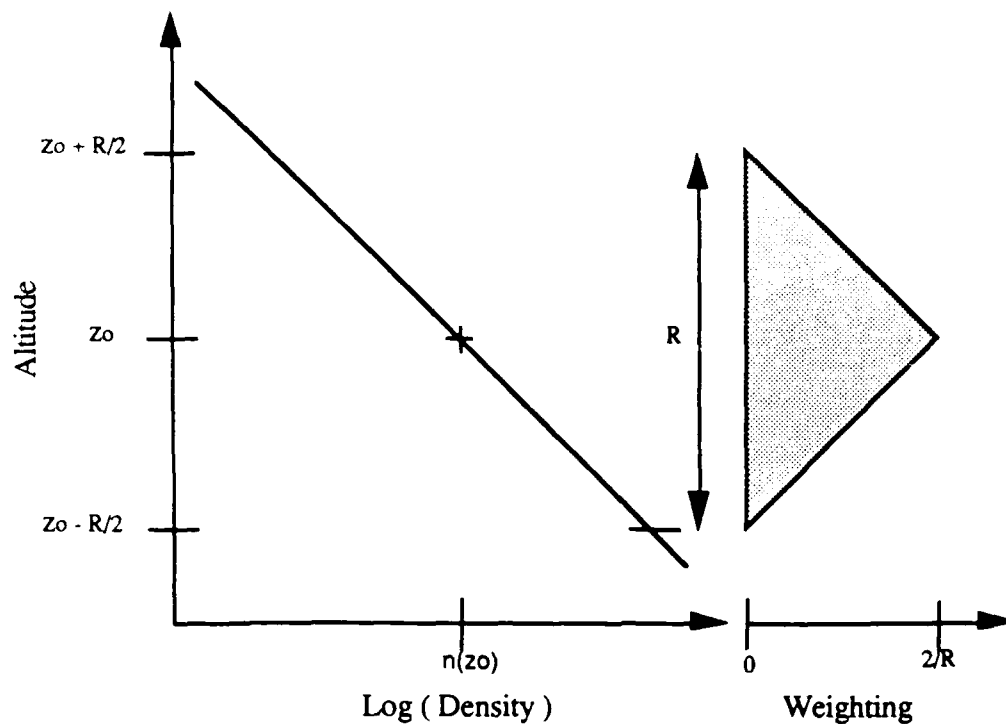Table 3.1   Summary of radar experiments from Chatanika used in this study.

Figure 3.1 Simple illustration of range smearing. The density falls off exponentially as shown on the left. The radar attempts to determine $n(z_0)$. But due to the radar pulse length, the density at z_0 is estimated by integrating the density over an altitude range of length R. A triangular weighting is applied over the interval as shown on the right.
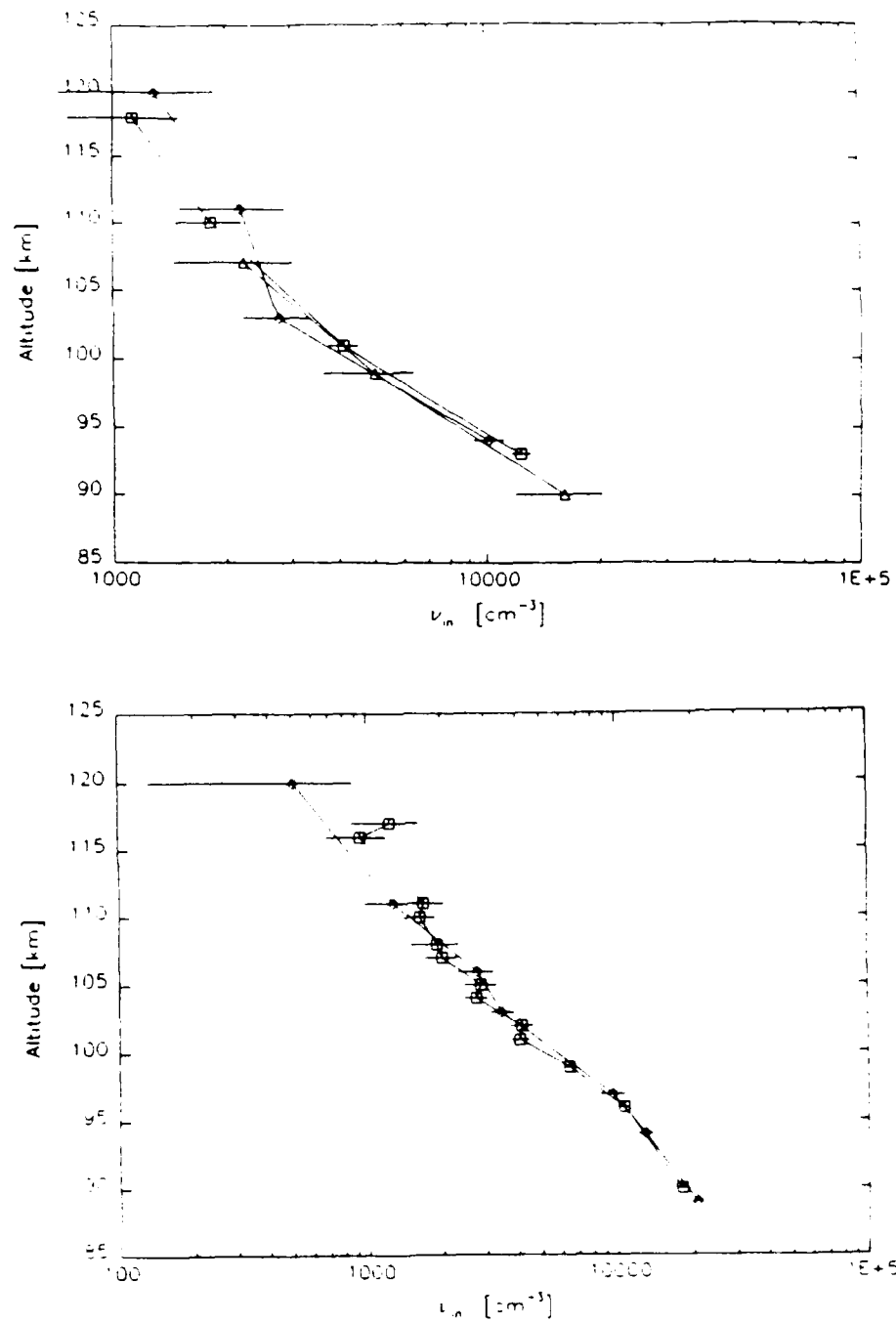
Figure 3.2   Average ion-neutral collision frequency as function of altitude for days with different multipulse modes in fairly close proximity. The profiles are almost identical within the uncertainties; no obvious range smearing effect is apparent between the two pulse modes in these profiles. Figure 3.2a   17-18 Oct 1979 (square, 60-ms), 21 Nov 1979 (diamond, 160-ms), and 19 Dec 1979 (triangle, 60-ms)   Figure 3.2b   19-20 Mar 1980 (diamond, 160-μs) and 16 Apr 1980 (square, 60-μs)
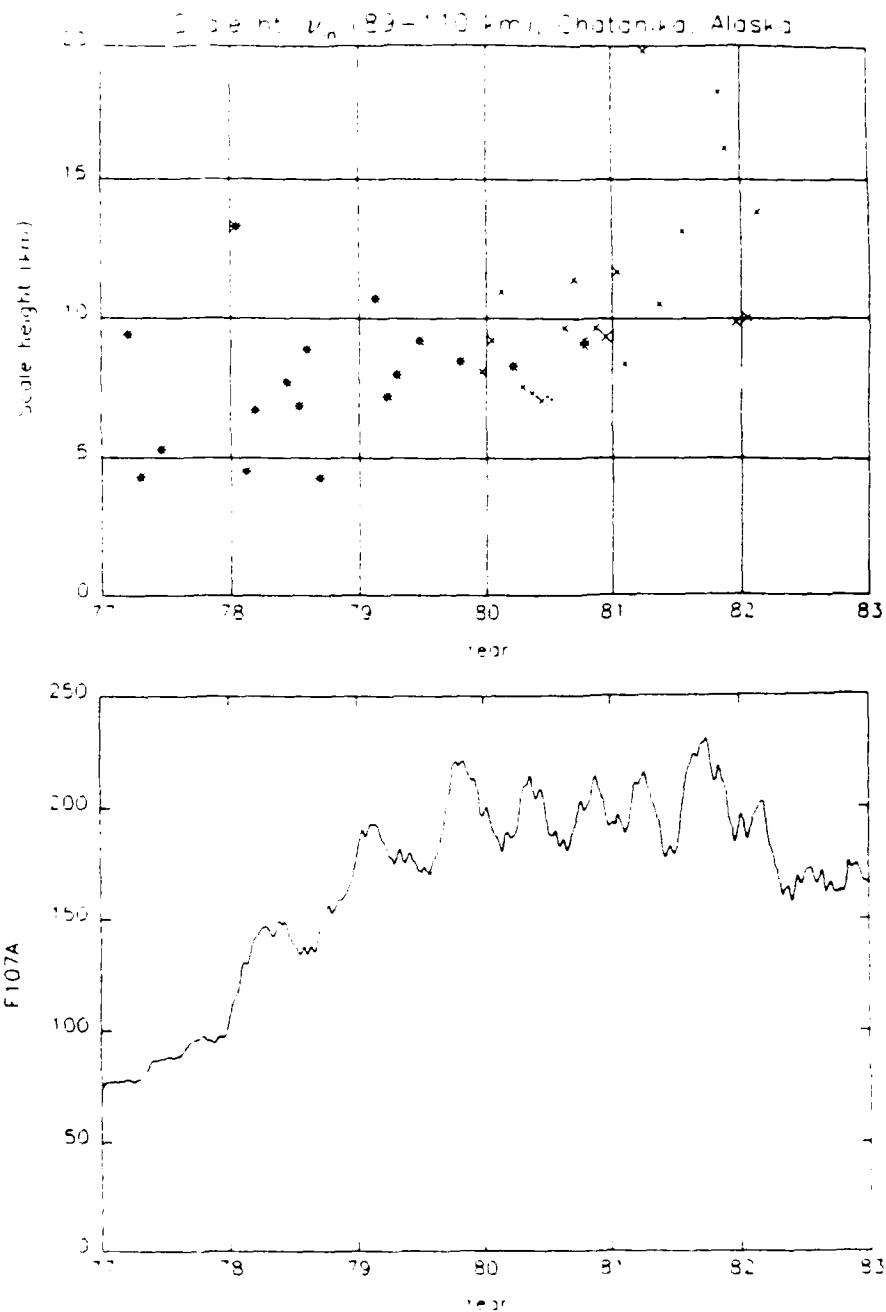
Figure 3.3a   Scale heights resulting from fits of average $v_{i n}$ profiles between the altitudes of 90- to 105-km at Chatanika. The (*) correspond to the 160-μs multipulse mode while the (X) correspond to the 60-μs multipulse mode.   Figure 3.3b   81-day average F10.7 solar flux for the same years as in Figure 3.2b. Solar maximum was in 1980-81. Note the correlation between the neutral scale heights and the large scale variation of the F10.7 solar flux.

80

CASE	DAYS
Summer 1980	14 May 1980
	11 Jun 1980
	9 Jul 1980
	13-14 Aug 1980
Autumn 1980	10 Sep 1980
	8 Oct 1980
	10-12 Oct 1980
Winter 1980-81	12 Nov 1980
	10-11 Dec 1980
	14 Jan 1981
	4 Feb 1981
Winter 1981-82	28-29 Oct 1981
	18 Nov 1981
	15-17 Dec 1981
	19-20 Jan 1982

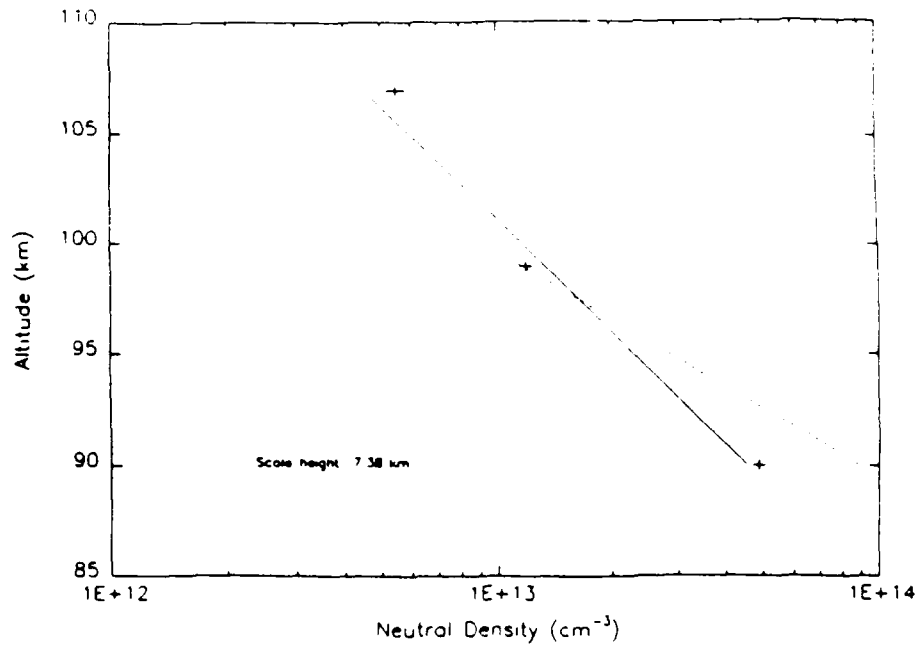Table 3.2 Summary of the days used in each of the seasonal cases examined in this study.

Figure 3.4   Average neutral density profile for the summer '80 case. The crosses with the error bars are the experimental averages. The dotted line is a neutral density profile determined from MSIS-86 for identical conditions. The solid line is a fit to the experimental data assuming a constant scale height. The constant scale height determined by the fit is 7.4 km.
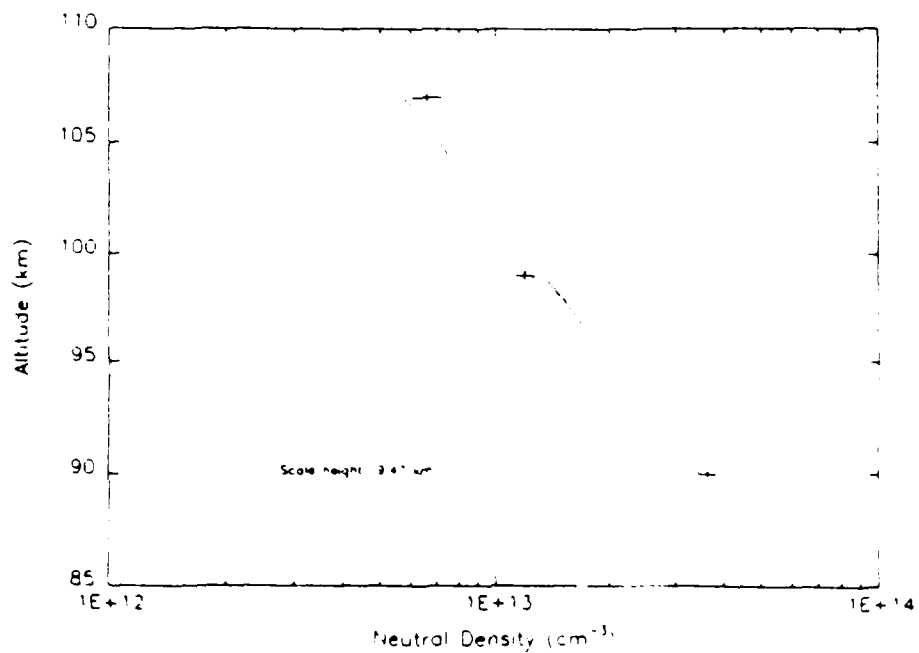

Figure 3.5   Same as Figure 3.4 for the autumn '80 case. The constant scale height determined from the fit to the data is 9.5 km.
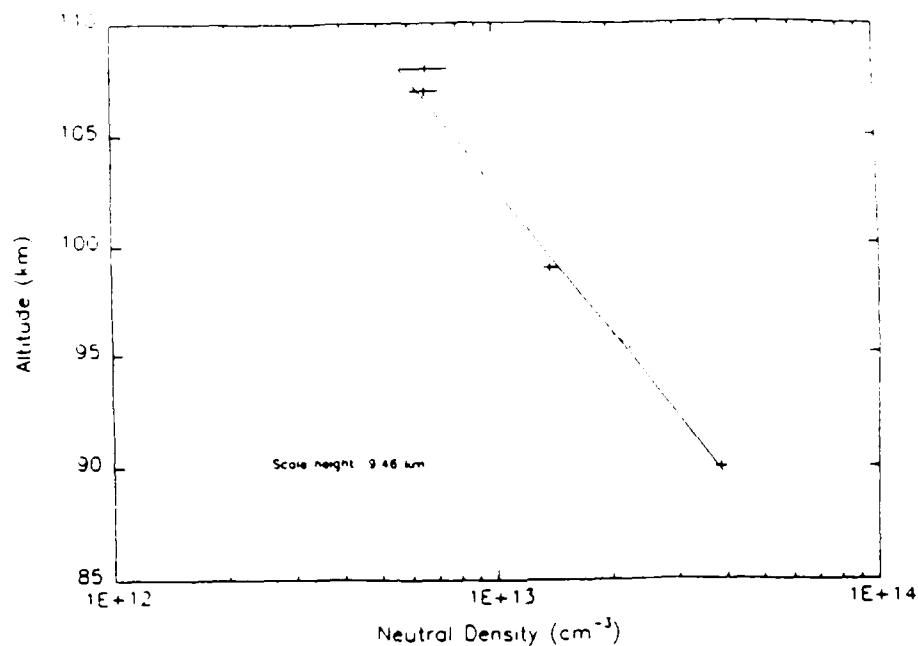
Figure 3.6   Same as Figure 3.4 for the winter '80-'81 case. The constant scale height determined from the fit to the data is 9.5 km.
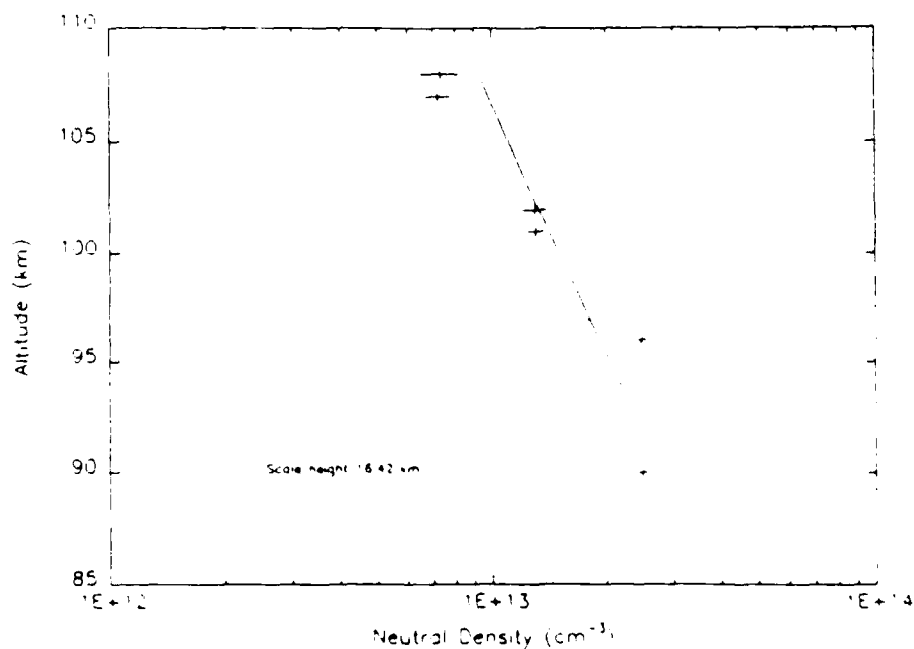

Figure 3.7   Same as Figure 3.4 for the winter '81-'82 case. The constant scale height determined from the fit to the data is 16.4 km. The lowest data point may be unreliable due to low ionization. The scale height fit to the data neglecting the lowest altitude is 9.1 km
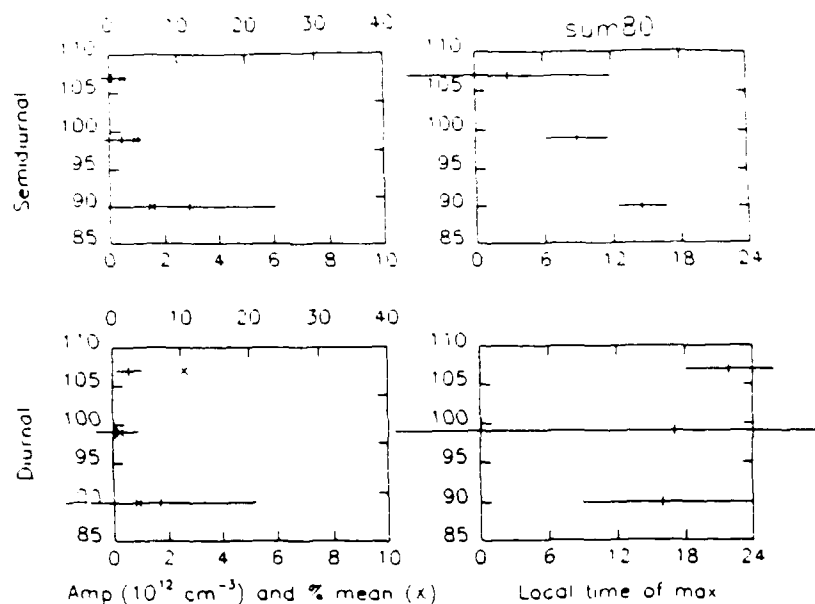
83

Figure 3.8 Summary of the tidal fit to the data for the summer '80 case. The amplitude and phase of the semidiurnal oscillation is shown in the top two panels, while the same for the diurnal oscillation is in the bottom two panels. On the left in each case is the amplitude of the oscillations. The amplitudes (shown with error bars) correspond to the scale on the bottom of each figure on the left. Also displayed on the left are the amplitudes as a percentage of their mean. These are plotted as X's and correspond to the scale at the top of each figure on the left. On the right are the phases of the oscillations, presented as the local time of maximum.
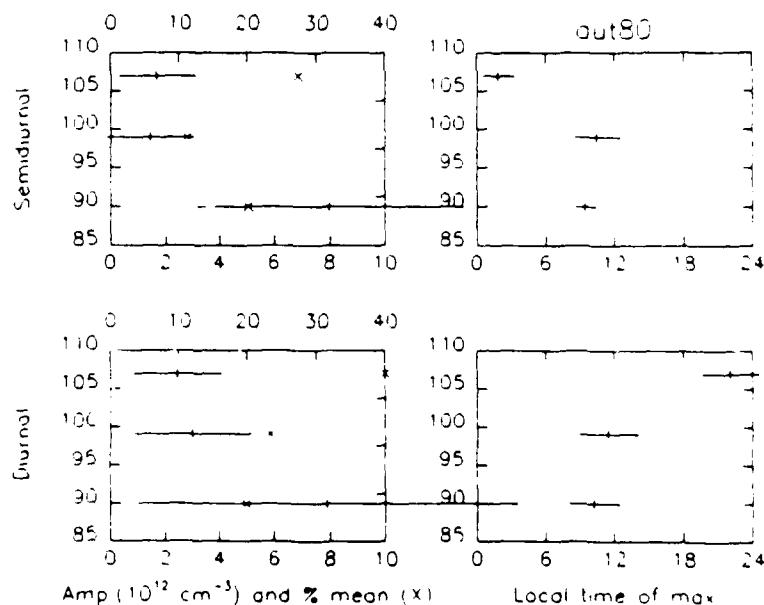

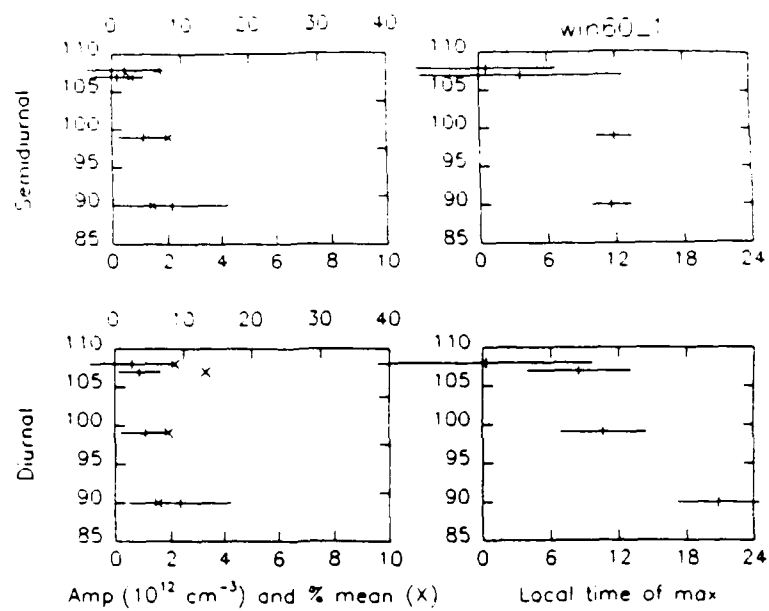
Figure 3.9 Same as Figure 3.8 for the autumn '80 case.

84

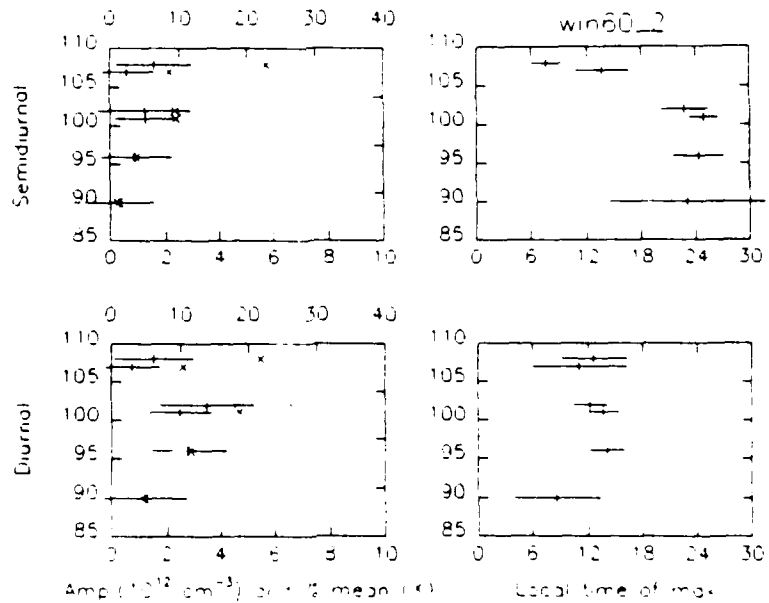Figure 3.10   Same as Figure 3.8 for the winter '80-'81 case.

Figure 3.11   Same as Figure 3.8 for the winter '81-'82 case.

Chapter 4   Conclusions and Remarks

The objective of this thesis was to investigate average vertical profiles and the dynamic behavior of the neutral density in the polar lower thermosphere utilizing the incoherent scatter radar technique. To accomplish this objective, I developed the techniques and software necessary to process incoherent scatter radar data received on magnetic tapes in a standard output format. The radar data which was analyzed in this thesis included one 6-day experiment from Sondrestrom, Greenland conducted during the Lower Thermospheric Coupling Study (LTCS-1), and more than 50 days of data from Chatanika, Alaska. The ultimate products of the data processing are average vertical profiles of neutral density and analyses of the tidal oscillations present in the neutral density. I have accomplished my objective for the Sondrestrom and Chatanika data mentioned above, and my techniques can now be easily applied to any set of radar data containing ion-neutral collision frequencies for which one is interested in the lower thermospheric neutral densities.

The ion-neutral collision frequency is the radar-derived parameter from which one can derive neutral density in the lower thermosphere. In Section 1.3, I presented enough incoherent scatter theory to illustrate how so many parameters of the plasma and neutral gas can be derived from the backscattered signal of the radar. The backscattered signal of the radar is received as a power spectrum or an autocorrelation function (ACF). In Section 1.4, the locations and operating modes of the incoherent scatter radar facilities were presented. Then the data processing system of the Chatanika/Sondrestrom radar was discussed. The ion-neutral collision frequency is fit from the ACF under the assumption that the ion and electron temperatures are equal. But in the polar lower thermosphere, there are processes that can cause thermal disequilibrium among the ions and electrons. In Section 1.5, these E-region heating mechanisms were described. The ion-neutral collision frequencies derived during periods of heating should not be used, and in Section 1.5, I described my technique for removing periods of E-region heating from the data.

86

The next step in my data processing was to convert ion-neutral collision frequencies to neutral densities. The dominant interaction between ions and neutrals in the lower thermosphere is an induced dipole interaction. In Section 1.6, I presented the theory which leads the formula which I have used to convert the collision frequencies to neutral density. The final step in the analysis was to compute average vertical profiles of the neutral density and to examine the tidal oscillations present in the neutral density. In Section 1.7, I discussed the mean structure of the lower thermospheric neutral density. Then I presented the classical tidal derivation to establish that tidal oscillations should be present in the neutral density. Finally, I described the important thermospheric tidal modes one expects to observe in the polar lower thermospheric neutral density.

This introduction was designed to provide background material to the information contained in Chapters 2 and 3. Both chapters 2 and 3 are papers that have been submitted for publication. They were designed to be able to stand alone, and were limited in the amount of background material that could be presented in them. Chapter 2 was a study of lower thermospheric neutral densities from Sondrestrom during the LTCS-1. This was the first ever examination of neutral densities from Sondrestrom, and only the second analysis of tidal oscillations present in the neutral density. Chapter 3 was a study of seasonal and solar cycle variations in the lower thermospheric neutral density from Chatanika. The major results of these two studies are summarized below.

1) The data processing software developed in this study can efficiently process radar data from magnetic tape to plots of average neutral density profiles and tidal summaries in an almost-automated fashion. Only the identification of particle precipitation events and anomalous heating intervals require 'hands on' interface.

2) Range smearing can introduce error into radar derived parameters, especially an exponentially changing parameter like the ion-neutral collision frequency. However, collision frequency profiles determined by different multipulse modes within 30 days of each other are virtually indistinguishable within the uncertainties of the measurements. This seems to indicate that when determining collision frequencies, range smearing by the 160-μs multipulse (24-km

resolution) is not much worse than range smearing by the 60-μs multipulse (9-km resolution) and hopefully is fairly insignificant. The range smearing effect may be lessened in the E-region since the electron density is typically increasing with altitude (with proportional gain in signal strength) as the neutral density decreases. Further study of range smearing, both experimental and and theoretical, is needed to accurately quantify this possible source of error.

3) Neutral scale heights fit to average v_{in} profiles between 89-110 km at Chatanika showed a very good correlation with the long term variation in F10.7 solar flux index, which indicates a strong solar cycle dependence of lower thermospheric neutral scale height on solar cycle. Neutral scale heights determined from the MSIS-86 model at 100 km showed virtually no variation with solar cycle, remaining nearly constant at a value near 6-km. The neutral scale height at Chatanika on the other hand varied on average between ~7-km in 1977 to more than 12-km in 1982. This scale height change corresponds to a temperature change at 100 km of ~225°K to ~386°K assuming that the mean molecular weight remains constant. Clearly this is a significant finding. Other investigators have reported lower thermospheric neutral scale heights which reinforce the theory that the scale height is closely connected to solar cycle.

4) Four case studies were examined at Chatanika for seasonal effects on average profiles and tidal oscillations. The four cases were summer '80, autumn '80, winter '80-'81, and winter '81-'82. Neutral scale heights fit to the average neutral density profiles for each case were 7.4 km, 9.5 km, 9.5 km, and 16.4 km respectively. The three profiles from 1980 and 1981 all displayed a roughly constant scale height with altitude. The winter '81-'82 profile deviates from a constant scale height profile at 90-km; altitudes above 90-km have a nearly constant scale height, but the average density at 90-km appears too low. It is possible that the winter conditions and the low altitude may have combined to create a situation with insufficient ionization to accurately derive the ion-neutral collision frequency at 90-km. Alternatively, the profile in this case may be poorly represented by a constant scale height. If the 90-km average density is omitted from the fit, a neutral scale height of 9.1 km results. Kirkwood [1986] observed that vertical profiles from the entire year could be modelled by two cases: a case representing the summer and a case

representing the rest of the year. Our results support this conclusion, although all our scale heights are higher than those of Kirkwood [1986], probably due to solar cycle effects as noted above.

5) The tidal analyses of the Chatanika and Sondrestrom neutral densities showed considerable complexity, however several observations can be made. The diurnal oscillations present in the neutral density were of the same order of magnitude as the semidiurnal components. This was somehat unexpected because the semidiurnal tide is thought to be the dominant tidal oscillation at these altitudes.

The amplitudes of both the diurnal and semidiurnal oscillations were very large in the autumn. This was observed in both the autumn '80 case at Chatanika and the LTCS-1 (autumn '87) period at Sondrestrom. The phases observed during autumn at Sondrestrom and Chatanika were also similar. The phase of the diurnal oscillation at Chatanika stayed nearly constant with height up to 100 km, where it jumped by nearly 12 hours. This same feature was observed at Sondrestrom except the jump took place slightly lower, between 92-98 km. At Chatanika, the semidiurnal phase also remained constant up to 100 km, then decreased with altitude. The semidiurnal phase from LTCS-1 decreased with height indicative of an upwardly propagating wave with a vertical wavelength of approximately 15 km.

In both winter cases, the amplitudes as a percentage of the mean of the diurnal components increased with altitude, while the semidiurnal components appeared to increase to a maximum of approximately 10% near 100 km. The percentage amplitudes of both oscillations in the summer case were relatively small, generally less than 10%, with the semidiurnal case decreasing with altitude. Winter semidiurnal oscillations from Kirkwood [1986] agreed with the amplitudes of both the winter cases in this study. Kirkwood's August case had semidiurnal amplitudes less than 10% that decreased with altitude, which also agreed with our summer '80 case.

The remaining phases in these seasonal cases displayed quite a bit of variability. The semidiurnal phases in both winter cases display roughly the same behavior: The phases changed little with height up to ~105 km then shifted towards earlier local times by 6 hours or more above 105 km. The diurnal phases in the winter cases were dissimilar. For the summer '80 case, the

phase of the semidiurnal oscillation decreased with altitude indicative of a vertically propagating oscillation with a vertical wavelength of ~20 km.

It is difficult to make more detailed conclusions about the tidal oscillations observed in the neutral densities at Chatanika and Sondrestrom. But these results will provide a starting point with which future tidal analyses can be compared. Now that these techniques for analyzing neutral densities from incoherent scatter radar are in place, it is hoped that there will be further examinations of average vertical profiles and tidal oscillations of neutral density in the polar lower thermosphere.

Appendix A   Error analysis

This appendix contains the statistical formula and techniques that I have used in analyzing this data. This includes general formula for calculating means and uncertainties of the mean, propagation of errors analyses in going between v_{in} and the neutral density, and my technique for eliminating statistical outliers. Most formula are taken from Bevington [1969].

Associated with each ion-neutral collision frequency fit from each autocorrelation function in ACFIT is an error estimate for that parameter. The larger the error estimate, the less credible is that data point. For that reason I use a weighted mean whenever I calculate an average. The formula for the weighted mean is

$$\mu = \frac{\sum \frac{x_i}{\sigma_i^2}}{\sum \frac{1}{\sigma_i^2}}$$

where x_i are the data points and σ_i are the associated error estimates. The uncertainty of the mean is then given by

$$\sigma_i^2 = \frac{1}{\sum \frac{1}{\sigma_i^2}}$$

I have also examined two statistical quantities in addition to these. The first is the standard deviation which is given by

$$s^2 = \frac{1}{(N-1)} \sum (x_i - \bar{x})^2 \qquad \text{or equivalently} \qquad s^2 = \frac{N}{(N-1)} \left(\frac{\sum x_i^2}{N} - \bar{x}^2 \right)$$

where $\bar{x} = \sum x_i / N$ is the unweighted mean. The second is the estimated variance of the fit which is characteristic of both the spread of the data and the accuracy of the fit. When the function being fitted is the weighted mean, μ, then this is given by

$$s^2 = \frac{1}{(N-1)}\left(\frac{\sum \frac{1}{\sigma_i^2}(x_i - \mu)^2}{\frac{1}{N}\sum \frac{1}{\sigma_i^2}}\right) \qquad \text{or equivalently} \qquad s^2 = \frac{N}{(N-1)}\left(\frac{\sum \frac{x_i^2}{\sigma_i^2}}{\sum \frac{1}{\sigma_i^2}} - \mu^2\right)$$

In each of these two cases, the simpler form on the right is included because it is the form most computer programmable. Either of these estimates to the variance of the data can be used to estimate alternate uncertainties of the mean using the formula

$$\sigma_\mu^2 = \frac{s^2}{N}$$

The error estimates of the ion-neutral collision frequencies, σ_i, are provided with the collision frequencies by the ACFIT routine. But when the v_{in}'s are transformed into neutral densities, then what are the error estimates of the densities? To find out, one must use the technique of propagation of errors. If you recall from Section 1.6.2 above, the relationship that I derived relating v_{in} and N is

$$v_{IN} = K \cdot N$$

where $\qquad K = \frac{2.59 \times 10^{-11}}{30.5}\left(\%(N_2) \cdot 5.07 + \%(O_2) \cdot 4.98 + \%(O) \cdot 2.88\right)$

If K was indeed a constant introducing no error of its own, then the relationship between the error estimate in N and v_{in} would be quite simple, $\sigma(N) = (1/K)\sigma(v_{in})$. But there are uncertainties involved with the relative abundances of the neutral species given by the MSIS-86 model. I will assume that the MSIS-86 model will predict %( ) to within 15%. This means that $\sigma(\%( )) = 0.15 \cdot \%( )$. Let $A = 2.59 \times 10^{-11}/30.5$ and let $B = (\%(N_2)\ 5.07 + \%(O_2)\ 4.98 + \%(O)\ 2.88)$. The neutral density, N, now depends on v_{in} and each of the percentage compositions from MSIS. If we assume that these all are independent (which of course they won't be since the three percentages add up to 100!), from the theory of propagation of errors we get

$$\sigma_N^2 = \sigma_{v_{in}}^2\left(\frac{\partial N}{\partial v_{in}}\right)^2 + \sigma_{\%N_2}^2\left(\frac{\partial N}{\partial(\%N_2)}\right)^2 + \sigma_{\%O_2}^2\left(\frac{\partial N}{\partial(\%O_2)}\right)^2 + \sigma_{\%O}^2\left(\frac{\partial N}{\partial(\%O)}\right)^2$$

Now,

$$\frac{\partial N}{\partial v_{in}} = \frac{1}{AB}, \quad \frac{\partial N}{\partial(\%N_2)} = \frac{-v_{in} \cdot 5.07}{AB^2}, \quad \frac{\partial N}{\partial(\%O_2)} = \frac{-v_{in} \cdot 4.98}{AB^2}, \quad \frac{\partial N}{\partial(\%O)} = \frac{-v_{in} \cdot 2.88}{AB^2},$$

and so,

$$\sigma_N^2 = \frac{\sigma_{v_{in}}^2 B^2 + v_{in}^2 (0.15)^2 \left[\left(\%(N_2) \cdot 5.07 \right)^2 + \left(\%(O_2) \cdot 4.98 \right)^2 + \left(\%(O) \cdot 2.88 \right)^2 \right]}{A^2 B^4}$$

This is how I get my neutral density error estimates from the v_{in} estimates.

A similar process is used to get error estimates in the amplitudes and phases of the tides. When neutral density data is fit for the various modes of tidal oscillations, the program REGRESS [Bevington, 1969] returns a cosine and sine amplitude for each tidal mode. With each amplitude is an associated error estimate. But I transform the cosine and sine amplitudes into an amplitude and phase of a cosine curve. Symbolically

$$B\cos(\omega t) + C\sin(\omega t) = A\cos[\omega(t - \Phi)]$$

where B and C (and σ_B and σ_C) are returned by the regression program, and A and Φ (as well as σ_A and σ_Φ) are to be calculated. Written in this form Φ is the local time of maximum. These quantities can be calculated as follows:

$$A = \left(B^2 + C^2 \right)^{1/2} \qquad \Phi = (1/\omega)\tan^{-1}(C/B)$$

Using the principles of propagation of errors, the uncertainties in the new amplitude and phase are given by

$$\sigma_A^2 = \sigma_B^2 \frac{B^2}{\left(B^2 + C^2 \right)} + \sigma_C^2 \frac{C^2}{\left(B^2 + C^2 \right)} \quad \& \quad \sigma_\Phi^2 = \left(\frac{1}{\omega} \right)^2 \left[\sigma_B^2 \frac{C^2}{\left(B^2 + C^2 \right)^2} + \sigma_C^2 \frac{B^2}{\left(B^2 + C^2 \right)^2} \right]$$

93

References

Banks, P. M., "Collision frequencies and energy transfer," *Planet. Space Sci.,14*, 1105-1122, 1966.

Banks, P. M., "Observations of Joule and particle heating in the auroral zone," *J. Atmos. Terr. Phys., 39*, 179-193, 1977.

Banks, P. M., and G. Kockarts, *Aeronomy*, Academic, New York, 1973.

de la Beaujardière, O., V. B. Wickwar, C. A. Leger, M. A. McCready, and M. J. Baron, "The software system for the Chatanika incoherent-scatter radar," *SRI Projects 4964 and 4995 Tech. Rep., 2nd ed.*, SRI International, Menlo Park, CA, 127 pp., 1984.

Bendat, J. S. and A. G. Piersol, *Random Data Analysis and Measurement Procedures*, John Wiley & Sons, New York, 1986.

Bevington, P. R., *Data Reduction and Error Analysis for the Physical Sciences*, 336 pp., Mc Graw-Hill, New York, 1969.

Bjørnå, N. "Derivation of ion-neutral collision frequencies from a combined ion line/plasma line incoherent scatter experiment," *J. Geophys. Res.*, in press.

Bowles, K. L., "Observations of vertical incidence scatter from the ionosphere at 41 Mc/sec," *Phys. Rev. Lett., 1*, 454-455, 1958.

Bowles, K. L., "Incoherent scattering by free electrons as a technique for studying the ionosphere and exosphere: Some observations and theoretical considerations," *J. Research NBS, 65D*, 1-13, 1961.

Dougherty, J. P. and D. T. Farley, Jr., "A theory of incoherent scattering of radio waves by a plasma," *Proc. Roy . Soc. london, A, 259*, 79-99, 1960.

Dougherty, J. P. and D. T. Farley, Jr., "A theory of incoherent scattering of radio waves by a plasma 3. Scattering in a partly ionized gas," *J. Geophys. Res.*, *68*, 19, 5473-5486, 1963.

Evans, J. V., "Theory and practice of ionosphere study by Thomson scatter radar," *Proc. IEEE*, *57*, 4, 496-530, 1969.

Evans, J. V., "Some post-war developments in ground-based radiowave sounding of the ionosphere," *J. Atmos. Terr. Phys.*, *36*, 2183-2234, 1974.

Evans, J. V., "Incoherent scatter contributions to studies of the dynamics of the lower thermosphere," *Rev. Geophys. Space Phys.*, *16*, 2, 195-216, 1978.

Farley, D. T., J. P. Dougherty, and D. W. Barron, "A theory of incoherent scattering of radio waves by a plasma 2. Scattering in a magnetic field, *Proc. Roy . Soc. london, A, 263*, 238-258, 1961.

Fejer, J. A., "Scattering of radio waves by an ionized gas in thermal equilibrium in the presence of a uniform magnetic field," *Canad. J. Phys.*, *39*, 716-740, 1961.

Fesen, C. G., and R. G. Roble, "Simulations of the September 1987 lower thermospheric tides with the NCAR TIGCM," *J. Geophys. Res.*, in press.

Fesen, C. G., R. E. Dickinson, and R. G. Roble, "Simulation of the thermospheric tides at equinox with the National Center for Atmospheric Research thermospheric general circulation model," *J. Geophys. Res.*, *91*, A4, 4471-4489, 1986.

Flå, T., S. Kirkwood, and K. Schlegel, "Collision frequency measurements in the high-latitude E region with EISCAT," *Radio Sci.*, *20*, 4, 785-793, 1985.

Forbes, J., "Atmospheric tides 1. Model description and results for the solar diurnal component," *J. Geophys. Res.*, *87*, A7, 5222-5240, 1982a.

Forbes, J., "Atmospheric tides 2. The solar and lunar semidiurnal components," *J. Geophys. Res.*, *87*, A7, 5241-5252, 1982b.

95

Forbes, J., "Thermospheric Extensions of the Classical Expansion Functions for Semidiurnal Tides," *J. Geophys. Res.*, *87*, A7, 5253-5259, 1982c.

Forbes, J. M. and H. B. Garrett, "Theoretical Studies of Atmospheric Tides," *Rev. Geophys. Space Phys.*, *17*, 8, 1951-1981, 1979a.

Forbes, J. M., and F. A. Marcos, "Tidal variations in total mass density as derived from the AE-E Mesa Experiment," *J. Geophys. Res.*, *84*, 31-35, 1979b.

Gage K. S. and B. B. Balsley, "On the scattering and reflection mechanisms contributing to clear air radar echoes from the troposphere, stratosphere, and mesosphere," *Radio Sci.*, *15*, 2, 243-257, 1980.

Gordon, W. E., "Incoherent scattering of radio waves by free electrons with applications to space exploration by radar," *Proc. IRE*, *46*, 1824-1829, 1958.

Hagfors, T. and R. A. Brockelman, "A theory of collision dominated electron density fluctuations in a plasma with applications to incoherent scattering," *Phys. Fluids*, *14*, 6, 1143-1151, 1971.

Hedin, A., "MSIS-86 thermospheric model," *J. Geophys. Res.*, *92*, 4649-4662, 1987.

Huuskonen, A., "High resolution observations of the collision frequency and temperatures with the EISCAT UHF radar," *Planet. Space Sci.*,*37*, 211-221, 1989.

Huuskonen, A., T. Nygrèn, L. Jalonen, T. Turunen, and J. Silèn, "High resolution EISCAT observations of the ion-neutral collision frequency in the lower E-region," *J. Atmos. Terr. Phys.*, *48*, 827-836, 1986.

Johnson, R. M., "Radar observations of high-latitude lower-thermospheric and upper-mesospheric winds and their response to geomagnetic activity," *PhD Dissertation, UCLA*, 1-351, 1987.

Johnson, R. M., "Lower-thermospheric neutral winds at high latitude determined from incoherent scatter measurements: a review of techniques and observations," *Adv. Space Res*, *10*, 6, 6261-6275, 1990.

Johnson, R. M., "Sondrestrom incoherent scatter radar observations during the Lower-Thermospheric Coupling Study: 21-26 September 1987," *J. Geophys. Res.*, in press.

Johnson, R. M. and V. B. Wickwar, "Incoherent Scatter Measurements of High-Latitude Lower-Thermospheric Density and Dynamics," *AFGL Technical Report*, in press.

Kirkwood, S., "Seasonal and tidal variations of neutral temperatures and densities in the high latitude lower thermosphere measured by EISCAT," *J. Atmos. Terr. Phys., 48*, 817-826, 1986.

Killeen, T. L., "Energetics and dynamics of the Earth's thermosphere," *Rev Geophys., 25*, 3, 433-454, 1987.

Kofman, W., and C. Lathuillere, "EISCAT multipulse technique and its contribution to auroral ionosphere and thermosphere description," *J. Geophys. Res., 90*, A4, 3520-3524, 1985.

Kofman, W., C. Lathuillere, and B. Pibaret, "Neutral atmosphere studies in the altitude range 90-110 km by EISCAT," *J. Atmos. Terr. Phys., 48*, 837-848, 1986.

Lathuillere, C., V. B. Wickwar, and W. Kofman, "Incoherent scatter measurements of ion-neutral collision frequencies and temperatures in the lower thermosphere of the auroral region," *J. Geophys. Res., 88*, 10137-10144, 1983.

Manson, A. H. and C. E. Meek, "Middle Atmosphere (60-110 km) Tidal Oscillations at Saskatoon, Canada (52°N, 107°W) During 1983-1984," *Radio Sci., 20*, 1441-1451, 1985.

Manson, A. H., C. E. Meek, and J. B. Gregory, "Winds and Waves (10 min-30 days) in the Mesosphere and Lower Thermosphere at Saskatoon (52°N, 107°W, L=4.3) During the Year, October 1979 to July 1980," *J. Geophys. Res., 86*, C10, 9615-9625, 1981.

Mathews, J. D., "Measurements of the Diurnal Tides in the 80- to 100-km Altitude Range at Arecibo," *J. Geophys. Res., 81*, 25, 4671-4677, 1976.

Nygrén, T., L. Jalonen, and A. Huuskonen, "A new method of measuring the ion-neutral collision frequency using incoherent scatter radar," *Planet. Space Sci., 35*, 337-343, 1987.

97

Roble, R. G., E. C. Ridley, A. D. Richmond, and R. E. Dickinson, "A coupled thermosphere/ionosphere general circulation model," *Geophys. Res. Lett., 15,* 1325-1328, 1988.

Salah, J. E., "Daily oscillations of the mid-latitude thermosphere studied by incoherent scatter at Millstone Hill," *J. Atmos. Terr. Phys., 36,* 1891-1909, 1974.

Salah, J. E., J. V. Evans, and R. H. Wand, "Seasonal variations in the thermosphere above Millstone Hill," *Radio Sci., 9,* 231-238, 1974.

Salah, J. E., R. H. Wand, and J. V. Evans, "Tidal effects in the E region from incoherent scatter radar observations," *Radio Sci., 10,* 347-355, 1975.

Schlegel, K. and J. P. St.-Maurice, "Anomalous Heating of the Polar E Regions by Unstable Plasma Waves 1. Observations," *J. Geophys. Res., 86,* A3, 1447-1452, 1981.

Schlegel, K., H. Kohl, and K. Rinnert, "Temperature and collision frequency in the polar E region measured with the incoherent scatter technique," *J. Geophys. Res., 85,* A2, 710-714, 1980.

Sharp, L. R., D. R. Hickman, C. J. Rice, and J. M. Straus, "The altitude dependence of the local time variation of thermospheric density," *Geophys. Res. Lett., 5,* 261, 1978.

St.-Maurice J.-P. and W. B. Hanson, "Ion Frictional Heating at High Latitudes and Its Possible Use for an In Situ Determination of Neutral Thermospheric Winds and Temperatures," *J. Geophys. Res., 87,* A9, 7580-7602, 1982.

St.-Maurice, J. P., K. Schlegel, and P. M. Banks, "Anomalous heating of the polar E region by unstable plasma waves 2. Theory," *J. Geophys. Res., 86,* A3, 1453-1462, 1981.

Tepley, C. A. and J. D. Mathews, "Preliminary measurements of ion-neutral collision frequencies and mean temperatures in the Arecibo 80- to 100-km altitude region," *J. Geophys. Res., 83,* A7, 3299-3302, 1978.

Tepley, C. A., J. D. Mathews, and W. Ganguly, "Incoherent scatter radar studies of mesospheric temperatures and collision frequencies at Arecibo," *J. Geophys. Res., 86,* A13, 330-334, 1981.

Vickrey, J. F., "Incoherent Scatter Theory -- An Intuitive Approach," *Lecture notes presented at the Chatanika Radar School,* 1980.

Walker, J. C. G., "Space Science Without Rockets: Measurements of Ionospheric Properties at the Arecibo Observatory," *EOS, 59,* 4, 180-189, 1978.

Walker, J. C. G., "Radar Measurment of the Upper Atmosphere," *Science, 206,* 180-189, 1979.

Wand, R. H., "Semidiurnal tides in the E region from incoherent scatter measurements at Arecibo," *Radio Sci., 11,* 641-652, 1976.

Wand. R. H. and F. W. Perkins, "Radar Thomson scatter observations of temperature and ion-neutral collision frequency in the E-region," *J. Geophys. Res., 73,* 19, 6370-6372, 1968.

Wickwar, V. B., C. Lathuillere, W. Kofman, and G. Lejeune, "Elevated Electron Temperatures in the Auroral E Layer Measured With the Chatanika Radar," *J. Geophys. Res., 86,* A6, 4721-4730, 1981.